Mechanics of Deformation of Carbon Nanotube-Polymer Nanocomposites

by

Theodoros Akiskalos

Submitted to the Department of Mechanical Engineering
in partial fulfillment of the requirements for the degree of

Master of Science in Mechanical Engineering

at the

MASSACHUSETTS INSTITUTE OF TECHNOLOGY

June 2004

Author ....
Department of Mechanical Engineering
May 7, 2004

Certified by ....
Mary C. Boyce
Distinguished Alumnae Professor of Mechanical Engineering
Thesis Supervisor

Certified by ....
David M. Parks
Professor of Mechanical Engineering
Thesis Supervisor

Accepted by ....
Ain A. Sonin
Chairman, Department Committee on Graduate Students

Mechanics of Deformation of Carbon Nanotube-Polymer Nanocomposites

by

Theodoros Akiskalos

Submitted to the Department of Mechanical Engineering
on May 7, 2004, in partial fulfillment of the
requirements for the degree of
Master of Science in Mechanical Engineering

Abstract

The goal is to develop finite element techniques to evaluate the mechanical behavior of carbon nanotube enabled composites and gain a thorough understanding of the parameters that affect the properties of the composite, both micro- and macroscopically. Micromechanical models of representative volume elements (RVEs) of unit-cell and random multi-particle distributions are used to study such parameters and their performance and accuracy in doing is compared and discussed. The microstructural parameters of interest can be loosely categorized in two groups: those related to the geometry of the composite and those associated with the matrix-nanotube interactions as well as the load transfer mechanisms along the interface and inside the nanotubes. Among the geometry-related parameters, of particular interest are the nanotube aspect ratio, the number of walls, as well as the weight and volume fraction of nanotubes, their distribution and alignment in the matrix and their curvature. In terms of the matrix-nanotube interactions, emphasis is given on the bonds developed between the matrix and the nanotube and their effect on load transfer. The amount of load transferred internally in multi-wall nanotubes is also investigated. A number of models have been created and finite element methods have been employed to analyze the macroscopic mechanical behavior of nanotube-enabled composites, using the axial stiffness as the common metric in all cases. Fully functionalized matrix-nanotube interfaces have enabled the separate investigation of load transfer internally in multi-wall nanotubes. Unit-cell RVEs with appropriate periodic boundary conditions to emulate regular stacked or regular staggered arrays of nanotubes within a matrix, highlight the deficiency of using stacked array RVEs for assessing macroscopic properties. Unit-cell RVEs with staggered boundary conditions enable the detailed examination of issues, regarding modelling of the layered nature of nanotube walls. However, they do not fully capture the effects associated with the distribution of the nanotubes in the matrix. The focus shifted on accurately defining a RVE by analyzing nanotube dispersion in the matrix statistically, with emphasis on the proximity of neighboring particles. Simulated random distributions are studied in terms of the degree of filler clustering and its effect on composite stiffness and compared to nanotube distributions obtained from SEM images of actual composites. As a result, multi-particle finite element models are developed, based on these random distributions. They allow investigation of randomness in alignment, dispersion and curvature and are able to capture the characteristics and behavior of actual nanotube-enabled polymer composites more accurately than unit-cell models.

Thesis Supervisor: Mary C. Boyce
Title: Distinguished Alumnae Professor of Mechanical Engineering

Thesis Supervisor: David M. Parks
Title: Professor of Mechanical Engineering

Acknowledgments

First of all, I'd like to thank my advisors, Professor Mary. C. Boyce and Professor David M. Parks for their guidance and inspiration they provided during my years at MIT. I'm also grateful to my family for their loving support throughout my life so far. To all my friends and colleagues in the Mechanics and Materials research group, it was a great pleasure and privilege working alongside each one of you. Finally, to Ray, Una and Leslie, thank you for making this experience a little smoother.

Support for this work was provided by the Cambridge-MIT Institute.

Contents

List of Figures

List of Tables

Chapter 1

Introduction

The recent discovery of carbon nanotubes and the research activity associated with them can be thought of as a natural evolution of carbon-based fibers and an advance towards composites with fillers at the nanometer size scale, also known as nanocomposites. The use of fibers as stiffening and strengthening agents can be traced as far back as *800 BC*, when the Ancient Egyptians mixed straw and clay to produce reinforced bricks. This is one of the first documented instances in which a one-dimensional, high-aspect-ratio filler was used to produce a composite with higher stiffness and strength than the matrix material. Another example of early fiber-reinforced composites comes from Mongolia, where natives made their bows out of animal tendons, wood and silk around *1300 AD* (Beaumont, 1989). For centuries, these and numerous other naturally occurring fibers such as sisal, hemp, kenaf, flax, jute and coconut were widely used for the purpose of creating composites with enhanced mechanical properties. Some natural fibers are still being used in applications in which recyclability of the part is important.

It wasn't until the 19^{th} century that the need for materials with advanced properties stimulated the development of manufactured fibers. Initial efforts to create a fiber that would emulate the properties of silk, called "artificial silk", were not particularly successful. The first breakthrough in the development of advanced fibers came with the production of the first carbon fiber by Thomas Edison in *1892* (Edison, 1892), which was a product of carbonization of cotton and bamboo fibers and was used

Material	Density (Mg/m^3)	Tensile strength (GPa)	Tensile modulus (GPa)	Specific	
				Strength	Stiffness
Composites[a]					
E glass	2.1	1.1	45	0.5	20
Aramid	1.4	1.4	75	1.0	90
Type I carbon	1.5	1.1	220	0.7	130
Type II carbon	2.0	1.5	140	1.0	90
Metals					
Steel	7.8	1.3	200	0.2	26
Aluminium	2.8	0.3	73	0.1	26
Titanium	4.0	0.4	100	0.1	25

[a] Sixty percent fibre volume fraction unidirectional reinforcement.

Table 1.1: Comparison of mechanical properties of some popular composites and metals (Edwards, 1998)

as a filament for the new incandescent electric lamp. Despite Edison's pioneering work, interest in carbon fibers gradually faded as a more sturdy tungsten filament was developed for the light bulb (Saito et al., 1998).

Interest in carbon fibers and their composites was rekindled in the mid-1950's primarily due to the demand for lighter, stronger and stiffer materials for the aviation and space industries as well as due to solid-state theory's promising predictions of the potentially extremely high tensile strengths of defect-free crystals. The aerospace industry was initially attracted to titanium for its high strength-to-density ratio, but after spending significant resources on research and encountering insurmountable obstacles in its application, the industry turned to advanced carbon-fiber-reinforced composites, pursuing a deliberately more cautious but also more complete approach to their development (Jones, 1999). The interest in carbon-fiber composites proved to be well-founded, as suggested by Table 1.1 and Figure 1-1, in which modern popular composites are compared with some typical metals in terms of their mechanical properties and density.

The first filamentary carbon fibers were produced by the controlled pyrolysis of a precursor, such as rayon, which was later replaced by polyacrylonitrile (PAN) and pitch except for carbon-carbon composites, for which rayon is still used. In fact, this process is still being used nowadays to some extent. However, the need to reduce fiber defects, develop ultra-high modulus carbon fibers and have even greater control over processing sparked an interest in other production methods, such as catalytic

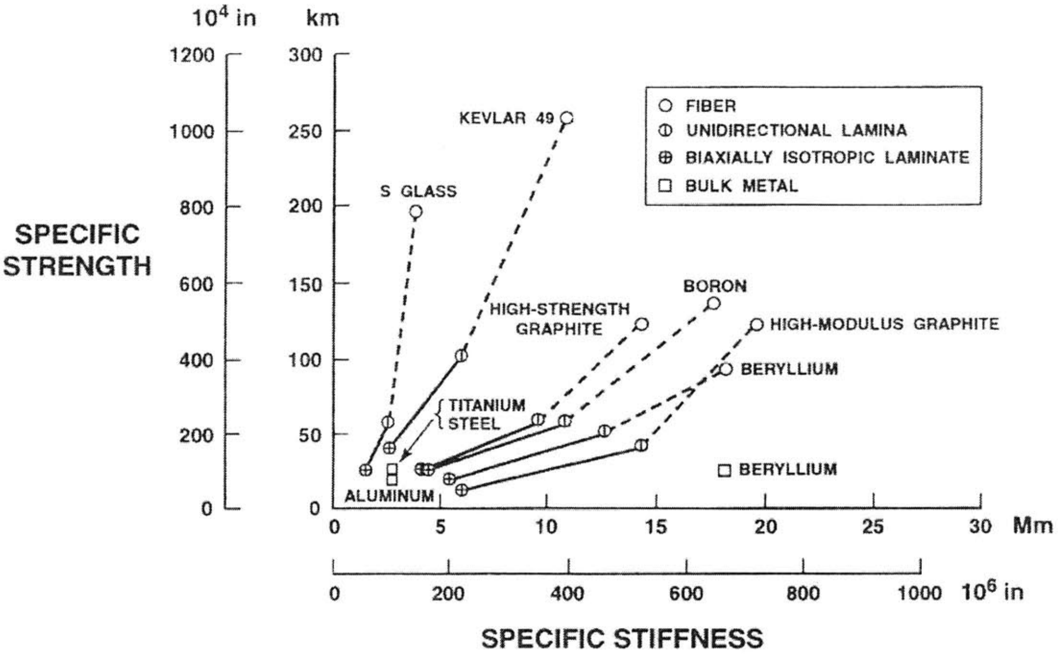

Figure 1-1: Specific strength and stiffness of some popular composites and metals (Jones, 1999)

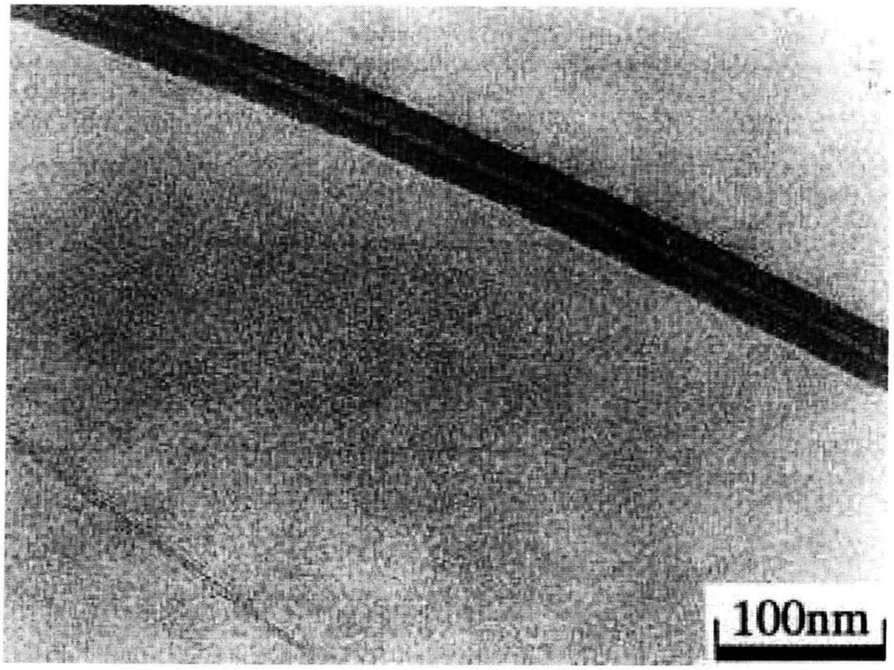

Figure 1-2: TEM micrograph showing a nanotube alongside a vapor grown carbon fiber (Dresselhaus et al., 2001a)

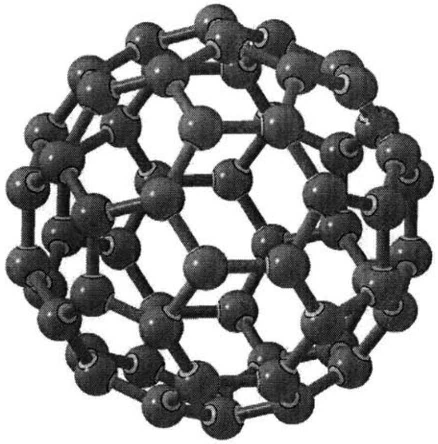

Figure 1-3: The first fullerene structure, C_{60}, also known as buckminsterfullerene (http://www.chem.sunysb.edu/msl/, 2004)

chemical vapor deposition processes (Saito et al., 1998). It was at that point that the growth of very thin filaments as byproducts, with diameters on the order of a few nanometers, was first observed. Figure 1-2 shows an instance of such a filament alongside a vapor grown carbon fiber (Dresselhaus et al., 2001a). However, these filaments were not studied systematically until the discovery of fullerenes in 1985 by Kroto and Smalley (Kroto et al., 1985), which sparked speculation about the existence of nano-sized carbon tubes, capped at both ends by fullerene hemispheres (Saito et al., 1998) (Figure 1-3). The experimental observation of carbon nanotubes, *CNT* in short, by Iijima in *1991* (Iijima, 1991) bridged the gap with the theoretical background set by the discovery of fullerenes and fuelled the rapidly growing study of carbon nanotubes ever since.

This thesis covers our research into the mechanics of deformation of carbon nanotube enabled materials. The overall objective has been to evaluate the mechanical behavior of CNT/polymer composites through modelling and experimentation. More specifically, the goal has been to gain a thorough understanding of the parameters that affect the properties of the composite, both at the microscopic and the macroscopic level. As it will be discussed later in more detail, these parameters could be loosely categorized in two groups: those related to the geometry of the composite and those associated with the matrix-nanotube interactions as well as the load transfer mechanisms along the interface and inside the nanotubes.

1.1 Carbon fibers and carbon fiber-reinforced composites

Before delving into the issues associated with carbon nanotubes and their composites, it is essential to provide an overview of their macroscopic analog, carbon fibers.

1.1.1 Processing, microstructure and properties of carbon fibers

Polymer-based carbon fibers

Carbon fibers can be produced by two processes. The most popular one, pyrolysis of a precursor, is comprised of three stages, namely oxidation (heating in oxidizing atmosphere at 200–250C), carbonization (heating in non-oxidizing atmosphere at 1000C) and graphitization (heating in non-oxidizing atmosphere at 2500–3000C). A variety of precursors can be used, with PAN, pitch and rayon being the three most important ones, in order of volume used.

The resulting fibers are typically a few microns in diameter (around $7\mu m$) and consist of "undulating, ribbon-like crystallites", intertwined and oriented more or less parallel to the axis of the fiber (Walsh, 2001) (Figure 1-4). The length and the degree of orientation of these crystallites determine the longitudinal stiffness of the fiber, with highly oriented pyrolytic graphite (HOPG) serving as a benchmark for the characterization of carbon fibers. Each crystallite consists of multiple graphene layers which are strong and stiff in the axial direction, due to the strong covalent C-C bonds within each plane, considered to be among the strongest bonds in nature. However, they provide only limited shear resistance, because of the weak van der Waals bonds between each layer. In the transverse direction, the graphene layers

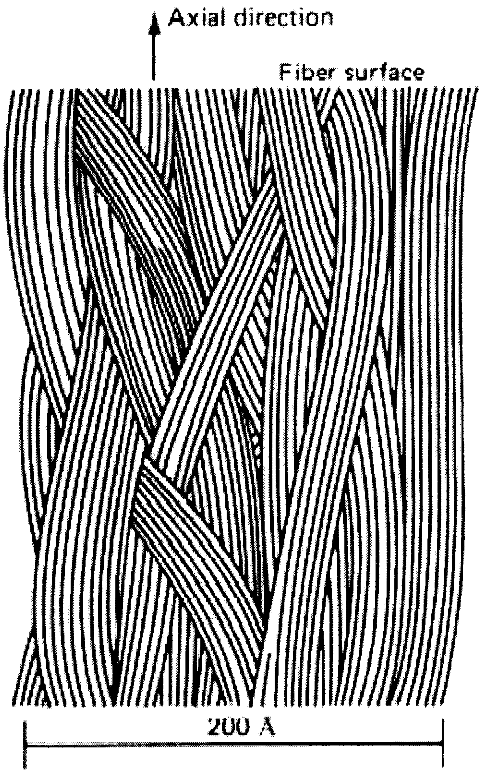

Figure 1-4: Schematic of typical axial microstructures of polymer-based carbon fibers (Walsh, 2001)

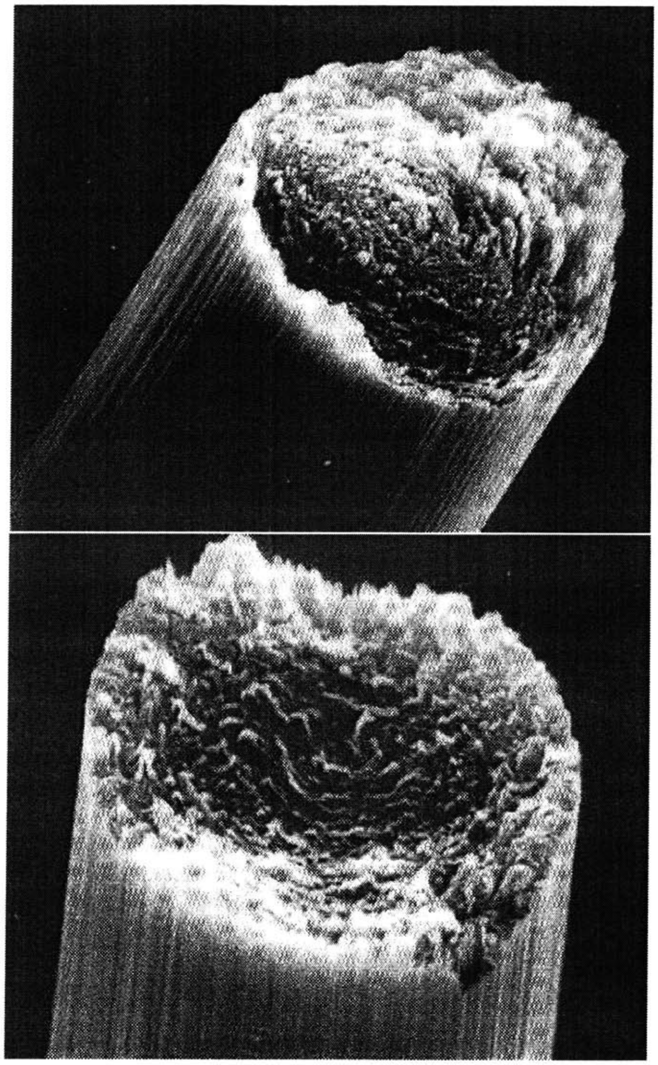

Figure 1-5: Typical transverse microstructures of polymer-based carbon fibers (Dresselhaus et al., 1988)

Fibre type	Density (Mg m^{-3})	Tensile strength (GPa)	Modulus of elasticity (GPa)		Strain to failure (%)	Coeff. of thermal exp. (10^{-6} K^{-1})	
			Long.	Trans.		Long.	Trans.
Glass							
E	2.6	2.4	73	73	3.8	5	5
R	2.53	3.5	86	86	4.1	4	4
Aramid							
HM	1.45	3.0	130	5.4	2.1	−2	17
LM	1.44	2.8	65		4.3		
Carbon							
HM1	1.96	1.75	500	5.7	0.35	−1.5	30
HM2	1.8	3.0	300		1.0	−0.2	
HT	1.78	3.6	240	15	1.5	−0.5	10
HST	1.75	5.0	240		2.1	−0.1	
IM	1.77	4.7	295		1.6		

Abbreviations: HM, high modulus; LM, low modulus; HM1,2, high modulus; HT, high tensile strength; HST, high strain; IM, intermediate type.

Table 1.2: Typical properties of some popular reinforcing fibers (Edwards, 1998)

are often arranged in structures similar to an "onion skin", resembling onion layers close to the fiber surface and being randomly oriented at the core region, as shown in Figure 1-5.

By altering a few key processing parameters, such as fiber tension and heat treatment and precursor spinning, it is possible to affect the fiber microstructure, in terms of the crystallite size and alignment as well as number and size of defects and produce carbon fibers with different strength and toughness, usually trading one for the other. As a result, there are three main types of polymer-based carbon fibers, although these categories are somewhat blurred: high modulus, high strength and general purpose. All carbon fibers behave elastically in tension up to failure, which occurs at very low strain (Edwards, 1998). Table 1.2 summarizes some of the typical properties for these fibers.

Comparison with the properties of the bulk material suggests that fibers are both stronger and stiffer. This increase in stiffness and strength can be attributed to the microstructure and size of the fibers. Due to the fibers' small-sized diameter, which can range from a few nanometers for nanofibers to hundreds of microns for polymer-based carbon fibers, they not only contain far fewer defects than the bulk material, but they also consist of well-aligned crystals with strong chemical bonds oriented axially, thus resulting in increased strength and stiffness in the direction of the fiber.

It is for this reason that the mechanical properties of fibers are often cited as the limiting case or as theoretical values for the properties of the bulk material.

Vapor-grown carbon fibers

Another, more recently developed production method of carbon fibers is the chemical vapor deposition of carbon from pyrolysis of a hydrocarbon (e.g., acetylene, benzene, natural gas) typically at 1100C, in the presence of a metal catalyst (e.g., Fe, Ni, Co) (Jacobsen et al., 1995). Subsequent heat treatment to 3000C results in near complete graphitization (Dresselhaus et al., 1988). This method was developed as a result of the need to reduce fiber defects, synthesize more crystalline fibers and gain greater control over processing. Indeed, the fibers produced by this method, also called vapor-grown carbon fibers (VGCF), are thinner, with properties approaching those of single crystal graphite and their aspect ratio can be controlled with reasonable accuracy (Ting et al., 1994).

In terms of their structure, VGCF are quite different from polymer-based carbon fibers. Instead of intertwined, oriented crystallites, VGCF feature numerous nested, concentric cylindrical shells arranged in a "tree-ring" microstructure, with limited layer-to-layer interactions and a hollow core about the size of the catalyst particle. An interesting observation, as indicated by Figure 1-6, is the presence of a carbon nanotube at the core of each VGCF, which suggests a structural and property-related discontinuity between the core and the surface of the VGCF. Furthermore, they are not continuous, although their lengths can be on the order of hundreds of millimeters.

The tensile elastic modulus of VGCF can vary from 250GPa (as grown) to more than 1TPa for heat treated fibers (Jacobsen et al., 1995) and tensile strength assumes values between 2.5 and 3GPa. In general, VGCF demonstrate mechanical properties superior to polymer-based carbon fibers, due to their greater microstructural organization (Dresselhaus et al., 1988).

As suggested earlier, research on VGCF stimulated the interest in carbon filaments of very small diameters, which led to the discovery of carbon nanotubes. The goal has been to create the ultimate carbon fiber, one that will be as structurally perfect as

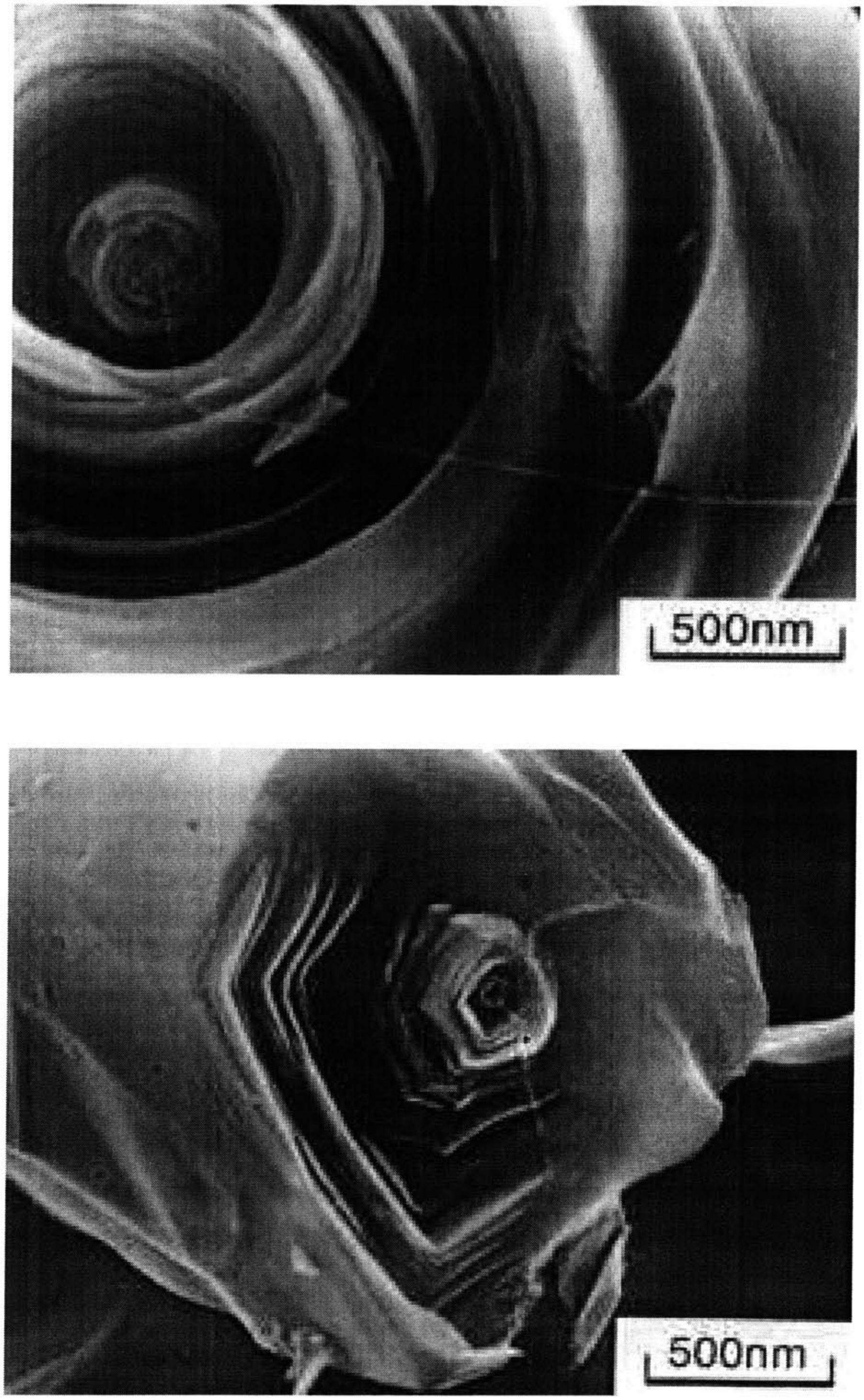

Figure 1-6: Exposed carbon nanotube at the core of a fractured VGCF (Dresselhaus et al., 2001a)

single-crystal graphite. The first step in that direction was taken with the production of VGCF. As it will be shown, the discovery of carbon nanotubes constitutes yet another major leap towards achieving this goal.

1.1.2 Carbon fiber composites

In order to capitalize on the exceptional mechanical properties of carbon fibers, they must be placed inside a matrix as reinforcement, creating a fiber-reinforced composite. The most commonly used matrix materials are polymeric, consisting mostly of thermosetting resins and, more recently, of thermoplastics (Schaffer et al., 1995). Typical thermosets include polyimides and various epoxies, whereas typical thermoplastics, which have the added advantage of not requiring a curing stage, include polyetheretherketone, polypropylene and nylon 6 (Dresselhaus et al., 1988).

Such matrices are typically of lower strength, stiffness and density but higher toughness than the fibers. Reinforcing these matrices with carbon fibers enhances the mechanical properties of the resulting composite, while maintaining the matrices' low density and toughness, thus demonstrating very favorable strength-to-density and stiffness-to-density ratios.

The functional role of the matrix is manifold. First, it allows load to be transferred to the fibers, so that all fibers are effective in bearing the load, while maintaining the structural integrity of the composite. Second, it protects the fibers from the environment. Third, it serves as a source of toughness for the composite, since carbon fibers are relatively brittle (Schaffer et al., 1995).

1.1.3 Mechanical behavior of carbon fiber composites

The simplest kind of carbon fiber composite is one in which all fibers are oriented in the same direction, also called unidirectional continuous carbon fiber-reinforced composite. The presence of carbon fibers in the matrix renders such composites highly anisotropic. As a result, strengthening pertains only to cases in which loading direction matches fiber orientation. Transverse behavior, perpendicular to the fiber direction, is close to that of the matrix (Edwards, 1998).

As mentioned earlier, carbon fibers typically behave elastically in tension in the axial direction up to their breaking point. The corresponding organic matrices are elastic up to strains that are much higher than the failure strains of the fibers. As a result, unidirectional fiber reinforced composites loaded in the axial direction behave elastically up to the point of fracture. Furthermore, if the fibers are perfectly bonded to the matrix, i.e. there is no fiber pull-out, the strain on both the reinforcing fibers and the matrix will be the same (isostrain condition).

The axial stiffness of carbon fibers can be orders of magnitude larger than that of the matrix. The difference is even more substantial in the case of carbon nanotubes. As a result, by the rule of mixtures, the axial stiffness of a unidirectional, fiber reinforced composite is dominated by the filler, assuming reasonable and practical volume fractions. The same is true for the strength of the composite. Since carbon fibers fail at much lower strains than matrices when loaded axially, the axial tensile strength of the composite is only limited by the strength of the fibers and their volume fraction (Schaffer et al., 1995).

Failure in carbon fiber composites under uniaxial tension can occur in various ways, including fiber-matrix debonding, fiber fracture, matrix microcracking and fiber pull-out. Some of the parameters that determine the failure mechanism are fiber aspect ratio, fiber strength and stiffness, matrix ductility and toughness, matrix-fiber bond interactions, the difference between the coefficient of thermal expansion of the matrix and that of the fiber, etc. (Beaumont, 1989).

In applications in which multi-axial loading is required, unidirectional carbon-fiber composites are obviously not an option. Laminate composites can be used instead, which consist of stacked layers of fibers oriented in the multiple directions. Directions are chosen to provide the necessary normal and shear stiffness and strength in the plane.

The preceding discussion of composites and their mechanical behavior pertains to continuous carbon fiber composites. Most of it is also directly applicable to the case of discontinuous fiber reinforcements, such as carbon nanotubes. Overall, carbon fiber reinforced composites, whether continuous or not, present numerous advantages over more traditional materials with respect to their mechanical behavior, which is the focus of this thesis. First, they have high specific strength and stiffness. Second, the structures made of such composites are both cheaper to produce and operate. Third, they can be tailored to specific applications, resulting in more effective material utilization. Finally, they demonstrate higher toughness and better fatigue resistance.

The macroscopic behavior of fiber reinforced composites depends on several parameters, which can be loosely categorized into those related to the geometry and structure of the reinforcing and the matrix phases and those related to their properties and interfacial interactions. All of them are of great interest in the study of carbon nanotube-enabled polymers and will be discussed in greater detail in the following chapters. Among the geometry-related factors, the most important ones are the volume fraction of the fibers, their dispersion and orientation in the matrix, their aspect ratio and, in the case of nanotubes, their type, i.e. single-wall or multi-wall.

The interfacial bonding between the fibers and the matrix is also a particularly important parameter, as it affects the stiffness, the strength and the fracture behavior of the composite. These interactions between the matrix and the stiff filler need to be of adequate stiffness in order to transfer load effectively from the former to the latter. Thermal stresses induced by different coefficients of thermal expansion between the matrix and the fiber can enhance interfacial bonding, as the matrix shrinks and tightens around the nanotube. Oxygen diffusion or moisture uptake through the interface, which is a preferential path for this purpose, may degrade composite behavior by weakening interfacial bonds.

There are two ways in which a fiber can bond with the matrix: mechanical and chemical bonding. Mechanical bonding occurs in the form of compression and friction along the interface. Such interaction can be induced by the aforementioned thermal coefficient mismatch, as matrix materials have a higher coefficient of thermal expansion and can exert compressive forces on the fibers when cooled from elevated processing temperatures. Mechanical bonding can be enhanced by increasing surface roughness of the fiber. Chemical bonding appears as "wetting" of the fiber surface, which results from short-range electron interactions between the fiber and the matrix. This type of bond is typically formed during processing and is sensitive both to the proximity and the cleanliness of the two surfaces (Schaffer et al., 1995). Carbon fibers have inert, non-polar surfaces and as a result cannot form chemical bonds easily. They are often treated with oxidizing agents and active chemical groups, such as hydroxyls, carboxyls and carbonyls, which increase surface roughness, thus facilitating mechanical bonding and form numerous "bridges" between the fiber and the matrix, which serve as weak chemical bonds and provide a strong interface due to their numbers, rather than the strength of each bond (Walsh, 2001).

1.1.4 Modelling of fiber-reinforced composites

Although in the previous discussion no distinction was made between continuous and short or discontinuous fiber composites, it is necessary to do so at this point for the purpose of showcasing various micromechanical models. A fundamental difference between the two is that the isostrain condition is only applicable to modelling of uniaxial continuous fiber composites, loaded in tension and assuming there is no fiber pullout. However, this is not true for short fiber composites. Since carbon nanotubes are not continuous, the focus of this section will be on micromechanical modelling of short fiber composites.

Calculation of average stress, strain and properties

Before presenting in detail some of the models, it is useful to briefly discuss some preliminary concepts, following Tucker's review of these ideas (Tucker et al., 1999).

The constitutive relations for the fiber and matrix materials are

$$\boldsymbol{\sigma}^f = \mathbf{C}^f \boldsymbol{\epsilon}^f \tag{1.1}$$

$$\boldsymbol{\sigma}^m = \mathbf{C}^m \boldsymbol{\epsilon}^m \tag{1.2}$$

The volume-average stress of the *composite*, $\bar{\sigma}$, is defined as

$$\bar{\boldsymbol{\sigma}} \equiv \frac{1}{V}\int_V \boldsymbol{\sigma}(\boldsymbol{x})dV \tag{1.3}$$

where $\sigma(x)$ is the local stress tensor. The average strain $\bar{\epsilon}$ is defined accordingly and

$$\bar{\boldsymbol{\sigma}} = \mathbf{C}\bar{\boldsymbol{\epsilon}} \tag{1.4}$$

where $\mathbf{C}$ is the average stiffness of the composite, on which modelling efforts have focused.

The volume over which the averaging occurs is assumed to be large enough to contain many fibers, yet small enough to justify a uniform average stress and strain assumption.

Similarly, the volume-average stresses of the *fiber* and the *matrix* over their corresponding volumes are defined as

$$\bar{\boldsymbol{\sigma}}^f \equiv \frac{1}{V_f}\int_{V_f} \boldsymbol{\sigma}(\boldsymbol{x})dV \tag{1.5}$$

$$\bar{\boldsymbol{\sigma}}^m \equiv \frac{1}{V_m}\int_{V_m} \boldsymbol{\sigma}(\boldsymbol{x})dV \tag{1.6}$$

and the average strains are defined accordingly. The average stresses and strains of the fiber and the matrix and those of the composite are related by

$$\bar{\boldsymbol{\sigma}} = v_f\bar{\boldsymbol{\sigma}}^f + v_m\bar{\boldsymbol{\epsilon}}^m \tag{1.7}$$

$$\bar{\boldsymbol{\epsilon}} = v_f\bar{\boldsymbol{\epsilon}}^f + v_m\bar{\boldsymbol{\epsilon}}^m \tag{1.8}$$

where v_f and v_m are the volume fractions of the fiber and the matrix accordingly and $v_f + v_m = 1$. The average strain in the composite is mapped to the average fiber strain by a strain concentration tensor $\mathbf{A}$ through

$$\bar{\boldsymbol{\epsilon}}^f = \mathbf{A}\bar{\boldsymbol{\epsilon}} \tag{1.9}$$

An alternate strain concentration tensor $\hat{\mathbf{A}}$ can be defined as

$$\bar{\boldsymbol{\epsilon}}^f = \hat{\mathbf{A}}\bar{\boldsymbol{\epsilon}}^m \tag{1.10}$$

The two tensors are related by

$$\mathbf{A} = \hat{\mathbf{A}}[(1 - v_f)\mathbf{I} + v_f\hat{\mathbf{A}}]^{-1} \tag{1.11}$$

An important consequence of these equations is the average strain theorem, according to which, if the representative volume is subjected to surface displacements that result in a uniform strain $\boldsymbol{\epsilon}^0$, then the average strain within the volume is equal to the uniform strain, $\bar{\boldsymbol{\epsilon}} = \boldsymbol{\epsilon}^0$. The same is true for average stresses, assuming that surface tractions resulting in uniform stresses in the body are applied.

Finally, combining Equations 1.2, 1.8, 1.4 and 1.9 results in

$$\mathbf{C} = \mathbf{C}^m + v_f(\mathbf{C}^f - \mathbf{C}^m)\mathbf{A} \tag{1.12}$$

It is suggested then by Equation 1.12 that if A is known, then the composite stiffness for a well-defined composite can be found.

Shear lag models

Among all models that predict the stiffness of discontinuous fiber composites, some of the most popular are the shear lag models, which also happen to be the first to be developed specifically for this reason. Unlike other models, it produces a prediction of the elastic properties only in the fiber direction; however, it is often assumed that all other engineering constants are almost independent of the fiber aspect ratio and can be obtained by a simple continuous fiber analysis.

There are a number of assumptions made in the original formulation by Cox in 1951 (Cox, 1952). First, a perfect bond is assumed between the matrix and the fibers. Furthermore, the elastic fibers are assumed to be loaded in simple tension, behaving as one-dimensional springs and the elastic matrix is assumed to deform in simple shear,

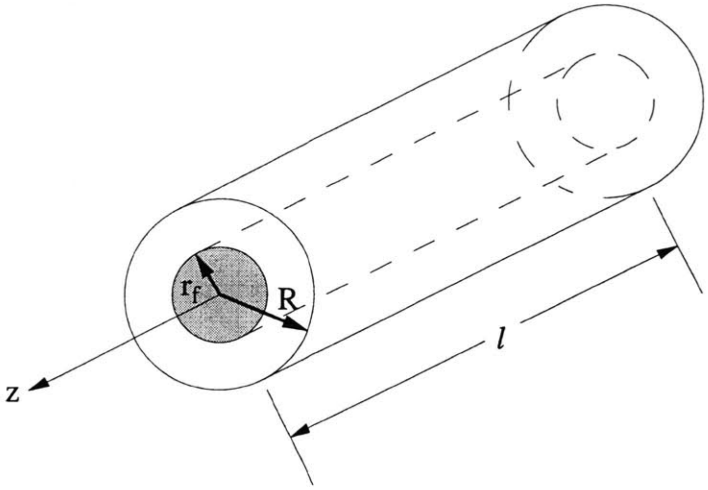

Figure 1-7: Geometry of unit cell for shear lag analysis (Tucker et al., 1999)

which is governed by the axial deformation of the uniformly distributed and aligned fibers. No tensile stress in transmitted at the fiber ends, which is a logical consequence of the non-applicability of the isostrain condition. Finally, the interfacial axial shear strain is assumed to be proportional to the difference in displacement between the fiber surface and the outer matrix surface.

The model suggests that a uniaxial tensile load that is applied to the composite in the fiber direction is transferred to the fibers by a shearing mechanism at the fiber-matrix interface. Longitudinal strain is lower in the matrix than in the fibers due to the lower stiffness of the former, which results in a shear stress distribution along the interface. The analysis assumes a unit cell with a fiber of length l and radius r_f embedded in a concentric shell of matrix with radius R as shown in Figure 1-7.

Focusing on the axial stress and strain σ_{zz} and ϵ_{zz} accordingly and neglecting Poisson effects, one can solve $\sigma^f_{zz} = E^f_{zz}\epsilon^f_{zz}$ for the distribution of the average axial stress over the fiber cross-section at a distance z from one of the fiber ends. Force equilibrium for an infinitesimal length dz of the fiber requires that

$$\frac{d\sigma^f_{zz}}{dz} = -\frac{2\tau_{rz}}{r_f} \tag{1.13}$$

where τ_{rz} is the shear stress along the fiber-matrix interface, as shown in Figure 1-

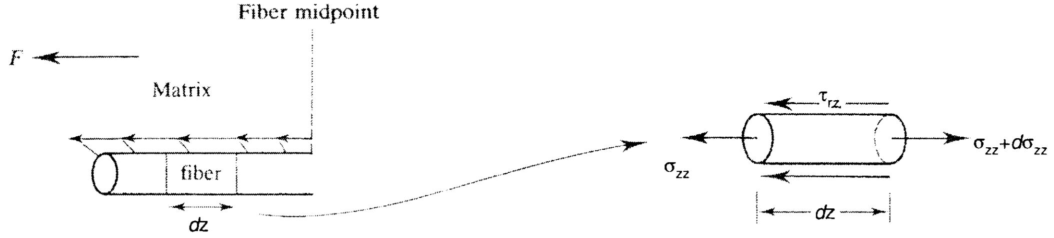

Figure 1-8: Longitudinal tensile loading of a unidirectional fiber composite (Courtney, 1990)

8.

Figure 1-9 shows the stress distributions along the interface under the specific assumptions.

A central assumption to the shear lag theory is the proportionality between τ_{rz} and the difference between the displacement u_z^f of the fiber at a distance z from one of the fiber ends and the displacement u_z^m of the matrix at the same point, if the fiber were absent.

$$\tau_{rz}(z) = \frac{H}{2\pi r_f}(u_z^m - u_z^f) \tag{1.14}$$

where H is a constant that depends on matrix material properties and fiber volume fraction. Then, from Equations 1.13 and 1.14, and since $\sigma_{zz}^f = E_{11}^f \frac{du_z^f}{dz}$ and the average composite axial strain is $\bar{\epsilon}_{zz} = \frac{dv_z^m}{dz}$, the governing differential equation becomes:

$$\frac{d^2\sigma_{zz}^f}{dz^2} = \frac{H}{\pi r_f^2}(\frac{\sigma_{zz}^f}{E_{11}^f} - \bar{\epsilon}_{zz}) \tag{1.15}$$

Solving Equation 1.15 and taking into account the boundary conditions of zero normal stress at the fiber ends, gives the fiber stress as a function of z:

$$\sigma_{zz}^f = E_{11}^f \bar{\epsilon}_z(1 - \frac{\cosh[\beta(l/2 - z)]}{\cosh[\beta(l/2)]}) \tag{1.16}$$

where $\beta = \sqrt{\frac{H}{\pi r_2^2 E_{11}^f}}$. The shear stress distribution along the interface can now be

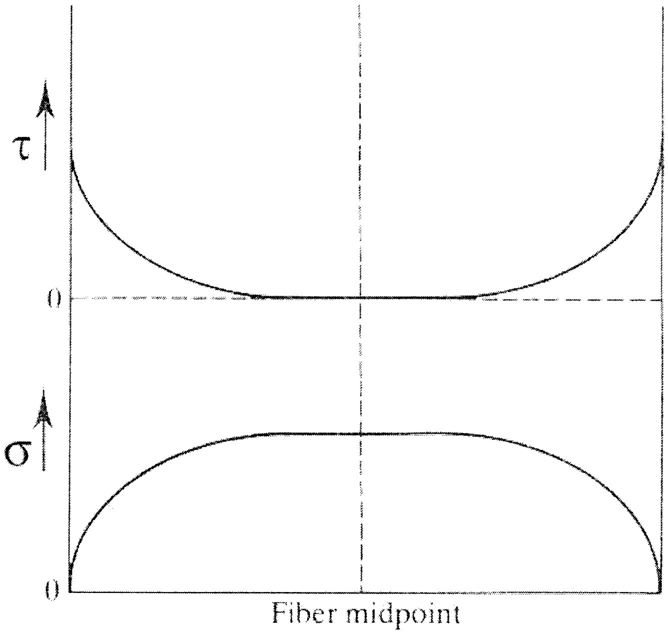

Figure 1-9: The variation of σ^f_{zz} and τ_{rz} with position along the interface assuming linear elastic matrix and fiber materials (Courtney, 1990)

derived from Equation 1.13 and 1.16

$$\tau_{rz} = -\frac{1}{2}E^f_{11}\bar{\epsilon}_{zz}\beta r_f \frac{\sinh[\beta(l/2 - z)]}{\cosh[\beta(l/2)]} \tag{1.17}$$

The average fiber stress can then be found by integrating Equation 1.16 over the length of the fiber

$$\bar{\sigma}^f_{zz} = \frac{1}{l}\int_0^l \sigma^f_{zz}(z)dz = E^f_{11}\bar{\epsilon}_{zz}(1 - \frac{\tanh[\beta(l/2)]}{\beta(l/2)}) \tag{1.18}$$

which can be rewritten in terms of the average fiber strain $\bar{\epsilon}^f_{zz} = \eta_l\bar{\epsilon}_{zz}$, where η_l is an efficiency factor, also known as the *effective modulus* of the fiber,

$$\eta_l = (1 - \frac{\tanh[\beta(l/2)]}{\beta(l/2)}) \tag{1.19}$$

η_l is the scalar analog of the strain concentration 4^{th} order tensor **A** introduced by

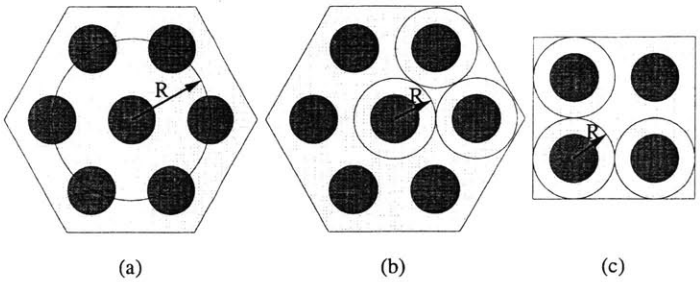

Figure 1-10: Fiber packing arrangements used to find R in shear lag models. (a) Cox. (b) Hexagonal. (c) Square (Tucker et al., 1999)

Hill (Hill, 1963), which is the ratio of the average fiber strain to the average strain in the composite.

For large $\beta(l/2)$, the value of η_l approaches 1, suggesting that the fiber and the matrix are subjected to the same uniform strain. In the opposite case, as $\beta(l/2)$ tends to 0, the fiber doesn't strain at all. Therefore, it is essential to determine the magnitude of β.

For this reason, Cox (Cox, 1952) assumed a similar cylindrical unit cell as before, the difference being in this case that the outer surface of the matrix is held fixed and the fiber is subjected to a uniform axial displacement, i.e. it is assumed rigid. An elasticity solution for the matrix layer then yields

$$H = \frac{2\pi G^m}{\ln(R/r_f)} \tag{1.20}$$

where G^m is the shear modulus of the matrix. H is a function of R and therefore it also depends on the periodic distribution of fibers in the matrix, which affects R. For this reason, a number of fiber array geometries have been proposed, such as hexagonal and square arrays. Figure 1-10 illustrates three different packing configurations along with the associated R. What is also important to note is that both a high fiber aspect ratio and a high G^m/E^f_{11} ratio are desirable for strengthening using discontinuous fibers.

Finally, in order to predict the axial modulus of the composite, E_{zz}, a simple rule of mixtures is derived, using average stresses for both the fiber and the matrix:

$$\sigma_{zz}^{c} = v_m \bar{\sigma}_{zz}^{m} + v_f \bar{\sigma_{zz}}^{f} \tag{1.21}$$

where the superscript *'c'* refers to values for the composite. Since $\sigma_{zz}^{c} = E_{zz}\bar{\epsilon}_{zz}$, substitution of $\bar{\sigma}_{zz}^{f}$ from Equation 1.18 into 1.21 gives

$$E_{zz} = \eta_l v_f E_{11}^{f} + (1 - v_f)E^{m} \tag{1.22}$$

The above discussion centers around the original formulation of the shear lag model. A number of other formulations have since been developed, each varying certain parameters or assumptions of the original.

Historically, the shear lag model has been widely adopted due to its physical basis as well as its algebraic simplicity. Indeed, the SLM utilizes simplified fiber and matrix representations to predict some key aspects of composite deformation, while at the same time, it is computationally more efficient than detailed 3-D finite element models (Xia et al., 2002b), which use an order of magnitude more degrees of freedom. Beyerlein suggests (Beyerlein et al., 1996) that the stresses determined by the shear lag model are accurate representations of local true stresses to a length scale of about one fiber diameter.

On the other hand, there are a number of drawbacks associated with its use. First, it is a one-dimensional analysis and as such, it only predicts the longitudinal elastic modulus of the composite unlike other models, such as the Mori-Tanaka and Halpin-Tsai. Additionally, the assumption that the fiber is a slender body subjected to uniform stress limits the range of applicability of the SLM to high-aspect-ratio fibers ($l/d \geq 10$), as it under predicts stresses for very short fibers (Tucker et al., 1999).

Eshelby model

Another important theory that addresses dilute short fiber composites is Eshelby's model (Eshelby, 1957). The term *dilute* in this case refers to the separation among the localized strain fields due to each fiber. In other words, in dilute short fiber composites, there is enough interparticle distance for the local strain field around each fiber to reach far-field strain according to St.Venant's principle before reaching the strain field of a neighboring fiber.

Central to Eshelby's model is the idea of *equivalent inclusion.* Eshelby started by assuming an initially stress-free infinite homogeneous solid body consisting of a matrix and an inclusion that undergoes a transformation such that, if it were a separate body, it would be subjected to a uniform strain $\boldsymbol{\epsilon}^T$. Since the inclusion is perfectly bonded to the matrix, the whole body develops a strain field $\boldsymbol{\epsilon}^C(\mathbf{x})$. The stresses in the matrix and the inclusion are accordingly

$$\boldsymbol{\sigma}^m(\mathbf{x}) = \mathbf{C}^m \boldsymbol{\epsilon}^C(\mathbf{x}) \tag{1.23}$$

$$\boldsymbol{\sigma}^I = \mathbf{C}^m(\boldsymbol{\epsilon}^C - \boldsymbol{\epsilon}^T) \tag{1.24}$$

where $\mathbf{C}^m$ is the stiffness of the body. Eshelby then showed that the strain $\boldsymbol{\epsilon}^C$ is uniform within an ellipsoidal inclusion and is related to $\boldsymbol{\epsilon}^T$ by

$$\boldsymbol{\epsilon}^C = \mathbf{E}\boldsymbol{\epsilon}^T \tag{1.25}$$

where $\mathbf{E}$ is called Eshelby's tensor and depends on the inclusion's aspect ratio and the matrix elastic constants.

The next step is to apply the same idea to an inhomogeneous inclusion, i.e. one with different properties from the surrounding matrix. Using similar procedures, the following result can be derived

$$-[\mathbf{C}^m + (\mathbf{C}^f - \mathbf{C}^m)\mathbf{E}]\boldsymbol{\epsilon}^T = (\mathbf{C}^f - \mathbf{C}^m)\boldsymbol{\epsilon}^A \tag{1.26}$$

where $\boldsymbol{\epsilon}^A$ is the uniform strain applied on the body.

This result can now be used to find the stiffness of a composite with ellipsoidal fibers. According to the average strain theorem, the average composite strain is equal to the applied strain. Furthermore, according to Eshelby, the fiber strain is given by $\bar{\boldsymbol{\epsilon}} = \boldsymbol{\epsilon}^A + \boldsymbol{\epsilon}^C$. Then, by combining Equations 1.25 and the previous results, one can relate the average composite strain, $\bar{\boldsymbol{\epsilon}}$, to the average fiber strain, $\bar{\boldsymbol{\epsilon}}^f$:

$$[\mathbf{I} + \mathbf{E}\mathbf{S}^m(\mathbf{C}^f - \mathbf{C}^m)]\bar{\boldsymbol{\epsilon}}^f = \bar{\boldsymbol{\epsilon}} \tag{1.27}$$

which defines the strain concentration tensor for Eshelby's equivalent inclusion as

$$\mathbf{A}^{Eshelby} = [\mathbf{I} + \mathbf{E}\mathbf{S}^m(\mathbf{C}^f - \mathbf{C}^m)]^{-1} \tag{1.28}$$

This result can then be used with Equation 1.12 to determine the composite stiffness.

The preceding discussion assumed ellipsoidal inclusions, although fibers in short fiber composites are better approximated as right cylinders. Steif and Hoysan (Steif et al., 1987) verified that although the ellipsoidal assumption is accurate at very low aspect ratio's, it consistently overpredicts axial tensile composite stiffness. Furthermore, since $\mathbf{A}^{Eshelby}$ is independent of fiber volume fraction, stiffness predictions increase linearly with v_f according to Equation 1.12 and as a result, Eshelby's solution is only accurate at very low volume fractions.

Mori-Tanaka model

The models presented so far focus on stiffness predictions for dilute composites. However, as often the case, strain fields around neighboring fibers can overlap. For this reason, Mori and Tanaka (Mori et al., 1973) proposed a modelling approach for non-dilute composite materials. The following discussion is based on Benveniste's simplified explanation of the Mori-Tanaka approach, according to which, when multiple identical particles are inserted in the matrix, the average fiber strain is

$$\bar{\boldsymbol{\epsilon}}^f = \mathbf{A}^{Eshelby}\bar{\boldsymbol{\epsilon}}^m \tag{1.29}$$

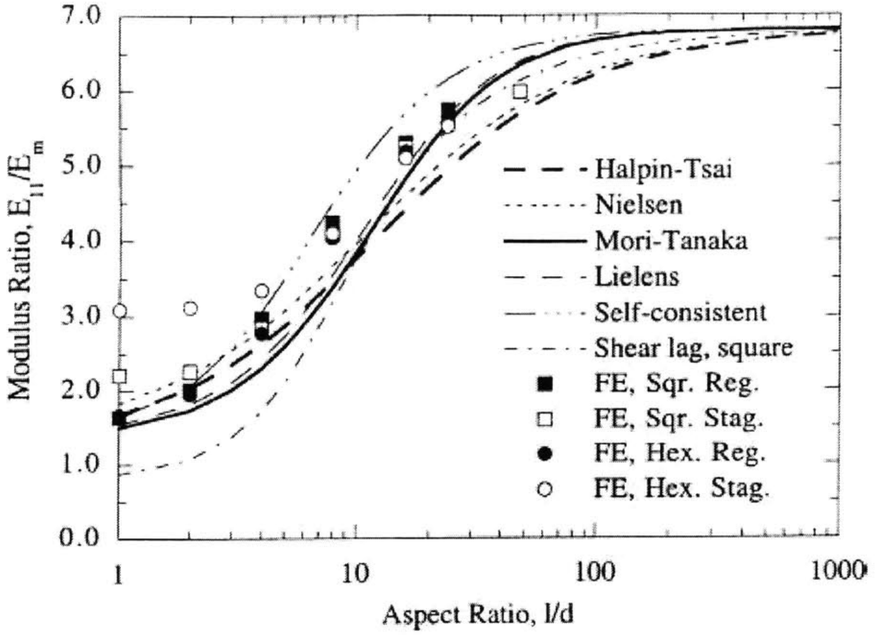

Figure 1-11: Model predictions and finite element analysis results for E_{11} (Tucker et al., 1999)

where the Eshelby strain concentration tensor maps the matrix average strain instead of the composite average strain to the fiber average strain. Then, according to Equation 1.10, $\hat{\mathbf{A}}^{MT} = \mathbf{A}^{Eshelby}$. By substituting in Equation 1.11, the Mori-Tanaka strain concentration tensor is given as

$$\mathbf{A}^{MT} = \mathbf{A}^{Eshelby}[(1 - v_f)\mathbf{I} + v_f\mathbf{A}^{Eshelby}]^{-1} \tag{1.30}$$

which is the basic equation for implementing the model.

Discussion

Figure 1-11 compares the various model predictions of E_{11} for various fiber aspect ratios and Table 1.3 lists all the relevant material properties. All moduli are normalized by the matrix modulus.

All models that were discussed earlier exhibit approximately similar S-shaped curves. Furthermore, at high aspect ratios, they approach asymptotically to the

Property	Fiber	Matrix
E	30	1
ν	0.20	0.38
v_f	0.20	
ℓ/d	1, 2, 4, 8, 16, 24, 48	

Table 1.3: Material properties used for the comparison of models (Tucker et al., 1999)

upper-bound value estimated by the rule of mixtures. At low aspect ratios, fiber composites behave increasingly as particle reinforced materials. In this case, the shear lag model performs the worst since it treats the fiber as a slender body. Overall, the Mori-Tanaka models seem to make the most reasonable predictions for composite E_{11} across a wide range of fiber aspect ratios.

1.2 Carbon nanotubes and carbon nanotube-reinforced composites

The discussion so far has provided an overview of the processing, structure and mechanical properties of traditional carbon fibers and vapor-grown carbon fibers and their composites and as such, it is highly relevant to carbon nanotubes and all issues related to them. Indeed, carbon nanotubes are strongly related to 3-D crystalline graphite and 2-D graphene layers (Dresselhaus et al., 2001a).

1.2.1 Processing, structure and properties of carbon nanotubes

The development of the chemistry of fullerenes by Smalley and his colleagues in the mid-1980's revealed tremendous possibilities to synthesize a whole new range of carbon structures of various shapes, sizes and dimensionalities (Ajayan et al., 1997), such as the buckminsterfullerene (C_{60} molecule), which was discovered first and is shown in Figure 1-3, or the C_{70} molecule, shown in Figure 1-12. Fullerenes are zero-dimensional,

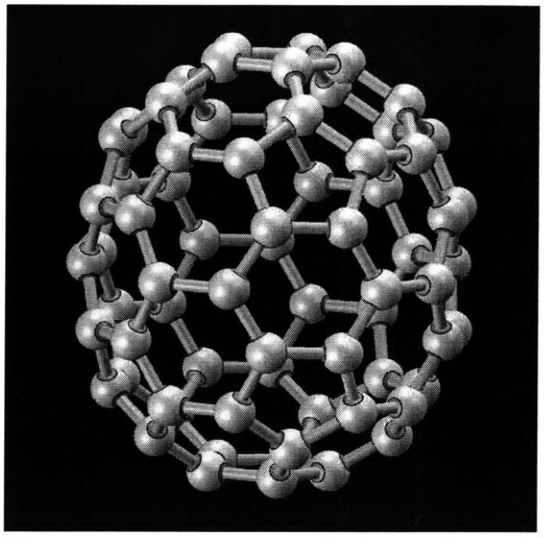

Figure 1-12: C_{70} molecule (http://www.chem.sunysb.edu/msl/, 2004)

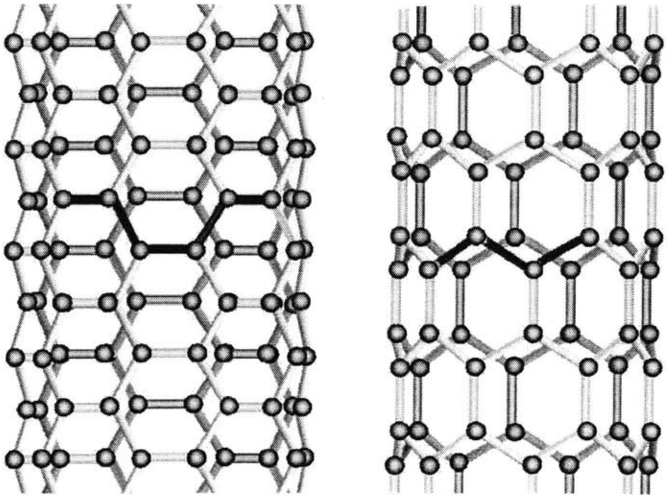

Figure 1-13: Atomic structure of a carbon nanotube wall (Thostenson et al., 2001)

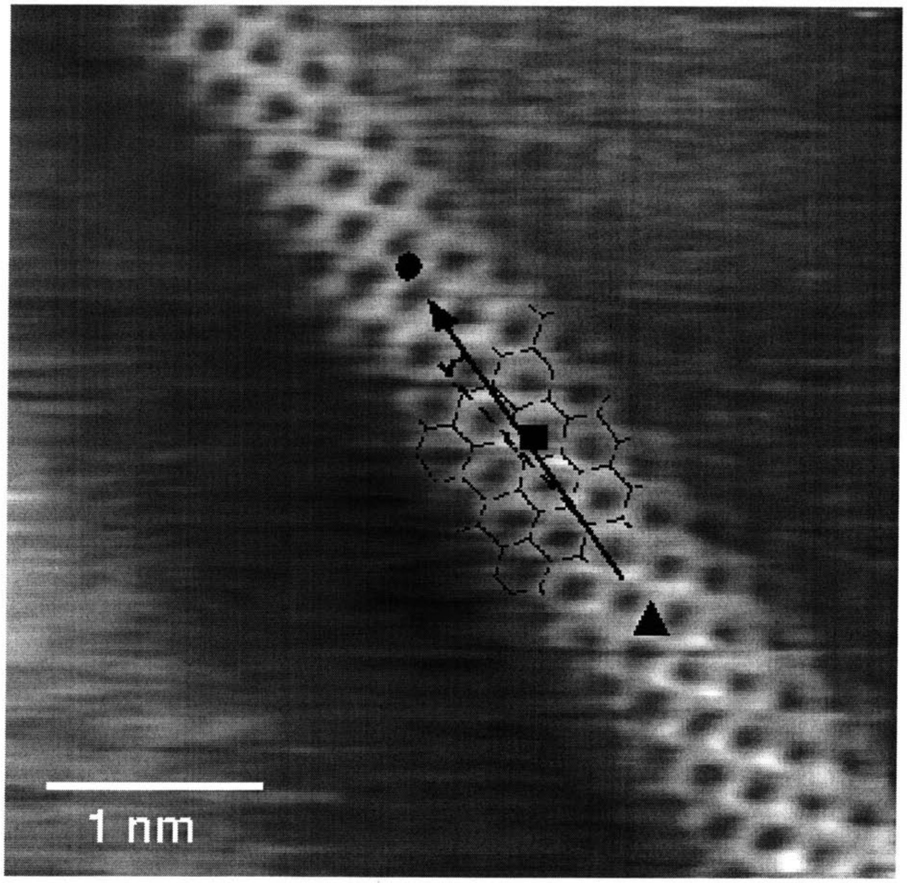

Figure 1-14: Single wall carbon nanotube with superimposed honeycomb pattern on the surface (Louie, 2001)

cage-like structures consisting of carbon atoms in their sp^2 hybridized bonding state, arranged in hexagonal and pentagonal configurations. Similarly, carbon nanotubes can be thought off as one-dimensional, cage-like structures with hexagonal carbon atom arrays and capped ends. A schematic of such a structure is shown in Figure 1-13.

Carbon nanotubes consist of honeycomb lattices representing a single atomic layer of crystalline graphite, called a graphene sheet, seamlessly rolled into a cylinder of nanometer size diameter. Carbon nanotubes fall under two categories, single-wall or multi-wall nanotubes, depending on the number of layers/tubes that comprise them. Figures 1-14 and 1-15 show a single wall and multi-wall nanotubes accordingly. Multi-

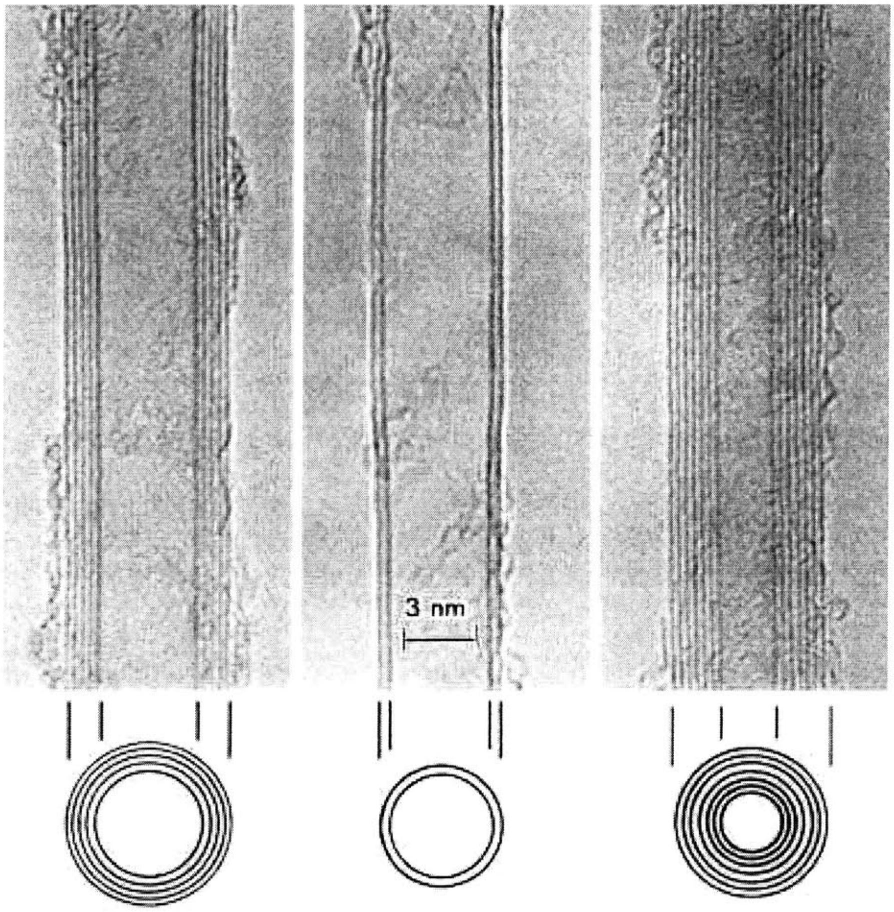

Figure 1-15: Multi-wall carbon nanotubes (Dresselhaus et al., 2001b)

wall carbon nanotubes consist of multiple concentric tubes of rolled-up graphene sheets, which interact with one another via secondary, van der Waals bonds, providing an interwall equilibrium spacing of $0.34nm$. Their diameter is on the order of tens of nanometers and their length is usually a few microns. Their structure resembles that of VGCFs but they are far more perfect. Single wall nanotubes on the other hand consist of a single graphene layer, as the name suggests, and are no more than a few nanometers in diameter, with similar lengths as multi-wall nanotubes. The single wall nanotube is considered to be the ultimate fiber of molecular dimensions, since it contains all of the in-plane strength and stiffness of graphite (Ajayan et al., 1997).

An important property of single wall nanotubes and of the walls of multi-wall nanotubes is their *chirality* or *helicity*. It is a topic that will be discussed in detail in a later chapter, in which a method will be presented that estimates the effective density of nanotubes based on their chirality. For this reason, only a brief mention of chirality will suffice at this point. The symmetric arrangement of carbon atoms on a graphene layer can lead to different crystallographic orientations of the carbon rings, when the sheet is rolled. Conceptually, chirality measures the degree of twist in the rolled graphene layer that results from these different possibilities. Chirality is expressed by the *chiral vector*, C_h, which connects two crystallographically equivalent sites on a graphene sheet (Dresselhaus et al., 2001b). In general, nanotubes can be either chiral or achiral, which in turn are divided into *armchair* and *zigzag* nanotubes, as shown in Figure 1-16. Nanotube chirality is discussed in further detail in Chapter 5.

Single and multi-wall carbon nanotubes can be produced by arc-discharge, laser ablation, gas-phase catalytic growth from carbon monoxide and chemical vapor deposition techniques, *CVD*, from hydrocarbons (Thostenson et al., 2001). Regardless of the process used, the nanotubes obtained contain varying amounts of impurities; multi-wall nanotubes produced by the arc-discharge method for example contain at least 33% polyhedral carbon clusters (Ajayan et al., 1997). As a result, subsequent purification is often required to remove such by-products. This is achieved by oxidation, often in a solution, by sonication and by centrifugation, all of which are more effective

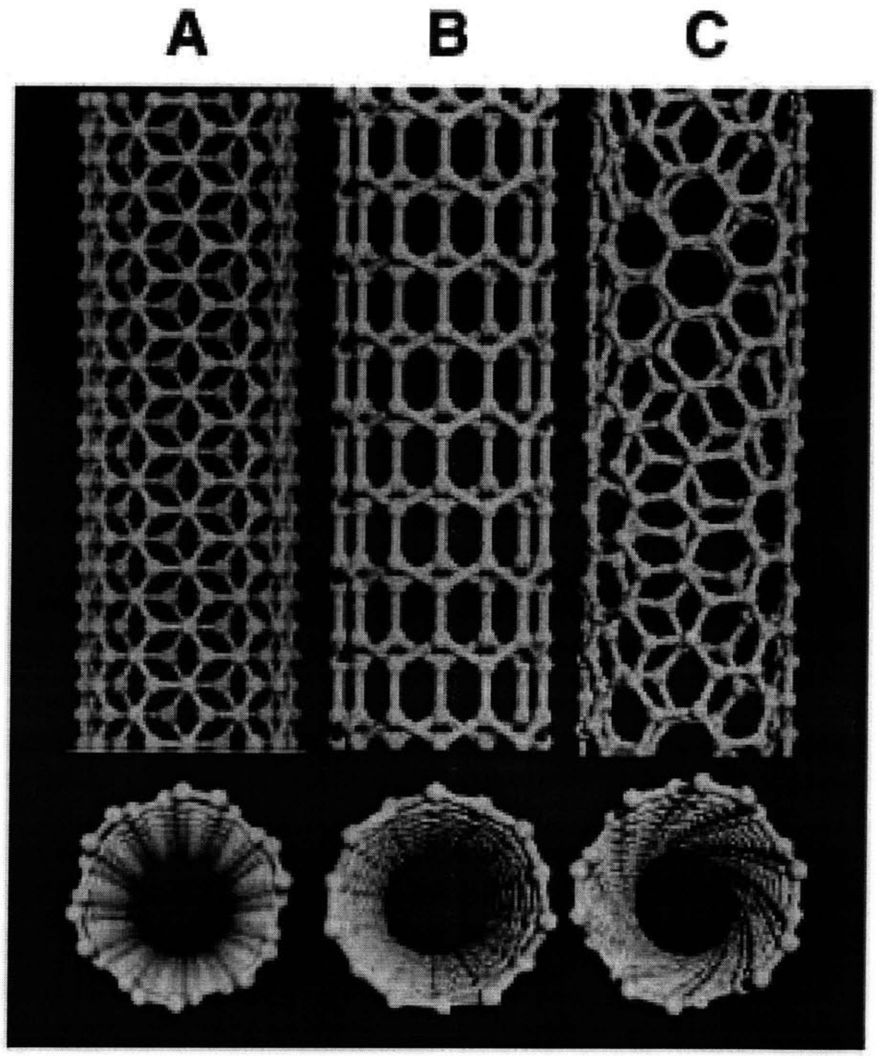

Figure 1-16: Illustration of chiral and achiral nanotubes (A: Armchair, B: Zigzag, C: Chiral (Baughman et al., 2002)

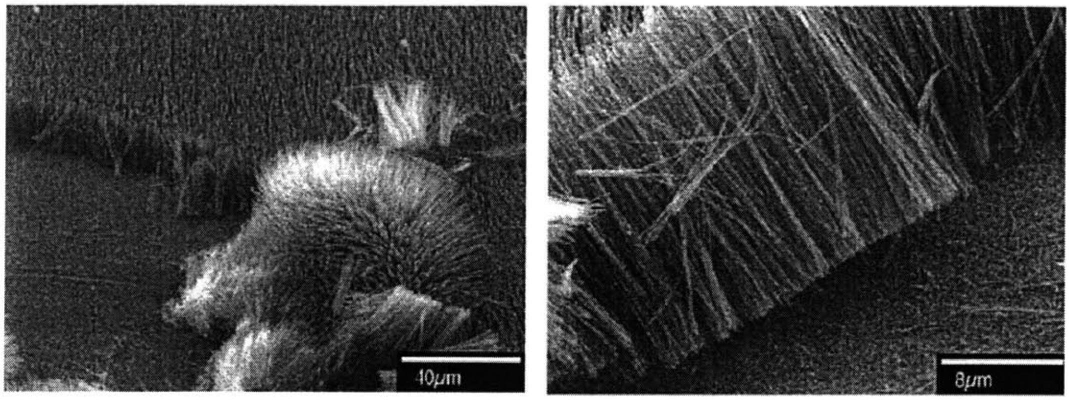

Figure 1-17: Micrograph showing "forest" of aligned multi-wall nanotubes (Thostenson et al., 2001)

in purifying multi-wall rather than single wall nanotubes. Nanotube alignment is also an important parameter and one in which CVD methods outperform other processing techniques. Among them, plasma-enhanced CVD results in the best alignment and uniformity of length and diameter. Figure 1-17 is a micrograph of PECVD-produced array of multi-wall nanotubes. Post-processing methods to untangle and align the produced nanotubes have also been developed.

The motivation in carbon nanotube research is partly founded on their promise for exceptional mechanical properties. Indeed, their molecular size and morphology allow the mechanical properties of carbon nanotubes to approach those of an ideal carbon fiber, with perfectly oriented graphene layers in the axial direction and a negligible amount of defects. The in-plane C-C covalent bonds are among the strongest bonds in nature and as such, they result in very high stiffness and strength values for carbon nanotubes in the axial direction.

Despite the intensity of research activity, the direct mechanical characterization of carbon nanotubes has been elusive for many years. The complete lack of micromechanical characterization techniques for direct property measurement, the difficulties involved in the manipulation of nanometer-sized particles and the uncertainty in data obtained from indirect methods have hindered the direct determination of the mechanical properties of carbon nanotubes. Furthermore, the resemblance of nanotubes

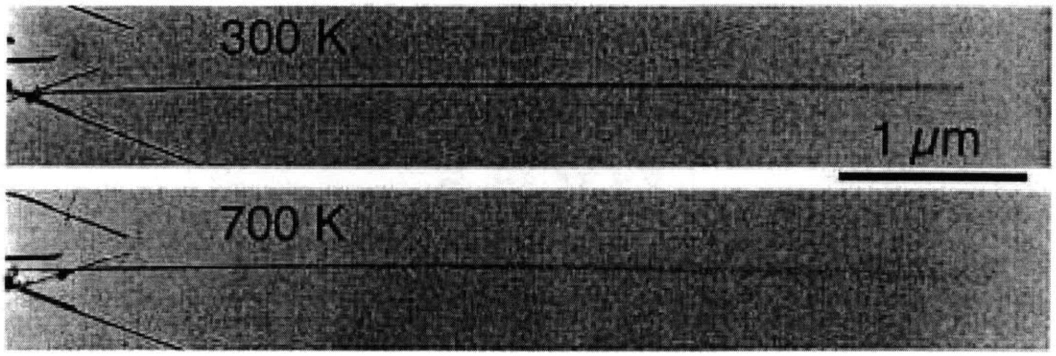

Figure 1-18: Blurring of multi-wall nanotube free tips due to thermal vibration (Yakobson et al., 2001)

to engineering structures, rather than solids adds to the complexity of their mechanical characterization. More specifically, the lack of spatial uniformity necessitates the coupling of any definition of material properties with appropriate assumptions about the geometry, such as the definition of an effective cross-sectional area and wall thickness(Yakobson et al., 2001).

The first direct experimental measurement of mechanical properties of carbon nanotubes was conducted by Treacy et. al (1996). In this case, the elastic modulus of multi-wall nanotubes, which were anchored on one side, was correlated to the amplitude of the thermal vibration at the free ends. The nanotubes were treated as hollow cylinders with finite wall thicknesses, cantilevered at one end, as shown in Figure 1-18. The average value for Young's modulus, over a number of nanotubes, that was obtained was $1.8TPa$, with significant scatter among the data for individual nanotubes and large error bars. This value is not considered to be very accurate, as it is relatively high, considering the corresponding in-plane elastic modulus for graphite, which serves as a reference point and is estimated at 1.06 TPa. Nevertheless, it is a strong indication of the exceptional axial stiffness of nanotubes. The same technique applied on single wall nanotubes yielded an average value of 1.25 TPa for the Young's modulus (Krishnan et al., 1998).

Direct measurement of the mechanical properties has also been achieved with the use of atomic-force microscopy, *AFM*. Wong et al. (1997) reported an average elastic

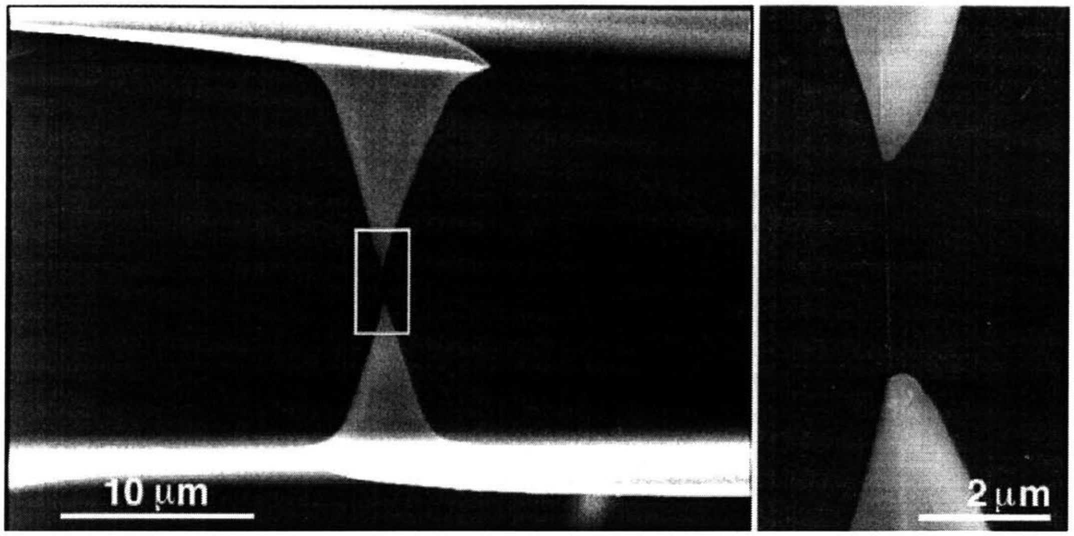

Figure 1-19: AFM apparatus for tensile loading (Yu et al., 2000a)

modulus of $1.28 \pm 0.59TPa$ and an average bending strength of $14.2 \pm 8.0GPa$ for multi-wall nanotubes that were cantilevered and loaded by an AFM tip at the other end. It was also found that these values do not depend on nanotube diameter. On the other hand, AFM techniques applied on single-wall nanotube bundles, or 'ropes', with diameters ranging from $3 - 20nm$, indicated that as the diameter of the bundle increases, both the axial and shear moduli decrease significantly due to the weakness of inter-tubular lateral adhesion (Salvetat et al., 1999). Multi-wall nanotubes and single wall nanotube ropes were also tested in tension using two opposing AFM tips and applying tensile loads (Yu et al., 2000a and Yu et al., 2000b), as shown in Figure 1-19. The experimentally determined strength and elastic modulus ranged from 11–63 GPa and 270–950 GPa accordingly. In both the single wall and multi-wall cases, the underlying assumption was that the outermost nanotube or wall in the assembly carried the load.

Finally, a recently developed technique allows the use of nanoidentation to determine the mechanical properties of vertically aligned carbon nanotube forests, a typical sample of which is shown in Figure 1-20. The experimental results, coupled with a micromechanical model yielded 0.90–1.23 TPa for the axial elastic modulus and 0.91–1.24 TPa for the bending elastic modulus (Qi et al., 2003). Assuming an

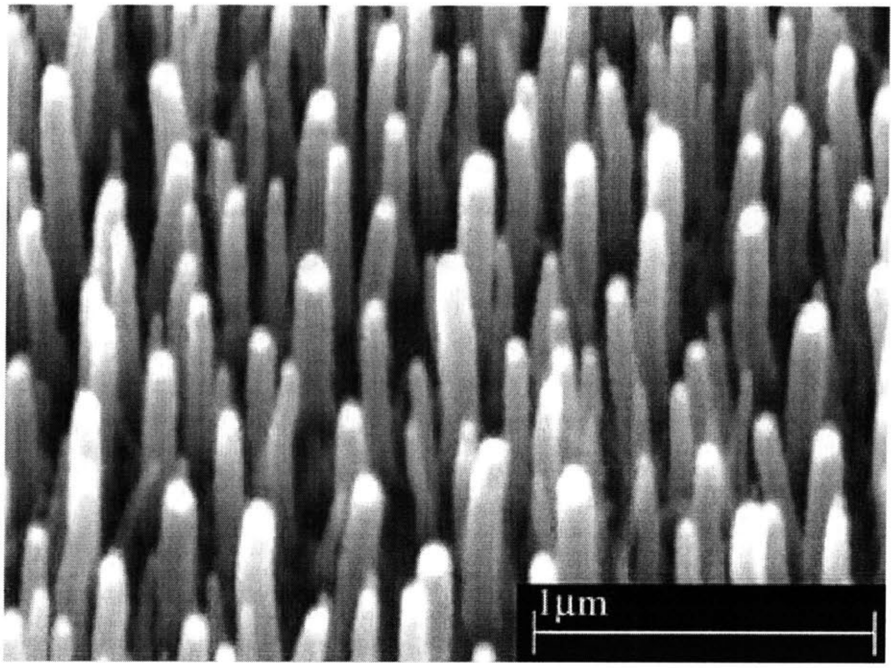

Figure 1-20: Vertically aligned carbon nanotubes (Qi et al., 2003)

effective nanotube wall thickness of 0.075 nm, these values result in a calculated effective wall modulus of 4.14–5.61 TPa, which is in agreement with predictions obtained from atomistic simulations (Pantano et al., 2004).

Besides high stiffness and strength, at least in the axial direction, carbon nanotubes demonstrate superior resilience. They can sustain extreme strain (40%), accommodating external forces without showing signs of brittleness, plastic deformation or atomic rearrangement and bond rupture. The reversibility of deformation has been verified under TEM and highlights the ability of nanotubes to recover from severe structural distortions (Ajayan et al., 1997). Adjacent multi-wall nanotubes often press into each other, flattening their walls and assuming ribbon-like shapes. At high number of walls, this does not occur due to the wall-to-wall van der Waals interactions. Similar flattening is observed in cases in which nanotubes are loaded in torsion, as shown in Figure 1-21. Another example of significant nonlinear deformation is the occurrence of kinks or ripples along multi-wall nanotubes when compressed or bent, captured in Figure 1-22. In all cases, the deformation is fully reversible, which

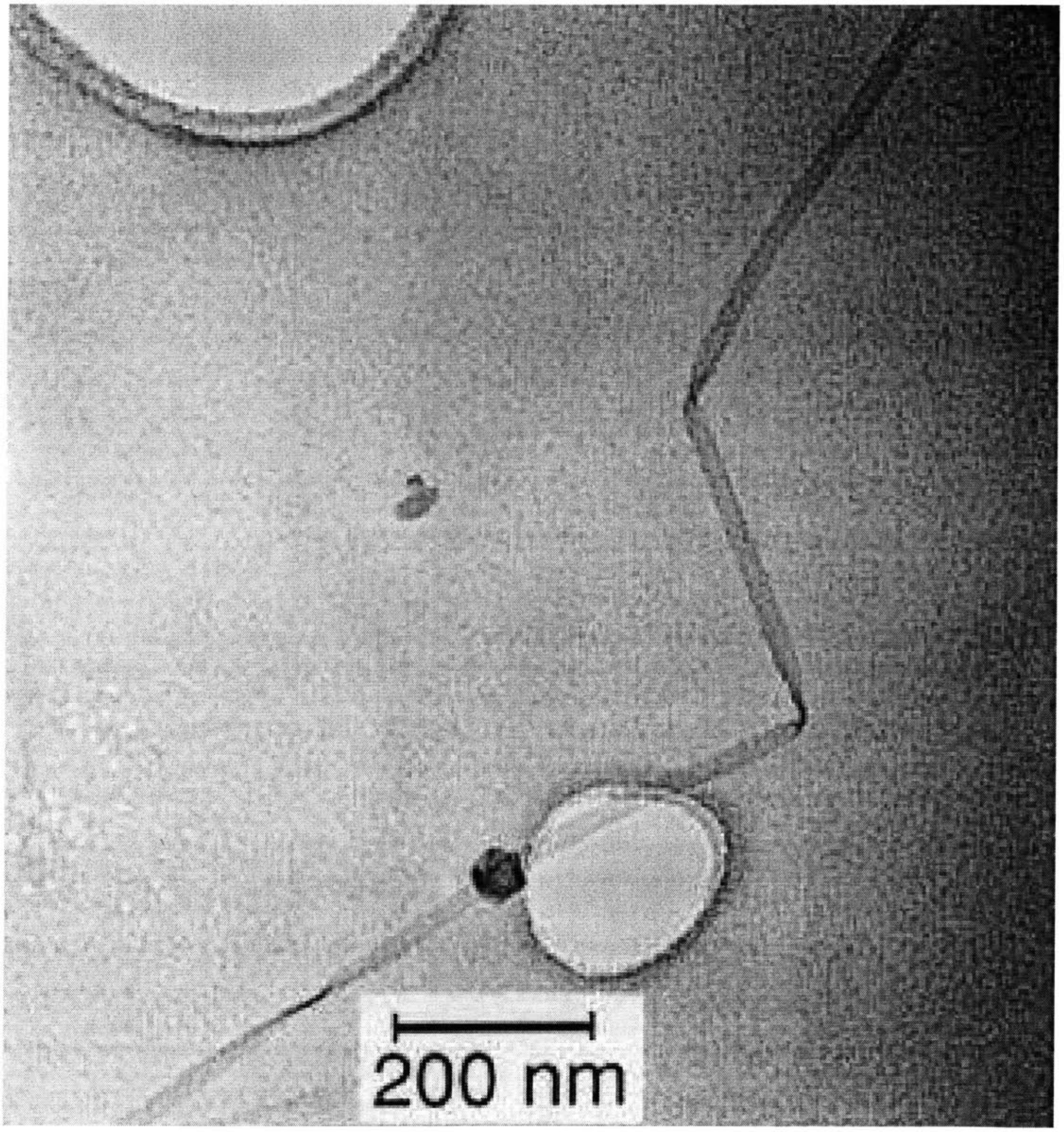

Figure 1-21: Collapsed nanotube, as observed in experiment (Chopra et al., 1995)

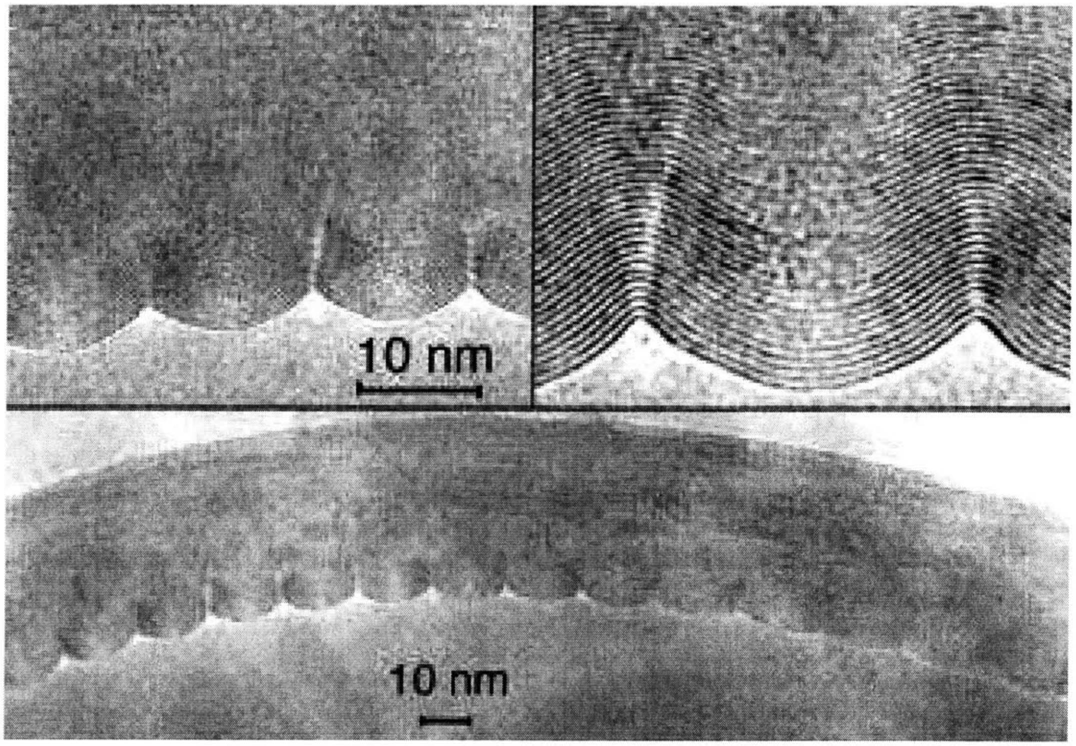

Figure 1-22: Bent multi-wall nanotube with typical wavelike distortion. Radius of curvature is 400 nm (Poncharal et al., 1999)

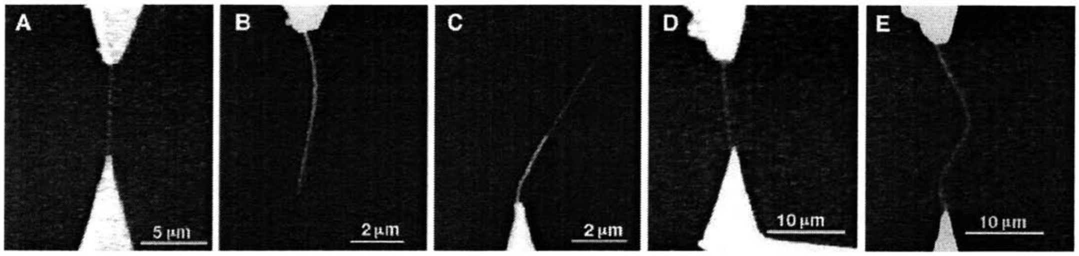

Figure 1-23: Telescopic, sword-in-sheath fracture behavior of a multi-wall nanotube loaded in tension (Thostenson et al., 2001

verifies the resilience of carbon nanotubes (Ajayan et al., 1997).

The actual strength of multi-wall nanotubes is compromised by the poor shear resistance of the van der Waals interactions between walls, which results in individual graphene cylinders sliding with respect to each other. The same factors contribute to the sword-in-sheath failure mode that is typical of multi-wall nanotubes, as shown in Figure 1-23. Such a failure mode cannot occur in single wall nanotube ropes, but individual nanotubes pull out by shearing along the rope axis in a similar fashion.

1.2.2 Properties of carbon nanotube-enabled composites

Recent work in the area of carbon nanotubes has focused on, among other issues, capitalizing on the exceptional mechanical properties of carbon nanotubes by developing nanotube-enabled composites. At the center of this activity as well as this thesis lies the use of polymers more than any other material as matrices.

There are three key parameters that affect the macroscopic mechanical behavior of carbon nanotube reinforced composites: filler geometry and dispersion; filler/matrix property ratio; and filler-matrix interfacial strength.

Nanotube geometry affects both the properties of the individual nanotubes in a composite as well as their reinforcing effect. The number of walls has a well-documented effect on the stiffness of nanotubes (Yu et al., 2000a). There have also been reports that the nanotube diameter of single wall nanotubes affects their stand-alone mechanical behavior at small diameters (Hernandez et al., 1998). Furthermore, recent experimental data suggests that the reinforcement scales linearly with total

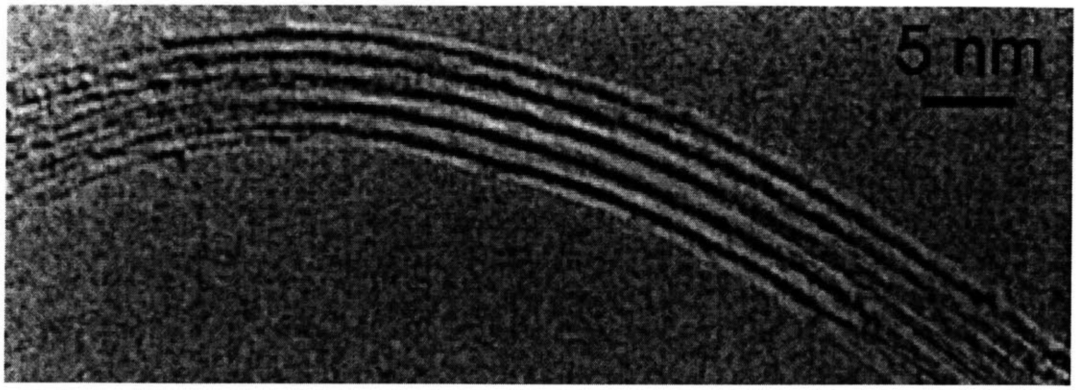

Figure 1-24: TEM image of single wall nanotube ropes (Salvetat et al., 1999)

nanotube surface area in thin films (Cadek et al., 2004).

Parameters such as nanotube dispersion and alignment as well as volume/weight fraction also influence the effectiveness of nanotubes as stiffeners. Poor filler dispersion in the matrix is often evidenced by the formation of aggregates of nanotube ropes, which results in nanotube slipping and affects the macroscopic behavior of the composite. Figures 1-24 and 1-25 show an example of a nanotube rope and the effect of rope diameter on mechanical properties accordingly. Furthermore, Gorga (2004) reported significant differences in tensile toughness between unoriented and oriented nanotube-reinforced composites (Figure 1-26) and concluded that unoriented nanotubes have in fact an adverse effect on tensile toughness. The effect of alignment is attributed to the ability of oriented nanotubes to bridge crazes and subsequent cracks, preventing them from growing into critical flaws.

Finally, a major issue that has limited the success of carbon nanotubes as reinforcements in composite materials has been the lack of strong interfacial bonding with the matrix, which limits load transfer from the matrix to the nanotube. There are three load transfer mechanisms: micromechanical interlock, chemical bonding and van der Waals interactions. Nanotubes are atomically smooth and have almost the same diameter and aspect ratio as polymer chains; as a result, no interlocking can occur. Interlayer sliding in the case of multi-wall nanotubes and nanotube-nanotube shearing in single wall nanotube ropes also contribute to poor load transfer.

There is conflicting experimental evidence on the strength of the matrix-nanotube

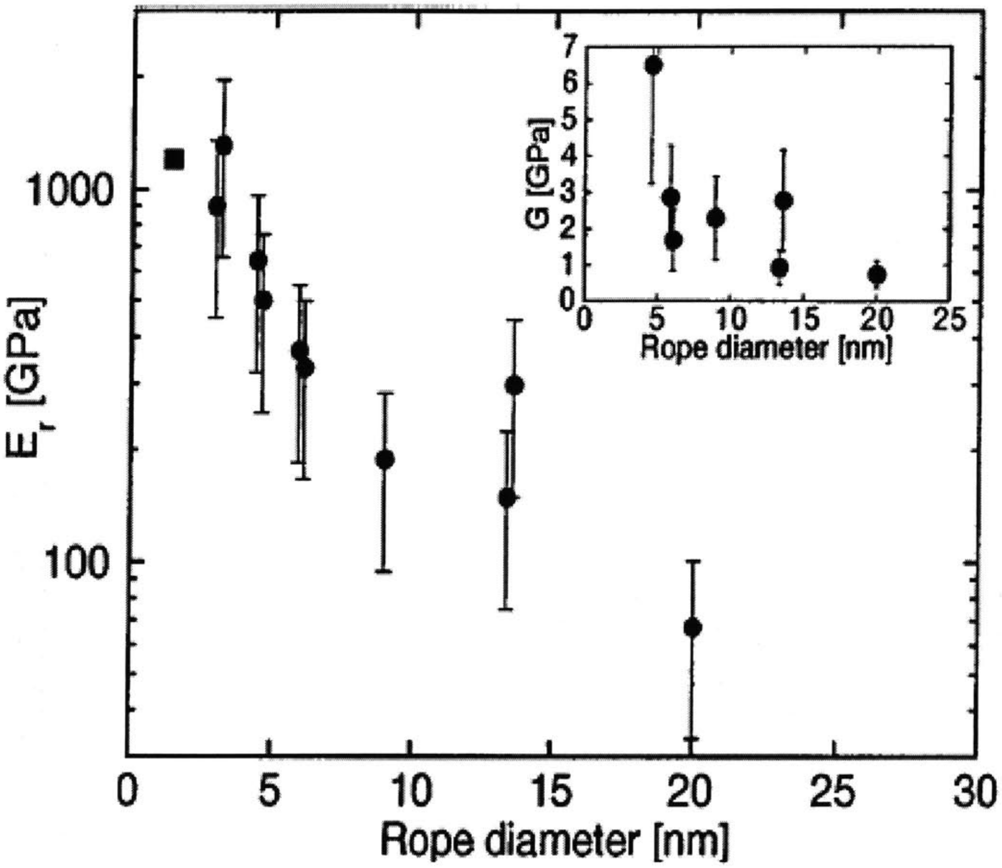

Figure 1-25: Effect of rope diameter on reduced modulus E_r and shear modulus G (Salvetat et al., 1999)

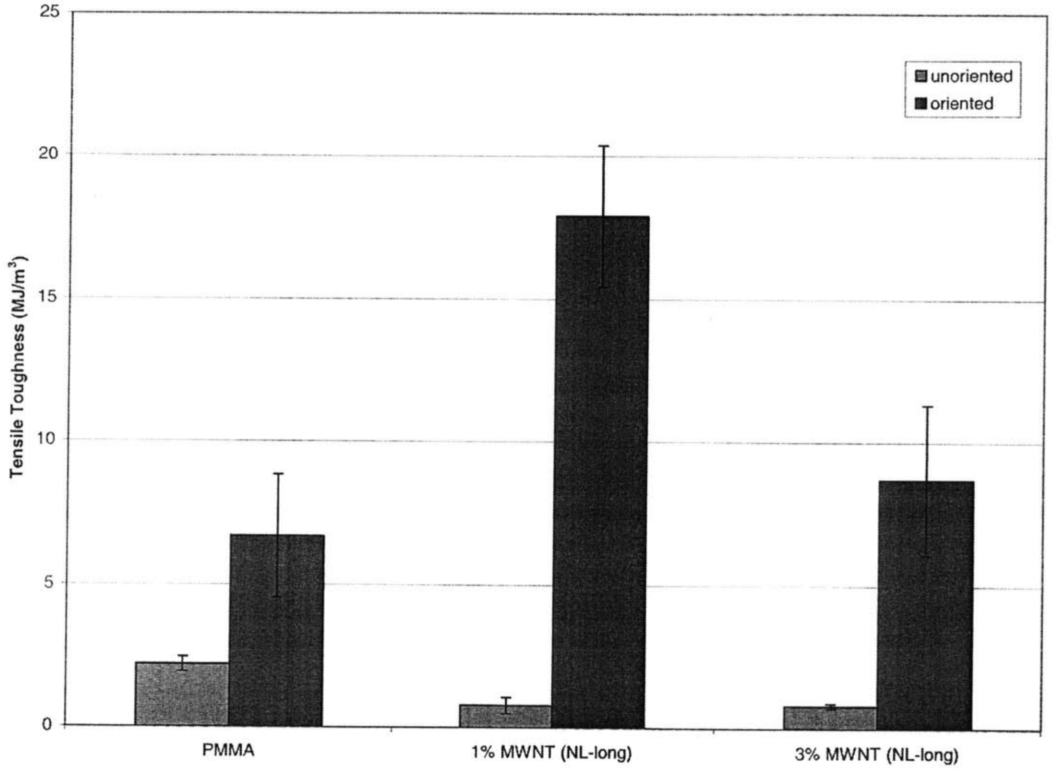

Figure 1-26: Effect of multi-wall nanotube orientation on composite tensile toughness for various nanotube weight fractions (Gorga, 2004)

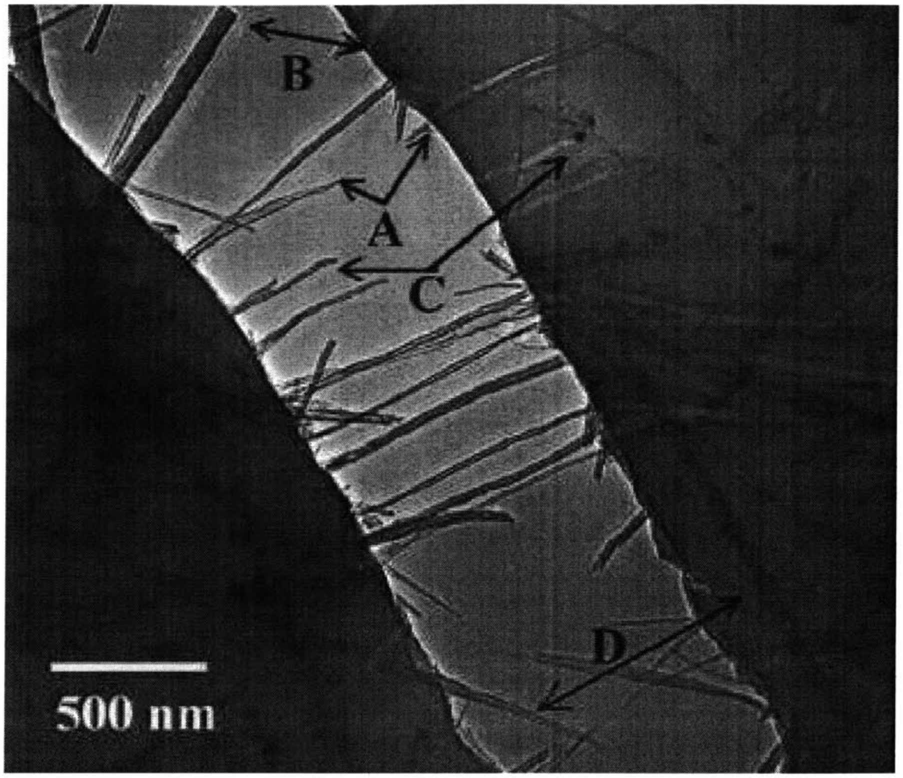

Figure 1-27: TEM observation of crack surface in a multi-wall nanotube-PS thin film (Qian et al., 2000)

interactions. Wagner et al. (Wagner et al., 1998) performed tensile tests on multi-wall nanotube-amorphous polymer composite film and reported interfacial shear stresses of over 500 MPa, which is higher than the amount of shear either the matrix or the nanotube itself can sustain. Schadler et al. (1998) and Ajayan et al. (2000) on the other hand have both suggested that the interfacial load transfer capability is poor. An important parameter that should be taken under consideration when evaluating these findings is the variation in the actual polymer used and in the processing conditions.

Such discrepancies in the interfacial bond strength become more apparent by close inspection of composite fracture surfaces. Figures 1-27 and 1-28 showcase different nanotube behaviors along a fracture surface. Overall, there is significant pull-out of the nanotubes from the matrix, which suggests low interfacial bond strength. Of those

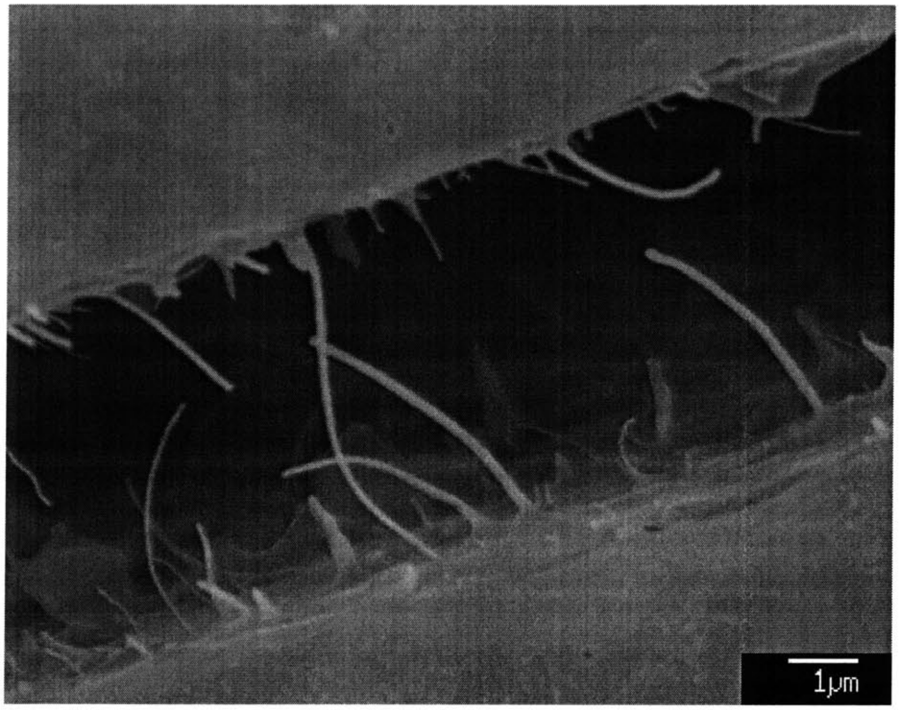

Figure 1-28: SEM observation of crack surface in a multi-wall nanotube-PMMA extruded strand

	Nanotube or fiber parameters				Composite tensile properties			
Composite 1 wt% loads	dia. (d) (nm)	length (l) (μm)	Ratio l/d	Modulus (MPa)	Strength (MPa)	Modulus (MPa)	Calculated modulus	Reference
Blank PS	···	···	···	···	12.8±1	1190±130 (E_M)	···	This study
PS+#1 MWNT	33.6	15	446	450	16±0.2	1620±130 (1.36E_M)	1.48E_M	This study
PS+#2 MWNT	30	50	1167	450	16±2	1690±130 (1.42E_M)	1.62E_M	This study
PP+VGCF	200	3.6	18	240	~28	~1.0E_M	1.06E_M	23
PS+$E-75$ fiber	9000	400	44	600	···	···	1.14E_M	24

Table 1.4: Tensile properties of multi-wall nanotube-PS composites (Qian et al., 2000)

Material	Density (Mg/m^3)	Tensile strength (GPa)	Tensile modulus (GPa)	Specific	
				Strength	Stiffness
Composites[a]					
E glass	2.1	1.1	45	0.5	20
Aramid	1.4	1.4	75	1.0	90
Type I carbon	1.5	1.1	220	0.7	130
Type II carbon	2.0	1.5	140	1.0	90
Metals					
Steel	7.8	1.3	200	0.2	26
Aluminium	2.8	0.3	73	0.1	26
Titanium	4.0	0.4	100	0.1	25

[a] Sixty percent fibre volume fraction unidirectional reinforcement.

Table 1.5: Mechanical properties of multi-wall nanotube-PBO composites (Kumar et al., 2002)

that remained attached to the matrix in Figure 1-27, the better-aligned nanotubes seem to break between the crack faces (nanotubes A and B), as opposed to those breaking inside the matrix (nanotube D). Finally, some nanotubes fail at obvious defects, such as nanotube C, which failed at the catalyst particle.

Reports of the actual macroscopic properties of nanotube reinforced composites vary significantly, and no firm conclusion can be drawn. Qian et al. (2000) achieved between 36–42% increase in the elastic stiffness and 25% increase in the tensile strength by adding only 1% by weight multi-wall nanotubes in polystyrene. The samples were prepared by employing a solution-evaporation method, assisted by high-energy sonication to produce uniform composite films. Table 1.4 summarizes these findings, which include reinforcing effects of nanotubes of different aspect ratio. Kumar et al. (2002) also reported an increase in strength and stiffness of single wall

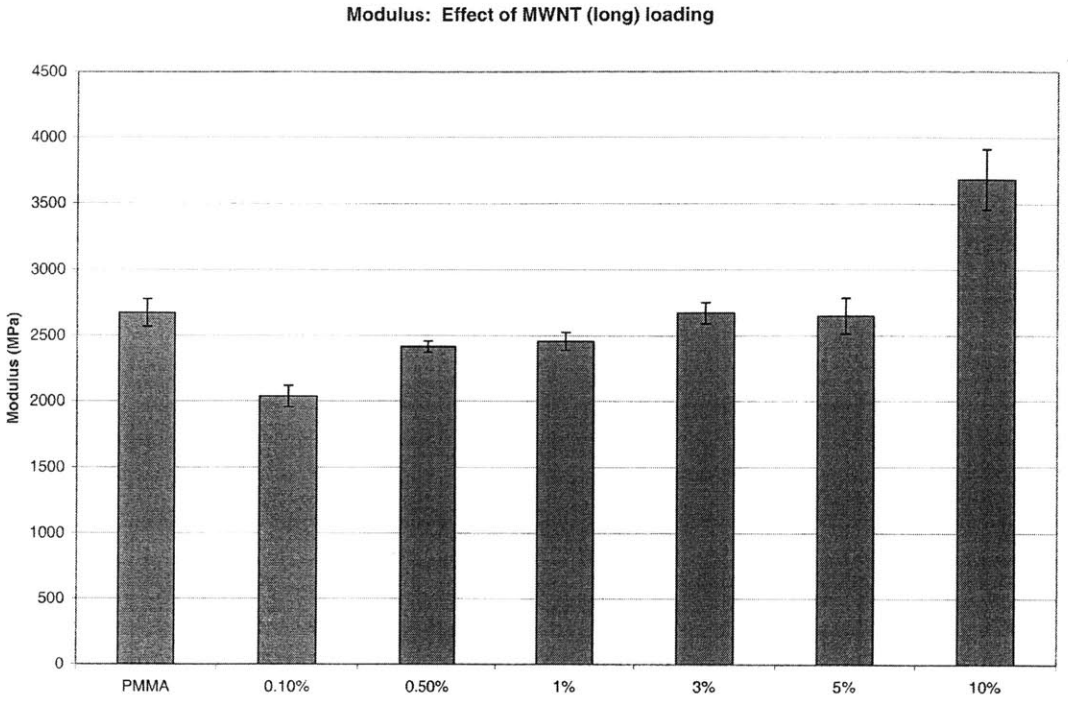

Figure 1-29: Elastic modulus of multi-wall nanotube-PMMA composites (Gorga, 2004)

nanotube-PBO composites, albeit less dramatic, as suggested by Table 1.5. On the other hand, Gorga et al. (2004) observed either a decrease or no change in the elastic modulus of multi-wall nanotube-PMMA composites at filler loadings up to 5% by weight and a noticeable increase at 10% (Figure 1-29). The opposite trend is apparent in the tensile toughness data, which show an increase at low weight fractions and a decrease to values below those for pure polymer at higher weight fractions (Figure 1-30). It seems therefore that no universal conclusion about the performance of carbon nanotubes as reinforcement can be drawn at this point. Research into parameters such as nanotube geometry and dispersion, interfacial bonding as well as investigation into different matrix systems will hopefully enable the full exploitation of the exceptional mechanical properties of carbon nanotubes.

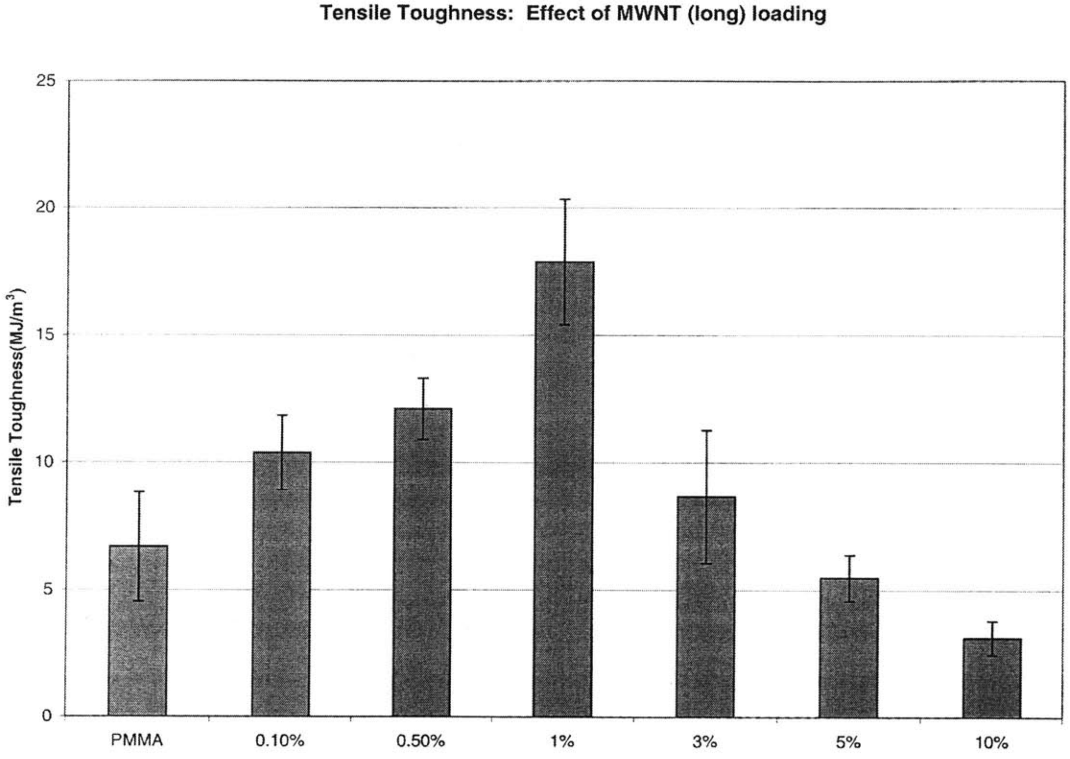

Figure 1-30: Tensile toughness of multi-wall nanotube-PMMA composites (Gorga, 2004)

Chapter 2

Analysis and simulation of nanotube dispersion in a matrix

The importance of nanotube dispersion and alignment in a matrix and their influence on the macroscopic mechanical properties of a composite were briefly introduced in the previous chapter. A number of authors have emphasized the adverse effects of nanotube debonding and clustering on macroscopic stiffness and toughness, which can be attributed to the resulting wall-to-wall sliding. Du et al. (2003) used a coagulation method that presumably leads to better dispersion of nanotubes, as evidenced by the lack of agglomerates upon visual inspection of micrographs as well as by the increased perceived viscosity of the composite (purified single wall nanotubes in PMMA) during melt-spinning. By comparing their experimental results for the axial elastic moduli of the samples ($\sim 4.3GPa$ for a 1% by weight composite) to the values obtained by Haggenmueller et al. (2000) ($\sim 3.3GPa$) for similar samples with less uniform dispersion, Du et al. (2003) concluded that better dispersion results in higher axial stiffness for a given nanotube-polymer system.

As a result, given the importance of nanotube spatial distribution in a matrix, it is essential to quantify and characterize nanotube dispersion for an actual composite sample as well as to model it. For the experimental aspect of this work, multi-wall carbon nanotube-PMMA samples were initially studied using TEM and nanotube dispersion was later evaluated through image analysis of the captured micrographs.

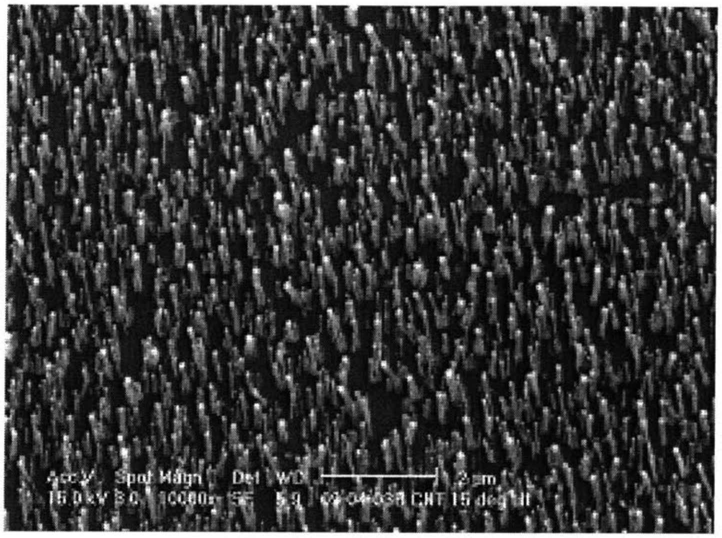

Figure 2-1: Multi-wall nanotube forests provided by Cambridge University

The next step was to model this dispersion, which would provide better insight into the spatial arrangement of nanotubes and would also facilitate finite element modelling. Thus, overall there were two objectives for this study. The primary goal was to evaluate nanotube dispersion in actual composites that were produced at MIT. This would shed light on the effectiveness of the processing technique being used and would also enable its correlation to measured macroscopic mechanical, electrical and thermal properties. A second goal was to accurately define a realistic representative volume element (*RVE*) to be used in models and simulations. This would be achieved by measuring the lateral and longitudinal spacings between nanotubes and extracting a statistical average from this data to determine the aspect ratio of the model RVE.

2.1 Experimental investigation of nanotube dispersion in a polymer matrix

The composite system that was selected for this purpose consisted of PMMA (Plexiglass V920) and aligned multi-wall nanotubes, provided by Cambridge University, similar to those shown in Figure 2-1. The length of the nanotubes was $55\mu m$ and

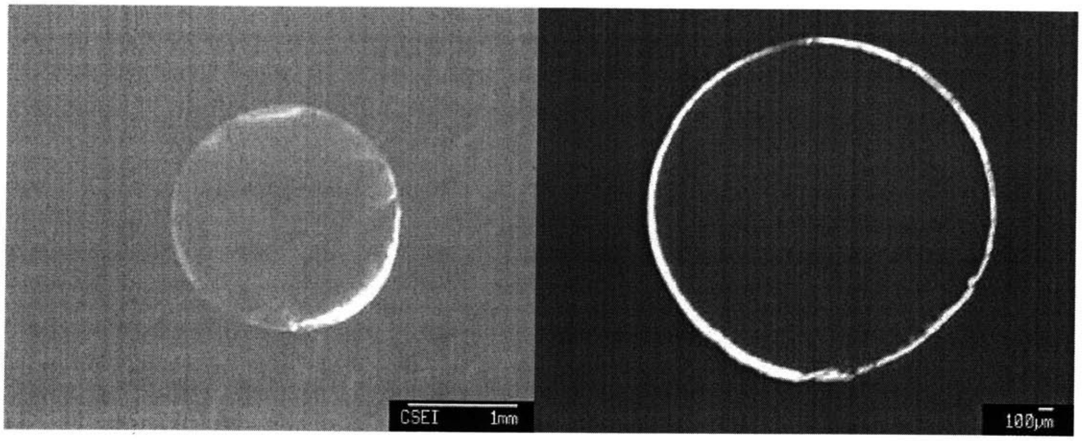

Figure 2-2: Bright rings on the 3% and 5% samples

their diameter was estimated from the micrographs to range between 50 and 100 nm. The nanotubes and PMMA were dry-blended and fed into an extruder at 230^oC for 10 minutes. The extruded strands were 2.5 mm in diameter and the particular samples that were selected contained 1%, 3% and 5% multi-wall nanotubes by weight, although subsequent image analysis efforts focused on the 5% samples exclusively due to their better fit to the goals of this study. Micrographs were taken using a JEOL JSM6340F SEM, located at Cambridge University.

2.1.1 Qualitative analysis

Initial images revealed a bright ring at the perimeter of the composite strand cross-section, as shown in Figure 2-2. Such rings appeared consistently in the 3% and 5% by weight samples and had a fairly constant thickness all around, except in areas whose morphology was affected by the insertion of the razor during cutting. From Figure 2-3, which shows close-ups of two diametrically opposite points on a 5% by weight strand, the ring thickness can be estimated at $40\mu m$ for both locations.

A number of factors can lead to the appearance of such rings. It can be attributed to the conductivity of the composite strand and its variation from the surface to the center. It could also be attributed to the morphology of the fracture surface and finally, it could simply be due to poor grounding.

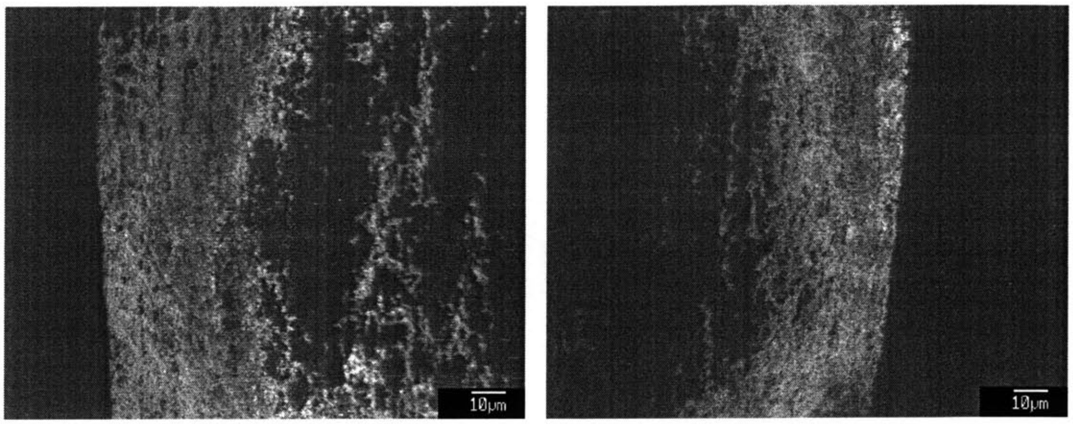

Figure 2-3: Close-ups of the bright ring on two opposite points on the surface of a 5% strand

It is well-established from literature that the conductivity and percolation rate of a composite depends heavily both on the dispersion as well as the alignment of the filler. Du et al. (2003) reported that the conductivity of unoriented purified single wall nanotube-PMMA samples was higher than that of oriented samples by a factor of 10^6. Measurements were taken for 2% by weight specimens and clearly indicated that unoriented samples had a lower percolation rate than oriented samples, as shown in Figure 2-4. Comparison with previous results for the conductivity of agglomerated, non-uniformly dispersed nanotube composites reported by the same group, indicates that besides alignment, conductivity is also affected by dispersion. Schueler et al. (1997), while studying the agglomeration process of carbon black particles, also found a correlation between percolation rate and dispersion. Sandler et al. (2003) studied the effects of nanotube entanglement on the formation of conductive networks in a composite and were able to achieve percolation rates for the non-entangled nanotubes that were an order of magnitude lower than the best results previously achieved with entangled nanotubes. Therefore, if a difference in conductivity between the strand edge and the core is causing the appearance of the bright rings in the micrographs, then one of two scenarios are plausible: there is a difference either in filler concentration or in filler dispersion and alignment between the edge and the core. Note that, since conductivity remains constant above the percolation threshold (Du et al.,

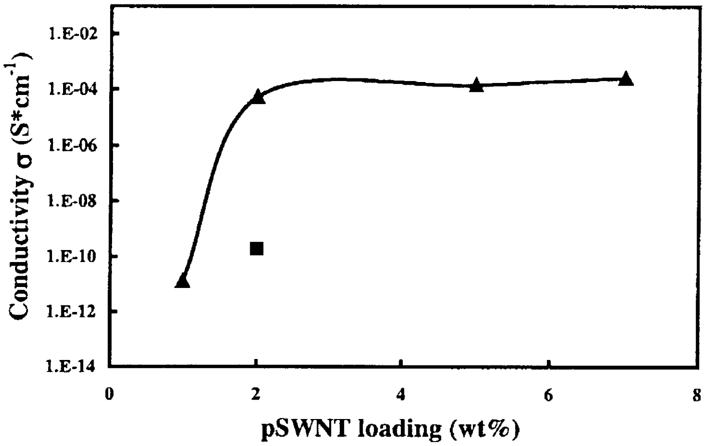

Figure 2-4: Electrical conductivity of purified single wall nanotube-PMMA composites, both (▲) unaligned and (■) aligned, as a function of nanotube loading (Du et al., 2003)

2003) and the rings appear both at the 3% and the 5% by weight samples, either hypothesis implies that such differences would be large enough to cause one of the two locations (the edge or the core) to be conductive and the other non-conductive. As it will be shown later, image analysis dismisses the existence of a large gradient in filler concentration from the edge to the core. It also shows a uniform dispersion throughout the cross section of the strand. Thus, if it is indeed an issue of composite conductivity, then only a significant difference in alignment between the edge and the core would explain the presence of the rings.

Topography could also account for the brightness at the perimeter of the strand cross section. If the edge was elevated relative to the core, then that would cause it to appear brighter. However, the cutting of the strand by a razor does not justify such a variation. Furthermore, the presence of the ring even at the lower right quartile of the strand, where the razor was first inserted creating an inclined surface, also serves as proof that morphology cannot account for the rings.

Finally, insufficient grounding of the specimen can result in charging effects, which may be evidenced by the aforementioned bright rings around the perimeter. In this study, samples were grounded using carbon black tape and the possibility of poor grounding is certainly realistic.

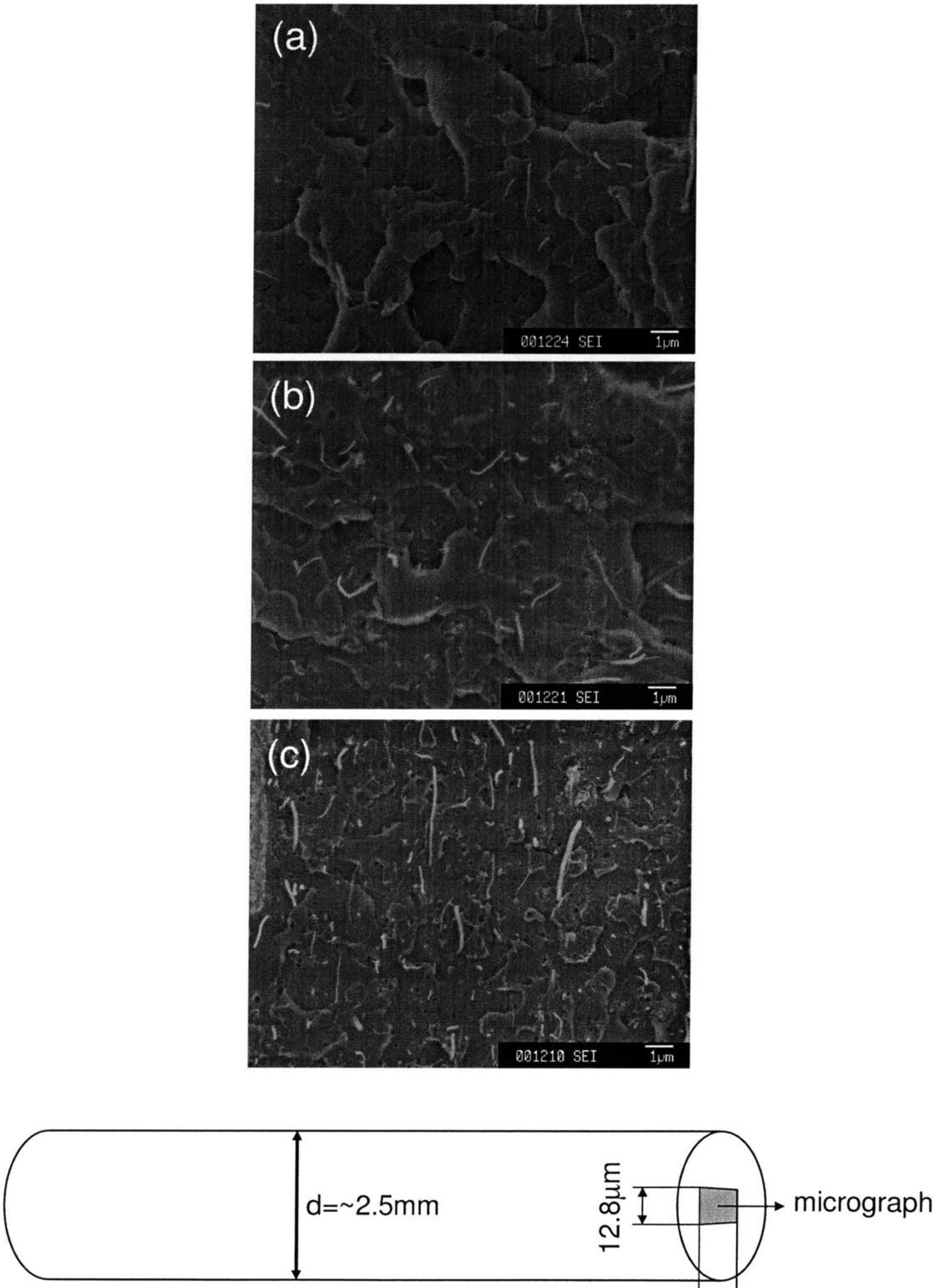

Figure 2-5: a) 1%, b) 3% and c) 5% by weight as-is samples of multi-wall nanotube-PMMA composites sectioned perpendicular to the strand axis

Figure 2-5 shows same-scale micrographs of three samples (1%, 3% and 5% by weight), cut perpendicular to the strand axis. A number of qualitative remarks can be made by simple observation of these images, taken sufficiently far away from the edge of the strand. First, nanotube dispersion is uniform at all three nanotube load levels and, as expected, nanotube packing density increases noticeably with weight fraction. Second, the morphological features of the fracture surfaces, although similar in structure, seem to scale down in size as the nanotube concentration increases. Third, there is widespread nanotube pull-out across the fracture surface, which implies poor interfacial strength. Pull-out is evidenced both by the suspended nanotubes, which remained attached to the sample part in the micrograph, and by the dark voids, which are the coupled locations of the nanotubes that remained attached to the half that was cut-off. Finally, there is significant variation in the diameters of the nanotubes. This can be explained partly by the variation in the as-received nanotube forests but it can also be attributed to potential fracture of the external walls of the pulled-out nanotubes, which would expose the inner, smaller-diameter walls. This may suggest that the interfacial bond between the external walls and the polymer has a higher strength than the nanotube walls themselves.

These samples were also examined axially. Due to the brittleness of the composite, it was not possible to fully control the direction of the cut and consequently, the fracture surfaces were at a slight angle off of the strand axis. Figure 2-6 shows a micrograph of such a surface, with the strand axis being horizontal in this capture. Note that although the samples depicted in Figures 2-5c and 2-6 are identical and were cut with the same technique, there are virtually no pulled-out nanotubes in the axial sample, as opposed to the perpendicular sample, in which pull-out is widespread. The implication is that there are no nanotubes oriented transversely to the strand axis. Furthermore, perceived packing density is much lower in the axial sample, as evidenced by the small number of visible nanotubes and, among the nanotubes that are exposed at the surface, most are aligned with the strand axis. Therefore, comparison between the axial and the perpendicular samples suggests that the nanotubes, besides being well-dispersed, are also fairly well aligned.

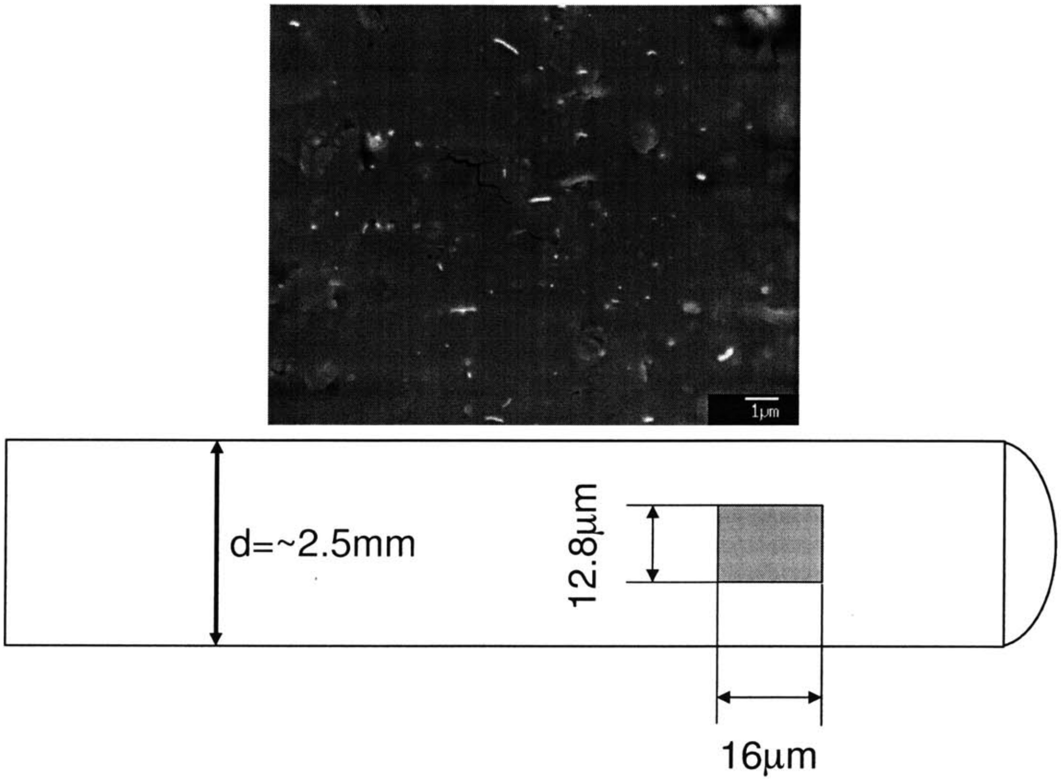

Figure 2-6: Axial cross-section of a 5% by weight as-is sample of multi-wall nanotube-PMMA composite

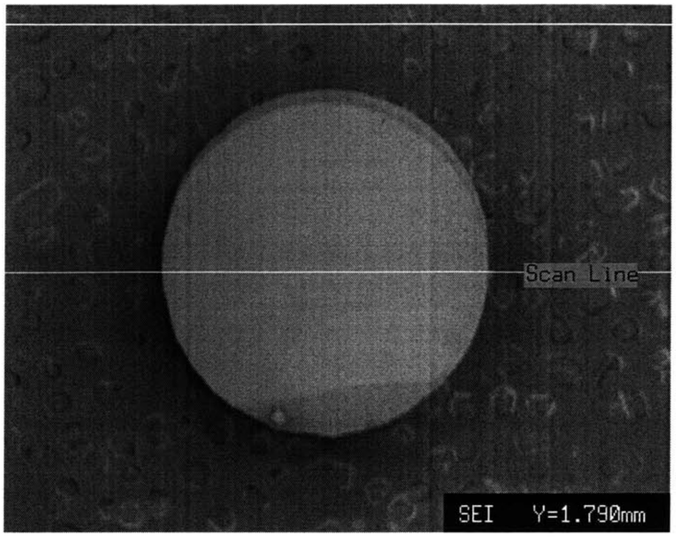

Figure 2-7: Micrograph capture scan line from the edge of the sample strand to the core

The samples in Figures 2-5 and 2-6 were cut with a razor and examined as-is. Although they offer useful qualitative information about the composite, the roughness of their surface and the presence of suspended nanotubes hinders any efforts to analyze their micrographs and extract statistical information about filler distribution. A number of parameters affect filler visibility and contrast between filler and matrix, such as the cutting method, polishing, etching and coating. It is often quite challenging, as it was in this case, to strike an optimum balance among these factors, particularly polishing and etching. Cutting the strands with a razor resulted in brittle fracture and rough surface, that exposed pulled-out nanotubes, but could not offer much to image analysis. The use of a glass tip to microtome the strand, coupled with polishing resulted in a very smooth surface morphology, with clearly distinguishable nanotubes. Etching was attempted using acetone for 10 seconds but proved to be detrimental, as it blurred the nanotube-PMMA boundaries and was therefore abandoned.

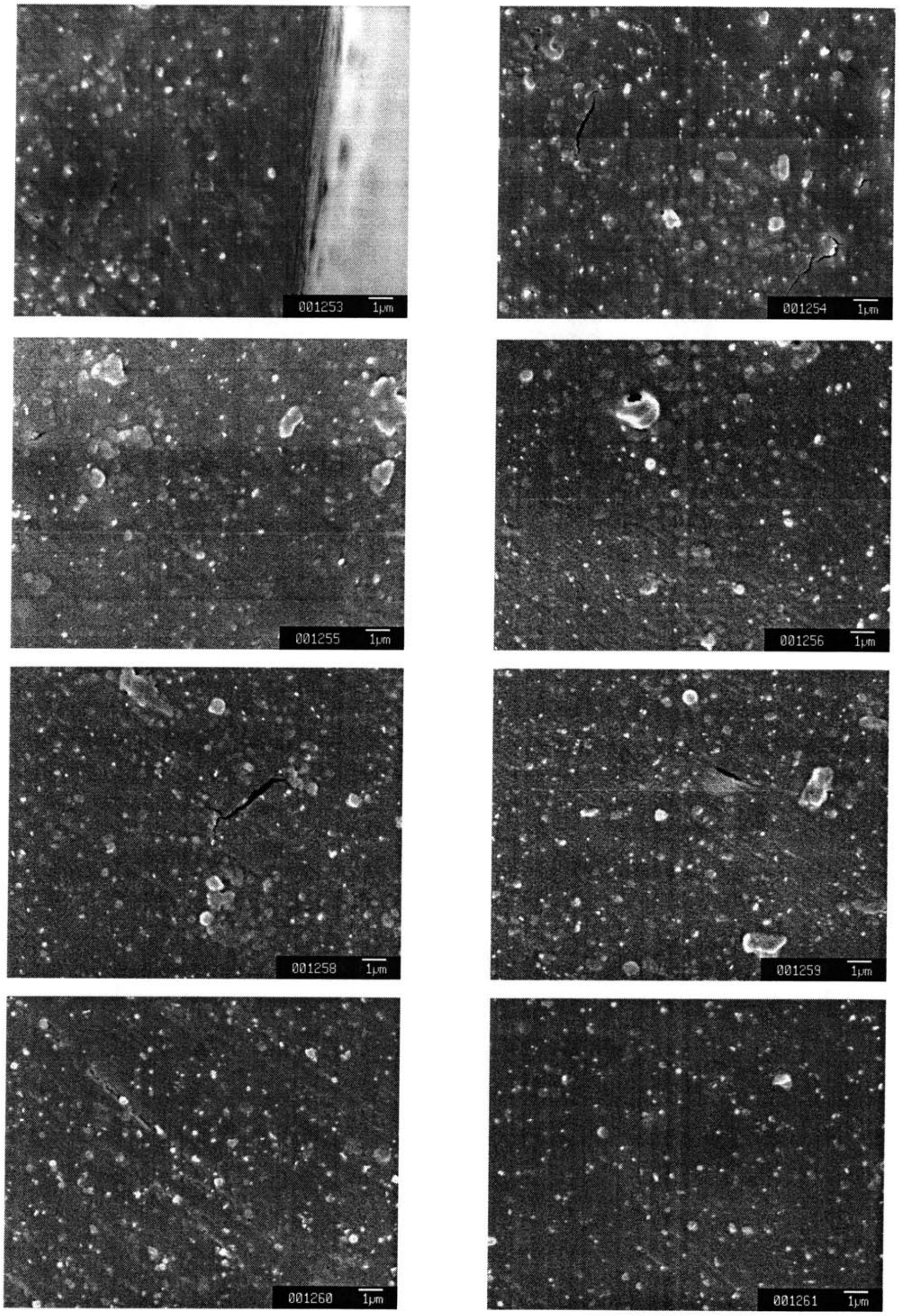

Figure 2-8: Series of micrographs of the 5% by weight sample, captured in order from the edge to the core of the strand

Image ID	Distance from the edge (mm)
1253	0
1254	0.02
1255	0.04
1256	0.065
1258	0.115
1259	0.165
1260	0.867
1261	1.366

Table 2.1: Location of micrographs in Figure 2-8

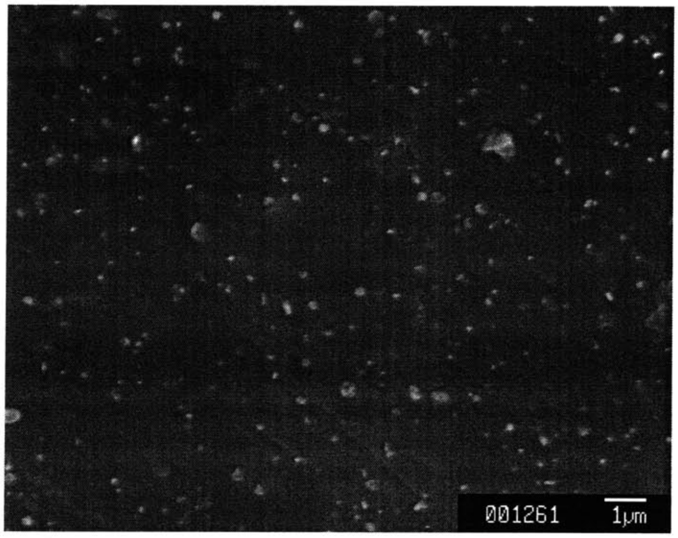

Figure 2-9: Micrograph of the core region of a 5% by weight, microtomed and polished sample of multi-wall nanotube-PMMA composite

2.1.2 Quantitative analysis

In order to investigate any potential differences between the edge and the core of the strand, in terms of degree of clustering and filler concentration, a series of micrographs were taken radially from the edge to the core, as shown in Figure 2-7. All micrographs are shown in Figure 2-8, in the order they were captured, from the edge to the core and the locations of the captures are indicated in Table 2.1. Figure 2-9 shows a micrograph of a sample, with 5% by weight multi-wall nanotubes, which was microtomed, polished and coated before being examined. This particular image was taken 1.4 mm from

Figure 2-10: Processed micrograph of a 5% by weight composite sample (length scale is identical to Figure 2-9)

the edge, inside the core region of the strand. Image analysis was conducted on this micrograph using ImageJ, a software available for free from NIH. A number of macros were coded to tailor its capabilities to the needs of this study. The images were thresholded in terms of their brightness in order to create a binary replica of the micrograph that would enable the visual separation of the nanotubes from the matrix. Figure 2-10 shows the micrograph from Figure 2-9 after it has been converted into a binary image. The apparent variation in particle size is a direct result of clusters of nanotubes appearing as single particles. This highlights the importance of the image processing step and its effect on the extracted data. There is no standard procedure to perform the necessary steps, since the brightness, contrast, sharpness, etc. of each micrograph varies greatly. Sample preparation, image capturing technique and thresholding settings are among the parameters that ultimately affect the quality of the processed image and the accuracy of particle identification. For this particular micrograph, accuracy was verified by comparing the weight fraction, as calculated from the image, with the actual weight fraction of 5%. Image analysis yielded a particle area fraction of 3.4%. Assuming an average nanotube diameter of 75 nm, which corresponds to a nanotube density of $2.1g/cm^3$ and a documented PMMA

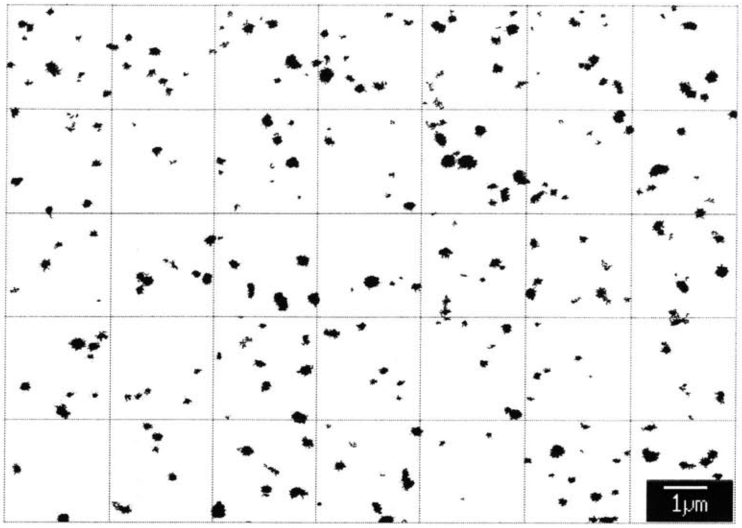

Figure 2-11: Illustration of scanning box (length scale is identical to Figure 2-9)

density of $1.17g/cm^3$, a simple calculation yields a weight fraction of 6.3%, which is reasonably close to the reported value (5%). More details about the connection between nanotube diameter and density will be presented at a later chapter.

A macro was formulated to obtain the particle count from the micrograph. The area that was captured in the image was $16\mu m$ in width and $12\mu m$ in height. A square box was created to scan the entire micrograph from left to right and top to bottom. At each snapshot, it recorded the particle count in its enclosed area and the focus area was then shifted by half an edge length to the right or, in case it was on the right edge of the micrograph, it wrapped around to the left edge, half an edge length lower than its prior position. As a result, a 50% overlap was maintained throughout the scanning process, thus providing 'smoothness' in the recorded data, which would facilitate its graphical representation. Furthermore, the area of the box was varied to capture the size scale at which this method transitions from capturing global dispersion to identifying localized clustering. For this reason, three square scan boxes were created with 2, 4 and $8\mu m$ long edges, respectively. Given that the average particle area was $0.017\mu m^2$, these box sizes were appropriate and reasonable for the specific study. Figure 2-11 illustrates consecutive positions of a scanning box, without the overlap.

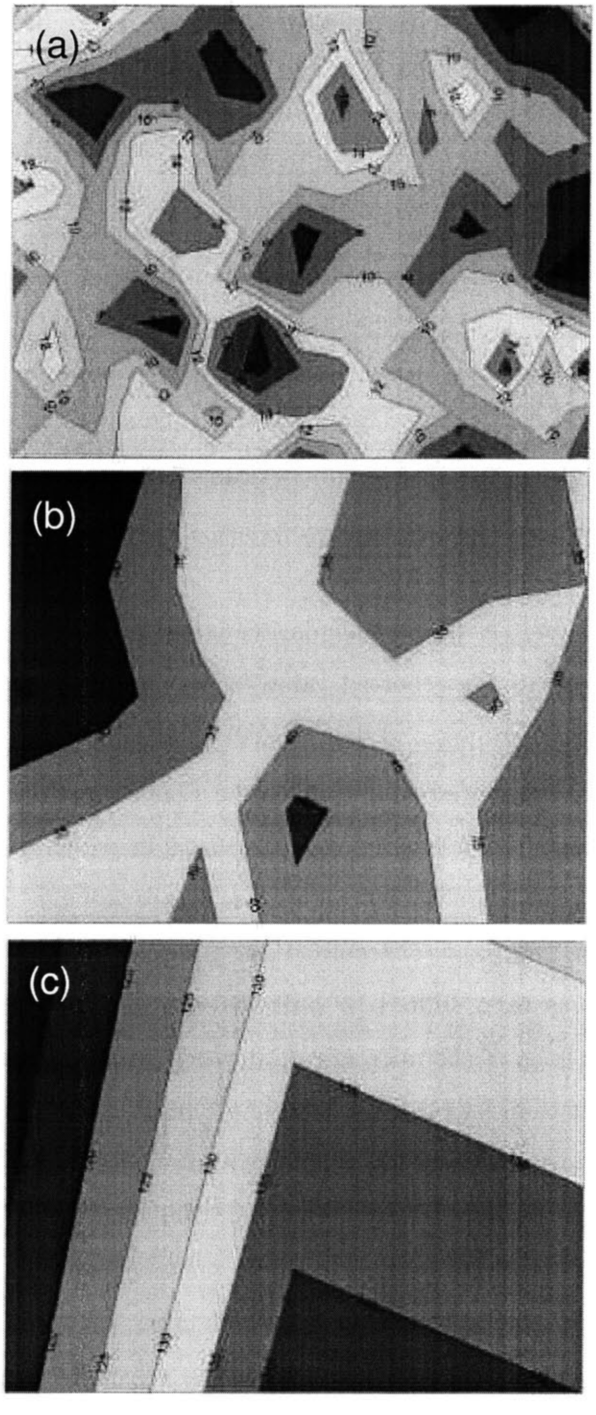

Figure 2-12: Contour plots of particle counts in the core of a 5% by weight sample created using three scan boxes with areas: a) $4\mu m^2$, b) $16\mu m^2$, c) $64\mu m^2$

	Scan box area (µm^2)		
	4	16	64
Average	9.88	34.86	128.67
Standard deviation	3.37	5.35	12.60

Table 2.2: Mean and standard deviation of particle count for various scan box sizes

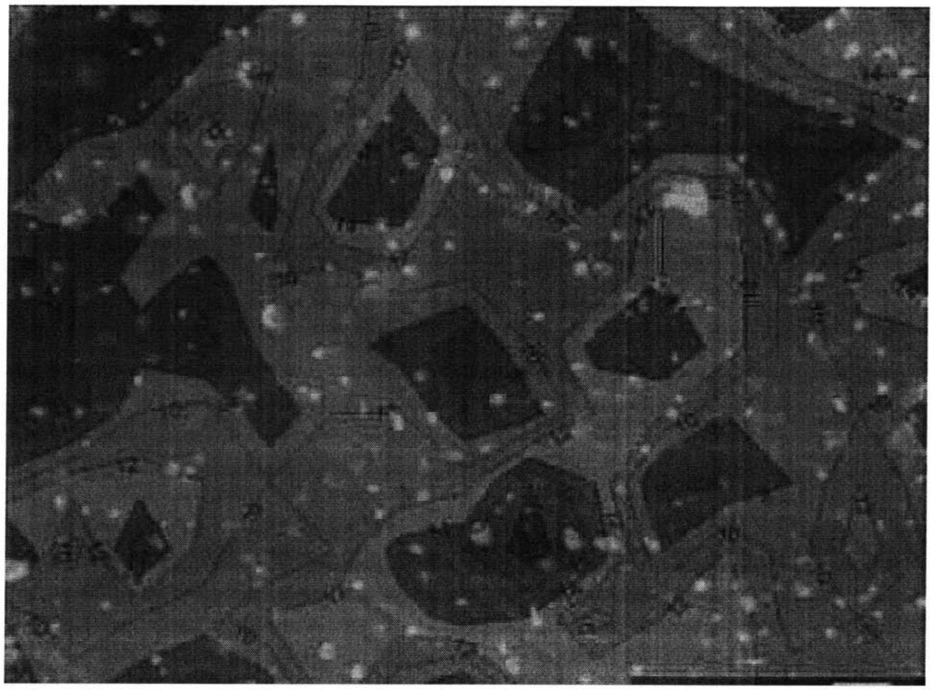

Figure 2-13: Superposition of the small-box particle count contour on the actual micrograph

As expected, as the size of the box increased, the contour plots of the particle count, which are shown in Figure 2-12, become smoother, with less variation. Table 2.2 summarizes the mean and standard deviation of the particle count for each scan box size. Even when the smallest box size was used, the standard deviation was less than 3.4 particles and the average was 10 particles. This data suggests that no significant clustering occurred during processing, which is consistent with the empirical observation made earlier. Superposition of the small-box contour plot on the actual micrograph further supports the agreement between the qualitative observations and the results of the data analysis, as shown in Figure 2-13.

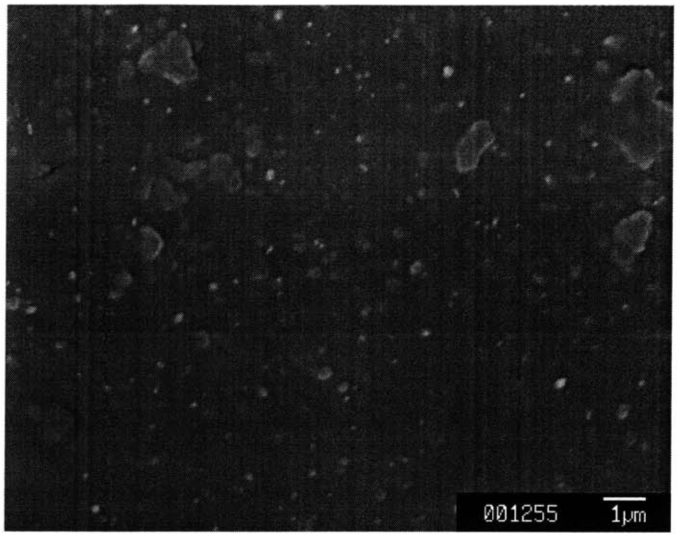

Figure 2-14: Micrograph of the edge region of a 5% by weight, microtomed and polished sample of multi-wall nanotube-PMMA composite

	Edge	Core
Total particle count	348	374
Average particle size (µm^2)	0.019	0.017
Particle area fraction	3.4%	3.4%

Table 2.3: Total particle count, average particle size and area fraction results obtained from the edge and core micrographs

A similar analysis was conducted on a micrograph of the same sample (shown in Figure 2-14) taken inside the edge region, 0.04 mm from the edge. The micrograph was thresholded, converted into a binary image and analyzed in terms of the particle size, overall particle count and area fraction. Table 2.3 summarizes the data and compares them with the data obtained from the core micrograph. The results are in excellent agreement for all three metrics and suggest an identical concentration of nanotubes at the edge and in the core.

The edge micrograph was also scanned with the $16\mu m^2$ area scan box in order to locate any potential nanotube clusters. The resulting contour plot, shown in

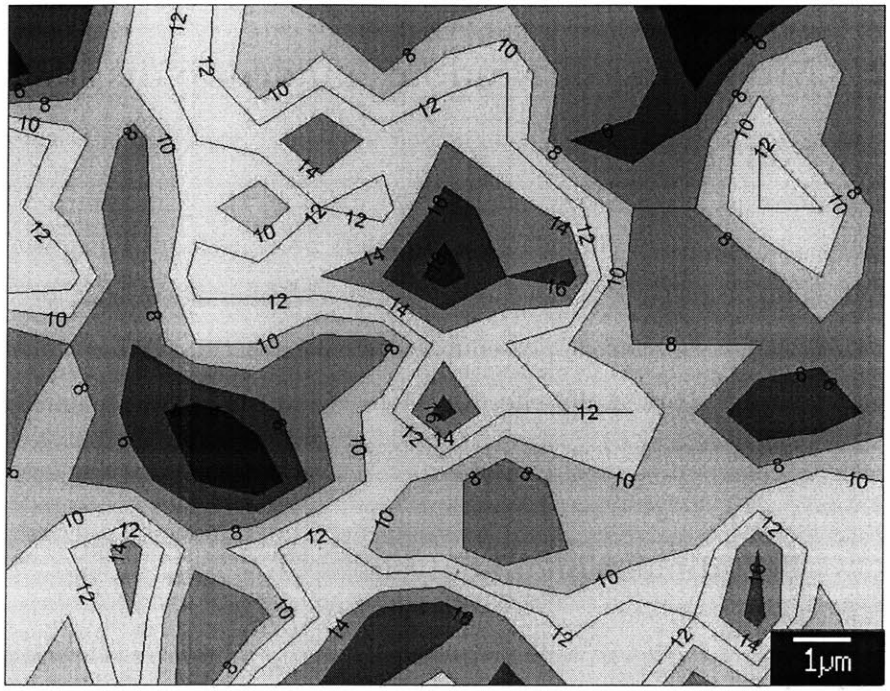

Figure 2-15: Contour plot of the particle count in the edge of a 5% by weight sample created using a $16\mu m^2$ area scan box

Figure 2-15, suggests that there is no significant variation in the degree of clustering between the core and the edge. Indeed, this observation is verified by the particle count data extracted from the micrograph. The average is 9.8 particles and the standard deviation is 3.6 counts, both of which match the values reported for the core micrograph for the $16\mu m^2$ area scan box (9.9 and 3.4 particles, respectively). Therefore, the appearance of bright rings in the micrograph can likely be attributed to poor grounding.

2.2 Modelling of random nanotube dispersion in a matrix

Although the experimental portion of this study provided valuable information about alignment and dispersion, it was constrained by a number of factors, most of which are related to the image analysis procedures used to extract data from the micrographs. Such limitations sparked the effort to model the distribution of nanotubes in the polymer and perform a more detailed analysis.

2.2.1 Two-dimensional analysis

The initial models were two-dimensional, as shown in Figure 2-16, and were implemented with the use of a representative volume element (RVE). In this case, a binary matrix was created to map a two-dimensional composite space. A "0" corresponded to a node occupied by matrix material and, conversely, a "1" represented a node occupied by a nanotube. The location of each nanotube was determined using a random number generator based on a uniform distribution. Each node was assigned a finite *effective unit volume*, which enabled the definition of an effective volume for the matrix and restricted the assignment of each node to a maximum of one nanotube. The length and diameter of the nanotube were hard-coded for the 2-D study at a fixed aspect ratio of 250. Necessary inputs for the models were either the number of nanotubes or the nanotube area and volume fraction, for the 2-D and 3-D cases

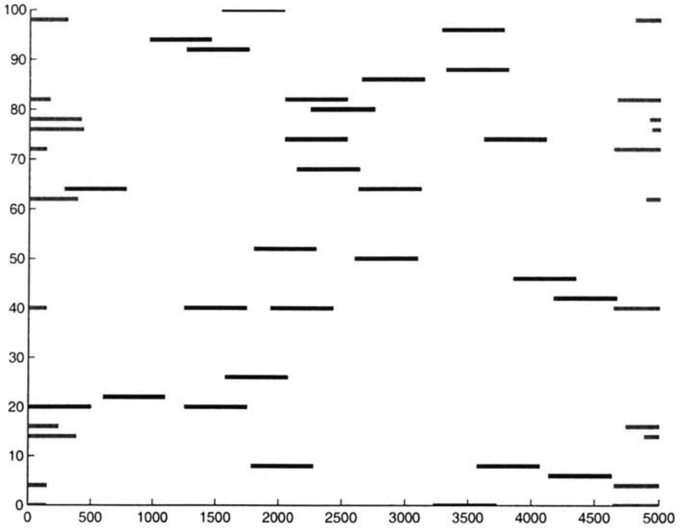

Figure 2-16: 2-D model of random, 15% by area nanotube dispersion

accordingly. In Figure 2-16 for example, nanotube area fraction was 15%. Moreover, periodic boundary conditions ensured geometric compatibility for the modelled volume in both directions. In the longitudinal direction (horizontal in the figure), nanotubes that were at or close to the boundary, shown in red in Figure 2-16, reentered into the opposite side. Similarly, nanotubes occupying nodes at one of the lateral boundaries (top or bottom edge in the figure) are assumed to also occupy the corresponding nodes on the opposite boundary, thus preventing the occupation of the same point in space by two nanotubes.

Such 2-D models offered valuable information about the lateral spacings between nanotubes. Figure 2-17 shows the distribution of spacings for the 2-D model shown in Figure 2-16. The first graph shows the number of nanotube nodes (y-axis) that have a nearest laterally neighboring nanotube node a certain distance away (x-axis), measured in matrix nodes. The second graph contains the same data, only in this case the number of occurrences (y-axis) has been divided by the nanotube length, thus registering the number of occurrences as number of effective or equivalent nanotubes. The shape of the histograms resembles a normal distribution in lateral spacings, centered around 0, which is a natural consequence of the randomization routine, based on a uniform distribution. Furthermore, due to the uniform distribution on which

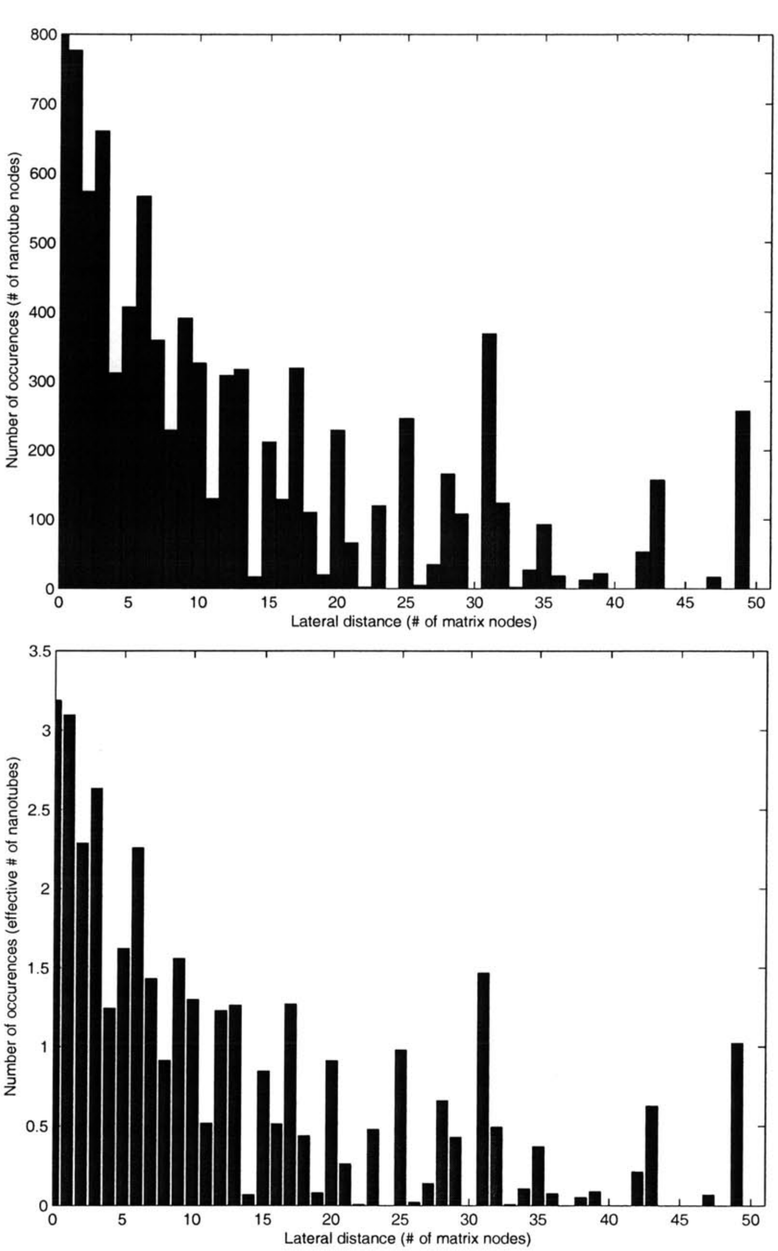

Figure 2-17: Lateral spacing histograms for a 15% by area nanotube 2-D model

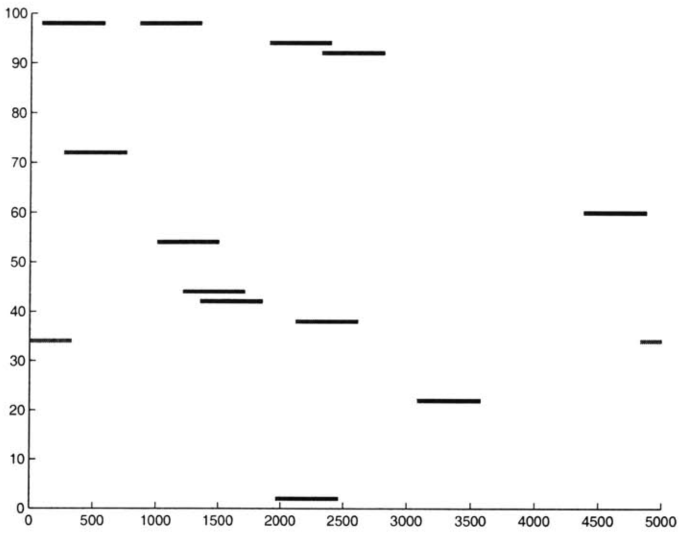

Figure 2-18: 2-D model of random, 5% by area nanotube dispersion

the random number generator was based, only minimal clustering was observed for the filler loads considered.

For comparison purposes, a similar model was created containing 5% by area nanotube (Figure 2-18). Both the standard deviation and the mean of the spacings tend to increase as the nanotube area fraction decreases, as shown in Figure 2-19. As fewer nanotubes are dispersed in the matrix, they are less densely packed, which raises the average spacings, but they also have a greater range of possible nodes where they can be located, which results in an increase in the scatter of the spacings data.

2.2.2 Three-dimensional analysis

The same concepts were extended into a three-dimensional model, such as the models depicted in Figures 2-20 and 2-21, which better resemble an actual composite with randomly dispersed nanotubes that the equivalent 2-D models. The 2-D binary matrix was replaced by a 3-D binary array, created by the same random number generator as in the 2-D case. Similar periodic boundary conditions where applied in all three dimension and the necessary inputs were either the number of nanotubes or the nanotube volume fraction.

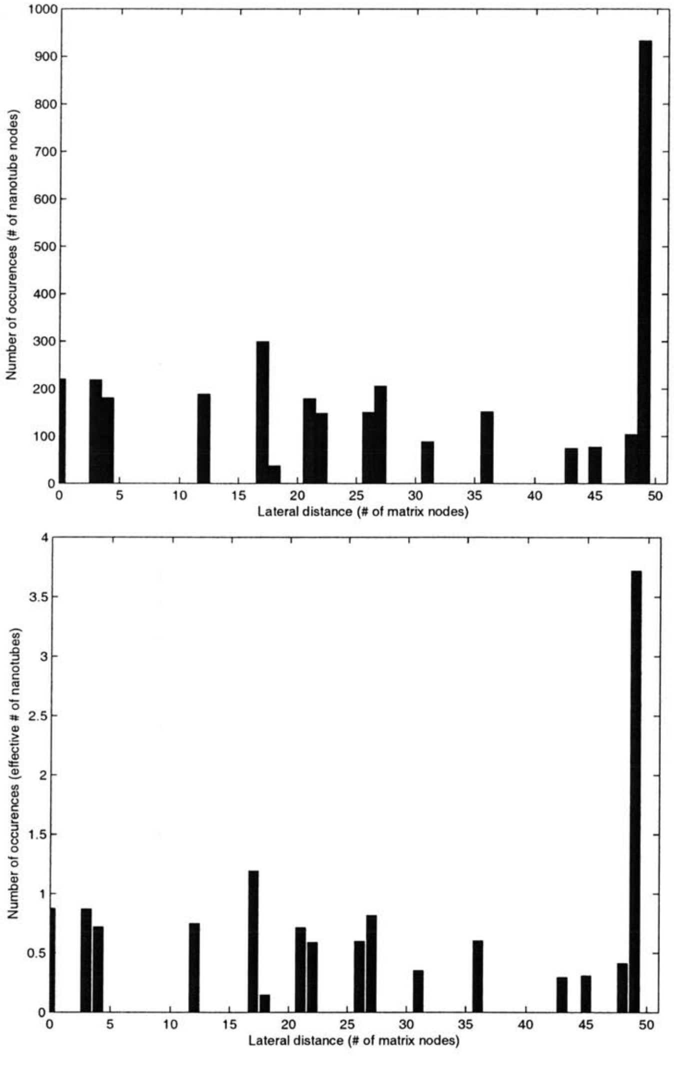

Figure 2-19: Lateral spacing histograms for a 5% by area nanotube 2-D model

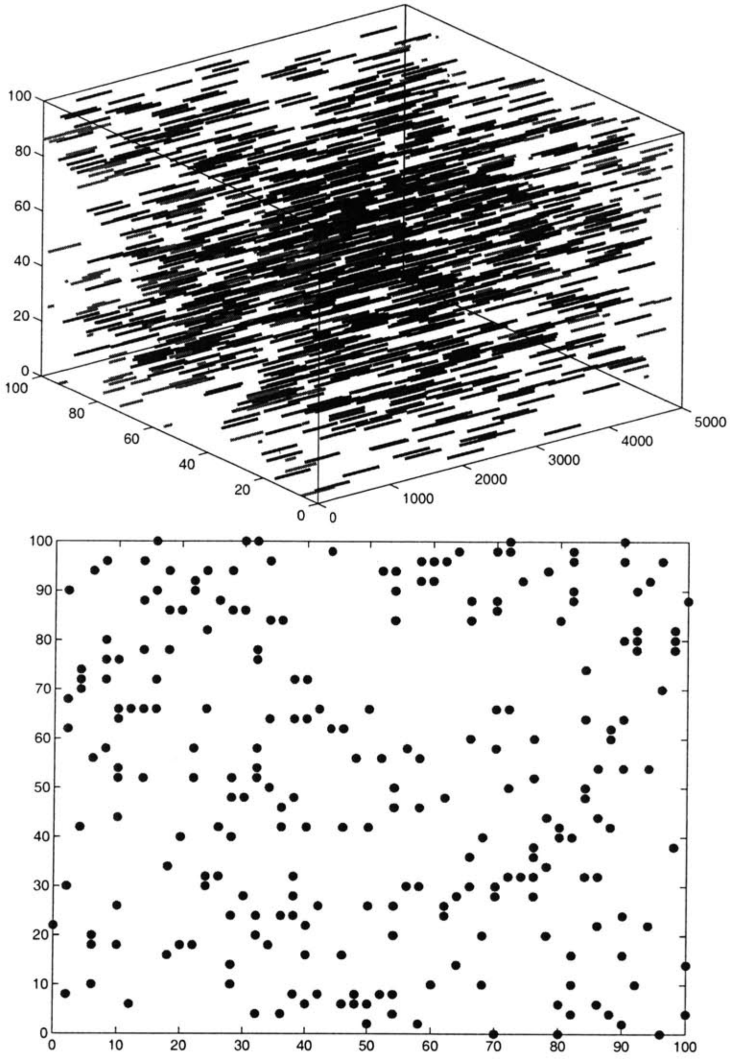

Figure 2-20: 3-D model of random, 15% by volume nanotube dispersion and axial cross section

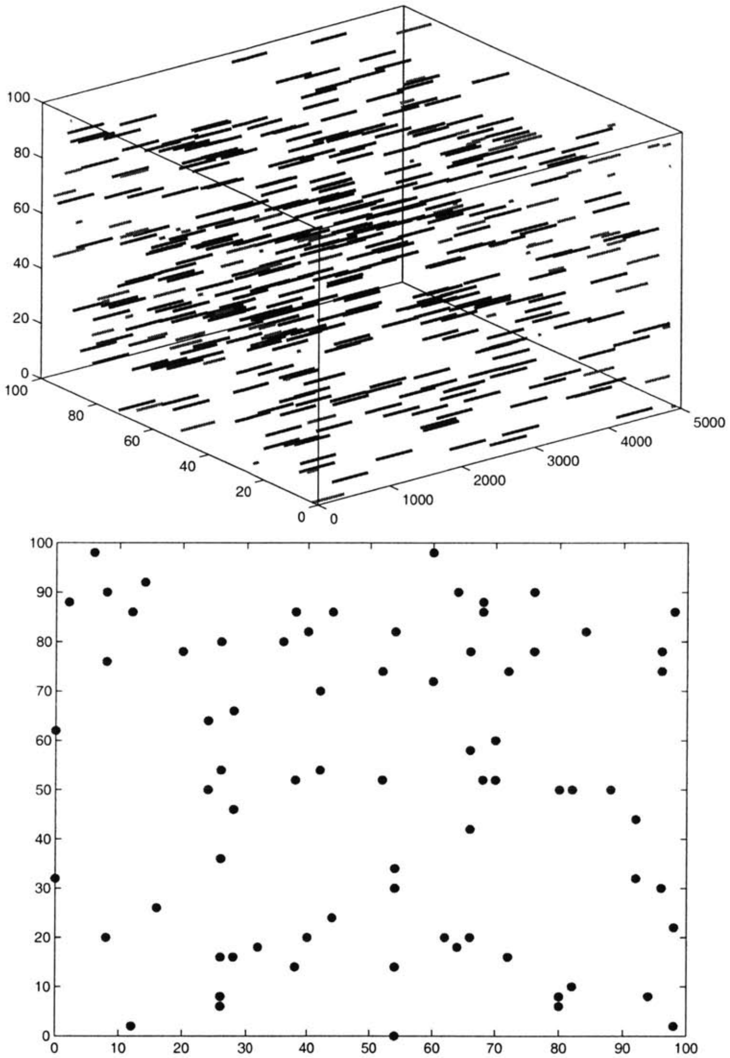

Figure 2-21: 3-D model of random, 5% by volume nanotube dispersion and axial cross section

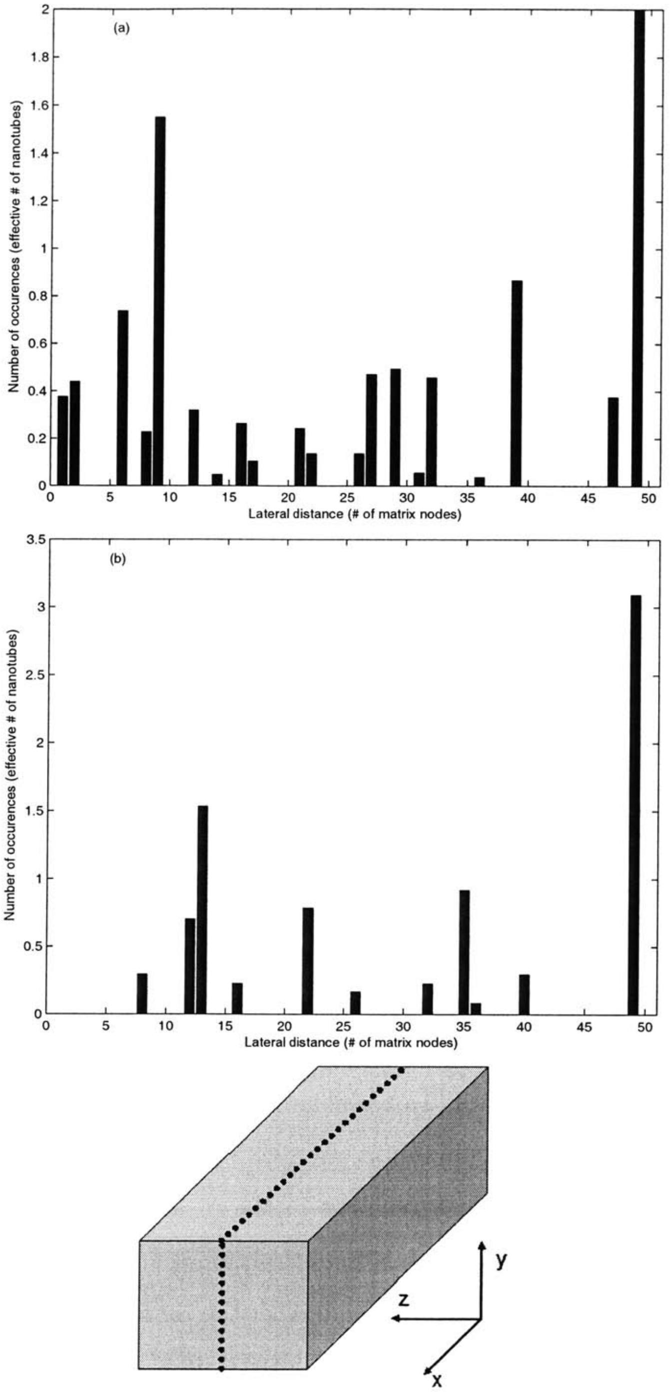

Figure 2-22: Lateral spacing histogram for a (a) 15% and (b) 5% by volume nanotube 3-D model

The same data about the lateral spacings was extracted for any cross-section parallel to the xy- and xz-planes shown in Figure 2-22. Furthermore, the ability to section the RVE across any plane parallel to the yz-plane and extract information about particle counts enabled the direct comparison between the experimental observations discussed previously and the models. Similar scan boxes as in the case of the micrographs were used to capture the number of particles, visualize the results through contour plots and identify any clusters. The smallest scan box used for the analysis of the micrographs was $4\mu m^2$ with the average nanotube having a cross-sectional area of $0.017\mu m^2$ which yield a ratio of 235. Due to the hard-coded dimensions of the model and the constraint of 50% overlap, only a finite set of box sizes could be used, namely 4-, 16-, 100-, and 400-node boxes. The volume fraction-box size combination that yielded the best results, for the purpose of comparison with the experimental results, was 30% and 100 nodes accordingly.

2.3 Comparison between experimental and theoretical results

Figure 2-23 shows a sample contour obtained from the model. Since the randomization code is based on a uniform distribution, no nanotube clustering is expected to occur and indeed, none is observed. Comparison with Figure 2-12(a) suggests that the model closely matches the actual composite that was studied. More specifically, the average particle count was 10 particles for the model (9.8 particles for the actual sample) and the standard deviation was 3.1 particles for the model (3.4 particles for the sample). Besides the agreement in the mean particle count, which suggests good calibration of the modelled volume fraction-scan box combination, the agreement in the standard deviation, coupled with the de facto uniform dispersion in the model serves as further proof that the nanotubes in the actual composite strands are randomly and uniformly dispersed.

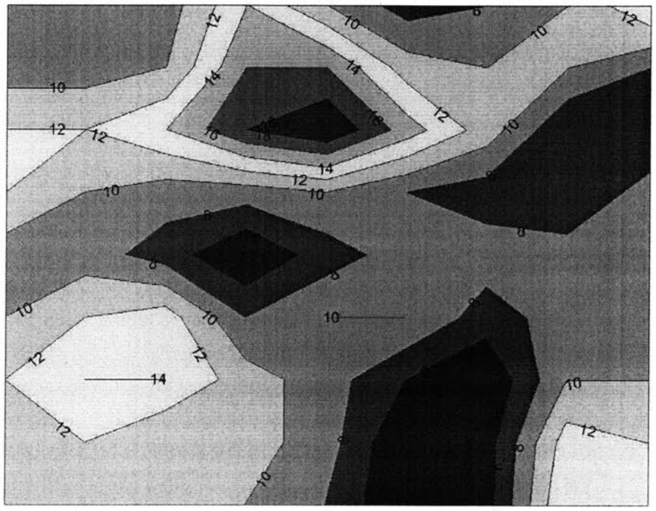

Figure 2-23: Contour plot of particle count in a modelled 30% by volume composite created using a 100-node scan box

Chapter 3

Finite element modelling of the mechanical behavior of a single-nanotube volume element

3.1 Motivation

The experimental investigation of filler dispersion in a nanotube-PMMA composite provided valuable tools and metrics that were used to develop and calibrate a realistic model of such a composite. This model provided significant flexibility in terms of the number of variables that could be adjusted to identify their effects, if any, on the macroscopic mechanical behavior of the composite. Such parameters include the nanotube aspect ratio, volume/weight fraction, degree of clustering, etc.

Finite element (FE) methods were employed to model the mechanical behavior of nanotube composites and study the effects of these and other parameters on the mechanical properties of the composites. Currently, FE modelling possesses a significant advantage over mechanical testing when used to investigate such issues. Experimental methods are handicapped by the limited ability to control parameters such as nanotube geometry, clustering and orientation as well as interfacial bonding between nanotubes and the matrix. As a result, robust understanding of the parameters that affect the mechanical properties of nanotube composites cannot be achieved solely by experimentation.

The primary goal of the FE simulations was to provide insight into the connection between the geometry-related and interface-related parameters on one hand and the mechanical behavior of nanotube composites on the other, by capturing the macroscopic stiffness of the modelled volume in each case and comparing it across different geometric and interfacial scenarios. The interface-related parameters include the load transfer mechanisms from the matrix to the nanotubes and, additionally, in the case of multi-wall nanotubes, from the outer to the inner walls. Such mechanisms may vary from weak van der Waals interactions, which only transfer normal loads, to shear transfer and the limiting case of perfect bonding. Other related issues of interest are the role of the nanotube walls and end caps and the debonding of nanotubes, which has been observed experimentally as well. Additionally, various nanotube and RVE geometric parameters were varied to study their effect on composite stiffness. Among these parameters are the RVE and nanotube aspect ratio, the volume fraction, the number of walls per nanotube, bamboo configurations, nanotube dispersion and wall curvature, which yields an initial strain energy due to rolling of the graphene sheet. Finally, besides serving as a common metric among the various models, the stiffness obtained from FE analyses, which contained numerous simplifying assumptions, also represented an upper bound to the actual stiffness of nanotube composites, thus defining the design limits of such composites.

3.2 Finite element model description

3.2.1 Microstructural representation and boundary conditions

Initial efforts focused on simplifying the randomly distributed nature of the nanotube dispersion to one of a regularly distributed in the form of either a stacked or a staggered array, as shown in Figure 3-1. The regular arrays permit the construction of a

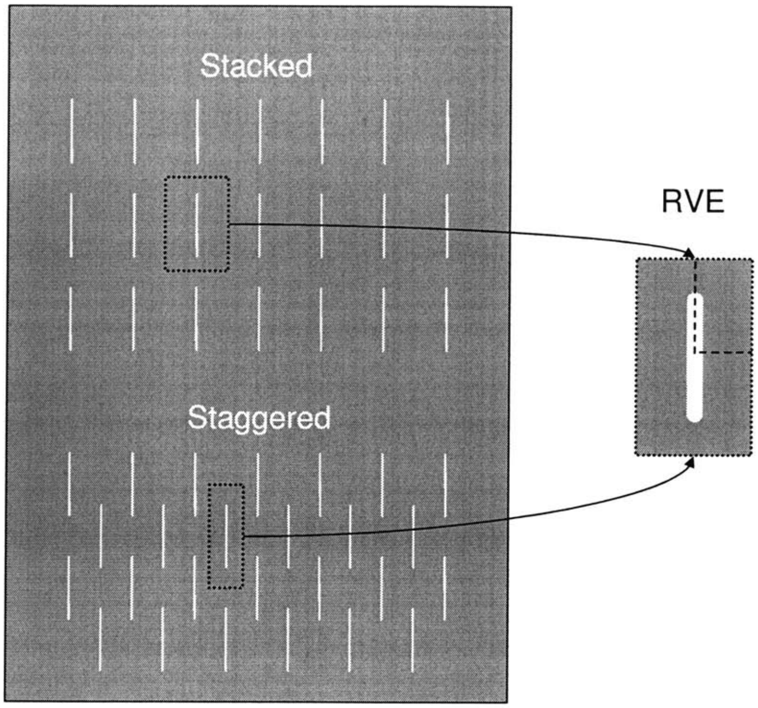

Figure 3-1: Schematic of stacked and staggered arrays of one-dimensional particles

unit cell RVE (one particle in a matrix, as shown in Figure 3-2)when used together with appropriate periodic boundary conditions. The nanotube along with the matrix constituted the two-phase composite representative volume element, *RVE*, a spatially periodic unit that deforms identically to its neighbors. For this reason, periodic boundary conditions are applied on each RVE to ensure deformation compatibility between adjacent RVEs (e.g. Socrate et al., 2000).

Uniaxial tensile loading is the load-displacement behavior of interest. Displacement was applied on the upper right node (node A) in Figure 3-6. The reaction force and displacement at that node in the x_2 direction was queried and used to extract macroscopic stress and strain data for the RVE. The nanotubes were perfectly aligned along the loading axis and they were assumed to be dispersed in either stacked or staggered arrays, as shown in Figure 3-1. Each array was implemented by the imposition of different periodic boundary conditions on the RVE for the stacked (Figure 3-3) and the staggered (Figure 3-4) cases that ensured deformation compatibility between

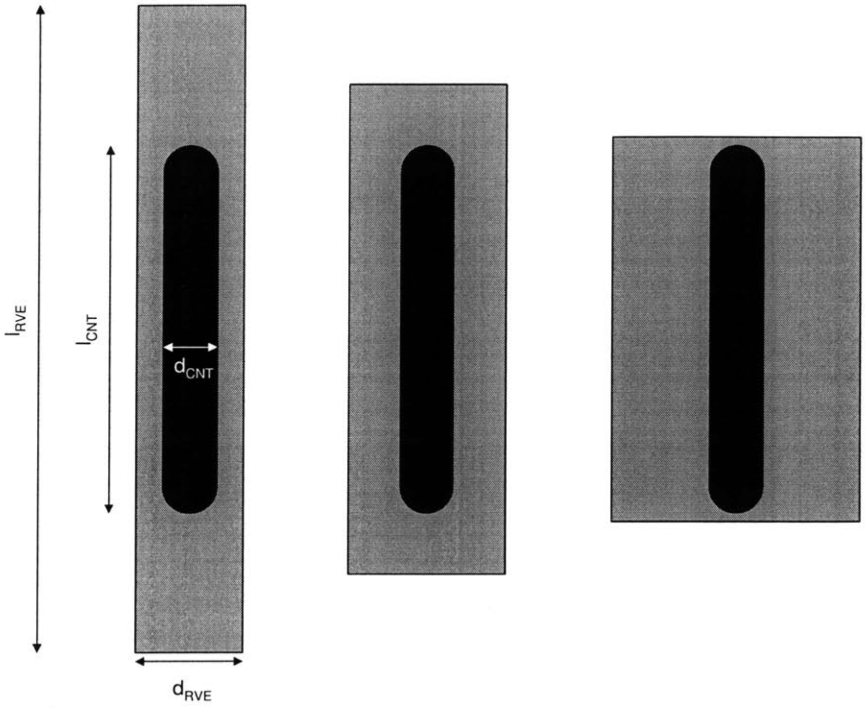

Figure 3-2: Schematic of a single nanotube embedded in a matrix n three different RVE aspect ratios

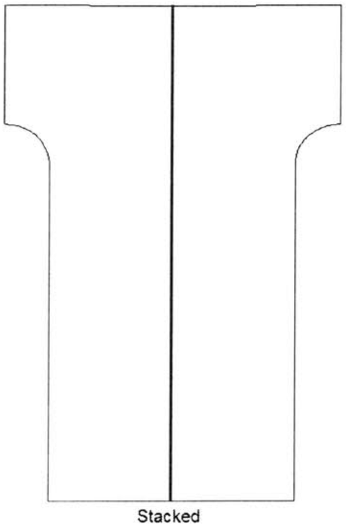

Figure 3-3: Spatial arrangement of laterally adjacent RVEs in the stacked case

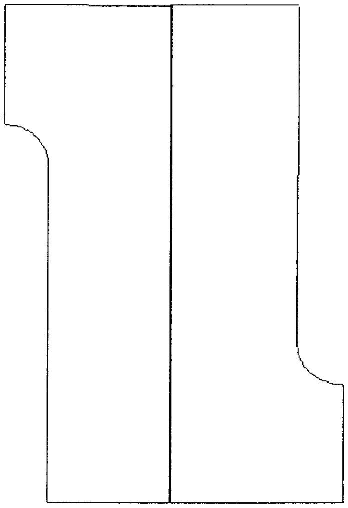

Figure 3-4: Spatial arrangement of laterally adjacent RVEs in the staggered case

adjacent RVEs. The stacked array is a rough idealization of actual nanotube dispersion that requires that the right and top edges remain straight and parallel to the principal axes of the model throughout the loading history. Thus, the constraints can be written as

$$u_A = u_{rightedge} \tag{3.1}$$

$$v_A = v_{topedge} \tag{3.2}$$

where the subscripts *right edge* and *top edge* represent all the nodes of the right edge and the top edge respectively, except for node A (Figure 3-5). Thus, by constraining the radial displacement of the side edge to that of node A and the axial displacement of the top edge to that of node A, Equations 3.1 and 3.2 enforces the requirement that both edges remain straight and parallel to the principal axes of the model. For the staggered case, the requirement on the top edge was the same as for the stacked array, i.e. it had to remain straight and parallel to the 1-direction as this is defined in Figure 3-7. However, both the radial and axial deformation of the nodes on the right edge are constrained by symmetry with respect to the deformation of the mid-node, C, shown in Figure 3-6. Mathematically, these requirements, in their linearized form,

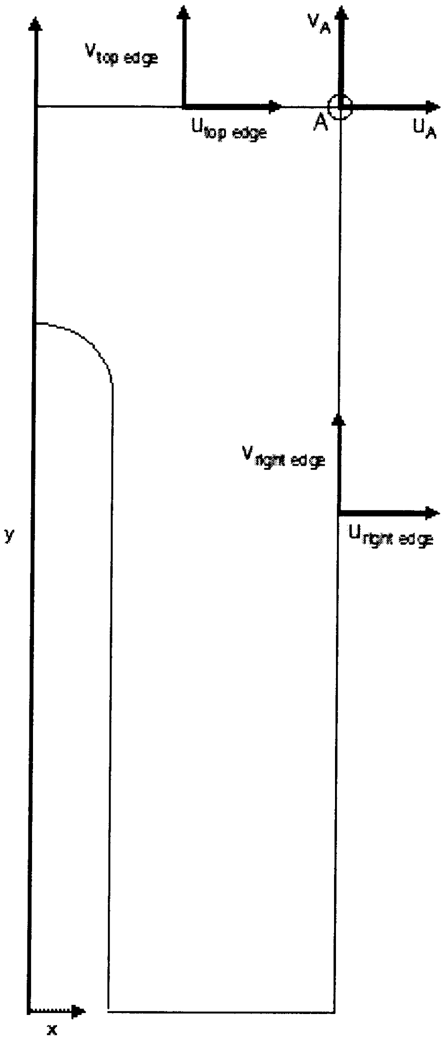

Figure 3-5: Schematic of the notation used for the stacked boundary constraints and equations

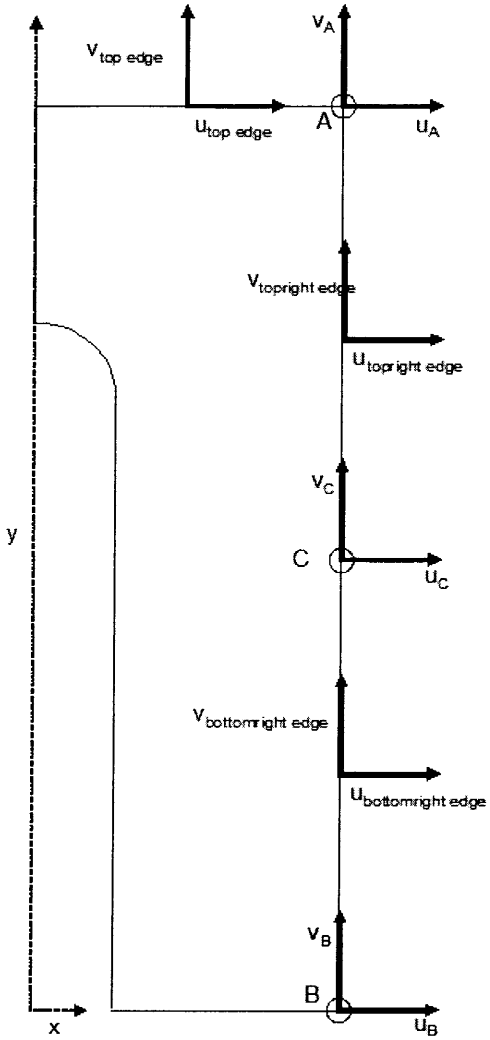

Figure 3-6: Schematic of the notation used for the staggered boundary constraints and equations

NT length (nm)	400
NT diameter (nm)	2.06
NT l/d	194
RVE length	409
RVE width	9
RVE l/w	45
Volume fraction	5%

Table 3.1: Geometric data for the model in Figure 3-7

are expressed as

$$u_{toprightedge} + u_{bottomrightedge} = 2u_C \tag{3.3}$$

$$v_{toprightedge} + v_{bottomrightedge} = 2v_c \tag{3.4}$$

$$v_A = v_{topedge} \tag{3.5}$$

The major drawback of the stacked array is that it's highly non-uniform; layers of pure matrix alternate with layers with large concentrations of nanotubes, resulting in a macroscopically in-homogeneous modelled composite. This non-uniformity limits the ability of the model to correctly capture the effects of particle interactions, which affect macroscopic mechanical behavior. As a result, the accuracy of the properties predicted by the stacked model is compromised, particularly at high load fractions. Nevertheless, modelling under the stacked assumption can provide valuable insight into the effects of geometry and interface properties.

Finally, in addition to periodic boundary conditions, constraints due to symmetry were imposed as well. More specifically, the nodes along the y-axis were constrained to zero radial displacement and zero rotation due to the axisymmetric nature of the model while the nodes along the x-axis were constrained to zero axial displacement and zero rotation due to symmetry with respect to the nanotube midplane (x-axis).

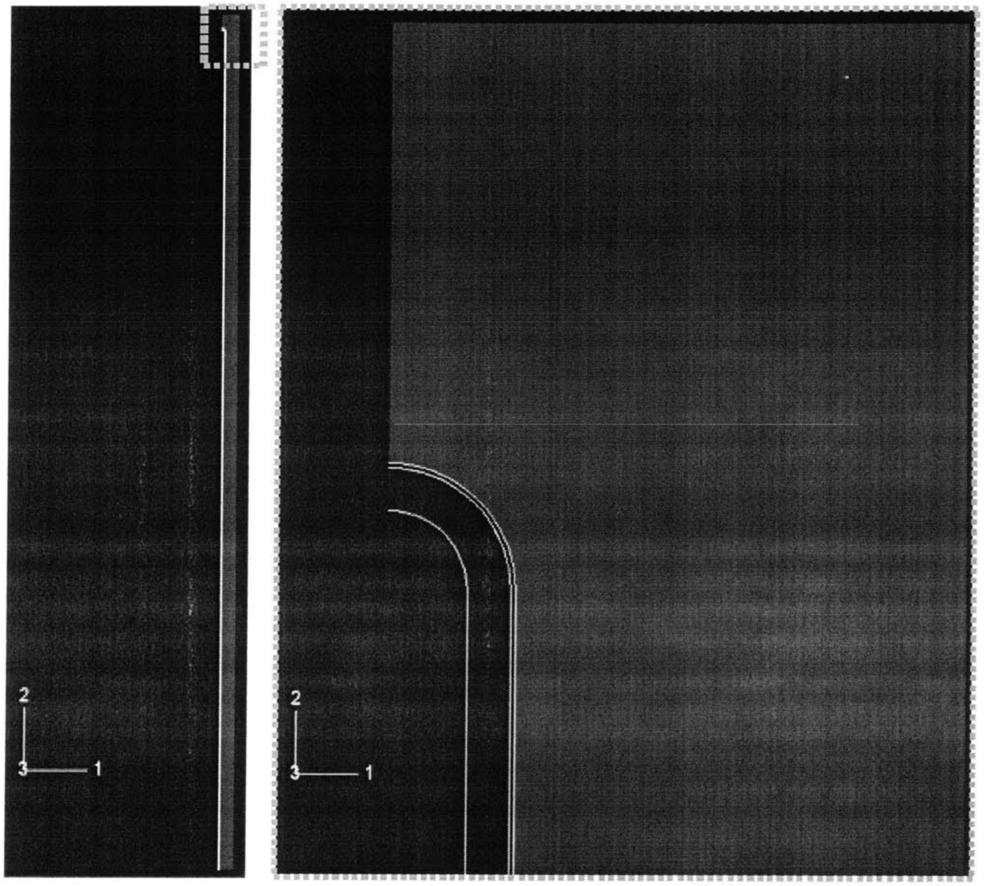

Figure 3-7: Schematic of a 2-wall nanotube composite RVE and detail of the end cap area

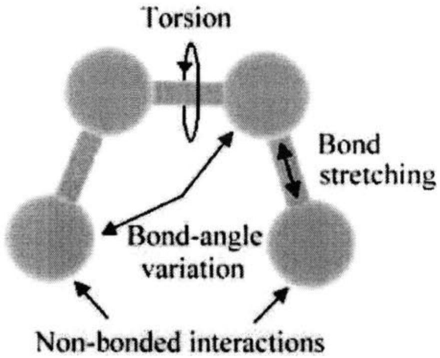

Figure 3-8: Geometric parameters affecting the stiffness of rolled graphene sheets (Odegard et al., 2001)

3.2.2 Material properties and assumptions

Matrix and nanotube properties

Due to the symmetry of the volume under consideration, an axisymmetric model of the upper half of the two-phase system was created, as shown in Figure 3-7. The matrix was assumed to be elastic-plastic with Young's modulus, $E = 3.1GPa$ and yield strength $\sigma_y = 120MPa$, corresponding to standard mechanical properties of PMMA. Some limited strain hardening was introduced to make the model computationally more stable than it would be under an elastic-perfectly plastic assumption. The effective properties of the nanotube walls were determined from the membrane stiffness. Both the bending and the stretching stiffness of the membrane can be related to the structure and properties of a graphene sheet. They originate from the resistance of carbon atoms in the graphene sheet to C-C bond stretching, in-plane C-C-C angle variation, dihedral angle torsion and out-of-plane angle bending, illustrated in Figure 3-8. Atomic-level models can provide values for both the stretching and bending stiffness of the membrane. Assuming a stretching stiffness of $59.36eV/atom$ and a bending stiffness of $2.886eV\mathring{A}^2/atom$, the resulting effective wall stiffness and effective wall thickness are $E_{wall} = 4.84TPa$ and $t_{wall} = 0.075nm$, respectively. Furthermore, the Poisson ratio of the nanotube wall, $\nu = 0.19$ was assumed to be identical to that of a graphene sheet (Pantano et al., 2004).

Various geometries were modelled. The nanotubes were always assumed to have hemispherical end caps but their aspect ratio, number of walls and volume/weight fraction as well as the aspect ratio of the RVE varied among models.

Interfacial properties

Matrix-nanotube interactions Two different states of the matrix-nanotube interface were investigated. In the first case, the nanotube was perfectly bonded to the matrix, both at the end cap and the wall. As a result of tying together their translational degrees of freedom, there was no relative displacement between the nodes of the nanotube (or, in the case of a multi-wall nanotube, the nodes of the external wall) and the corresponding interfacial nodes of the matrix. As it will be shown later, due to this simplifying assumption, under this scenario the predicted stiffness of the composite constituted an ideal upper limit rather than a realistic estimate.

In the second case, the nanotube was bonded with the matrix only through weak van der Waals interactions, which are capable of transferring normal load but no shear. This condition was implemented through the use of user-defined interaction elements that simulated van der Waals forces between the nanotube and the matrix. The adopted interfacial pressure expression was calculated by Zhao et al. (1989), it was based on the 12-6 Lennard-Jones potential for a carbon-carbon system and is given in Equation 3.6.

$$p(\alpha) = \frac{\Psi}{6}\left[\left(\frac{d_0}{\alpha}\right)^{10} - \left(\frac{d_0}{\alpha}\right)^{4}\right] \tag{3.6}$$

The pressure p is expressed as a function of the interlayer distance, α, $d_0 = 0.340nm$ is the equilibrium distance and $\Psi = 36.5GPa$. Figure 3-9 shows a plot of this expression, which yields negative pressure values for attractive interactions and positive values for repulsive interactions. Due to the rapid decay of pressure with distance, as noted from the figure, numerical instabilities often arised in the model, resulting in convergence issues. A number of methods were employed to address this problem without affecting the accuracy of the model. Some of the parameters that were tested were the master-slave selection, the step and increment size, the applied displacement, the arc-length method, etc. In the end, a combination of these parameters was used to resolve the

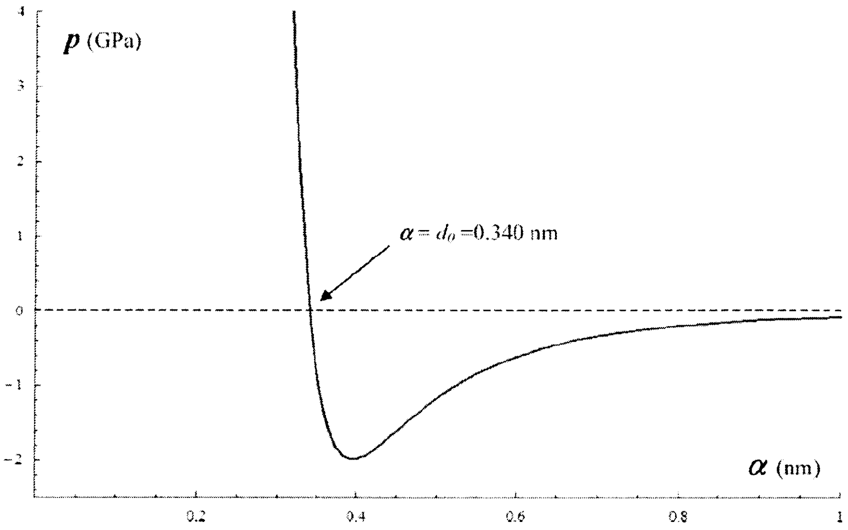

Figure 3-9: Interfacial pressure as a function of interlayer distance (Pantano et al., (2004)

convergence issue.

The interaction elements were assumed massless and were defined between a master and a slave surface. In order to model a single wall nanotube having van der Waals interactions with the matrix, a two-wall nanotube was defined with a 'null' external wall, i.e. a wall with zero stiffness. This layer was perfectly bonded to the matrix on one hand and weakly bonded to the inner wall through the interaction elements on the other. Therefore, the outer wall was serving as an intermediary between the inner wall and the matrix, without affecting however the mechanical behavior of the composite. This configuration eliminated the need to implement the interaction elements between dissimilar elements (continuum for the matrix and shell for the nanotube wall) and thus resulted in a more stable model.

Layer-to-layer interactions The same interaction elements were also used to simulate wall-to-wall interactions in multi-wall nanotubes. A similar two-wall nanotube was defined, with both layers having the actual mechanical properties of a nanotube wall in this case. Since there is virtually no shear load transfer from layer to layer in multi-wall nanotubes, it is reasonable to use the van der Waals interaction elements

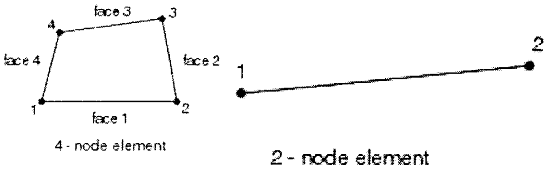

Figure 3-10: Bilinear continuum and linear shell axisymmetric elements used to mesh the matrix and the nanotubes accordingly

to simulate this condition. Indeed, there is overwhelming evidence that only weak van der Waals interactions exist between nanotube walls, with shear strength similar to that of high quality graphite ($\sim 0.48MPa$). Experimental evidence of the inner layers pulling out after the outer layer has fractured when loaded in tension further attests to the negligible load transfer through shear from the outer to the inner walls (Yu et al., 2000a).

3.2.3 Meshing

Four-node (bilinear) axisymmetric continuum elements were used for the matrix while two-node (linear) axisymmetric shell elements were used for the nanotubes (Figure 3-10). The mesh varied in density across the RVE, being very fine around the end cap and gradually coarsening away from it. Furthermore, mesh compatibility between the matrix and the nanotube was maintained along the interface in order to facilitate the implementation of the van der Waals interaction elements in that region. As a result, both the nanotube and the matrix at the interface were seeded with the same number of nodes, placed horizontally across each other in the wall region and radially across each other in the end cap region of the interface, as shown in Figure 3-11.

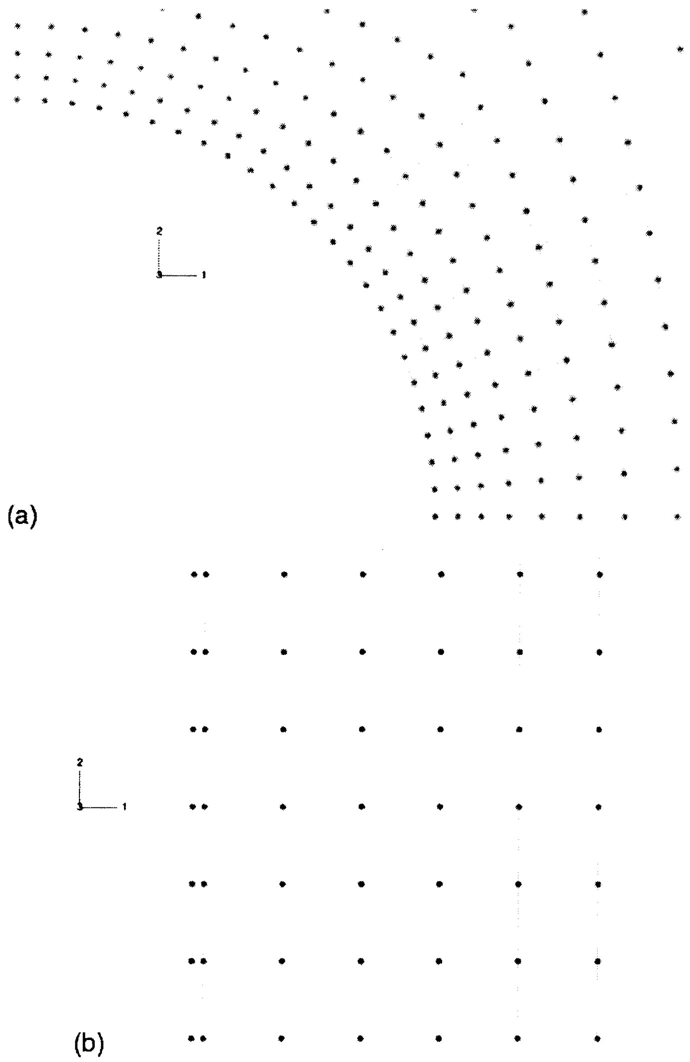

Figure 3-11: Mesh compatibility along the interface in the: (a) end cap region and (b) wall region

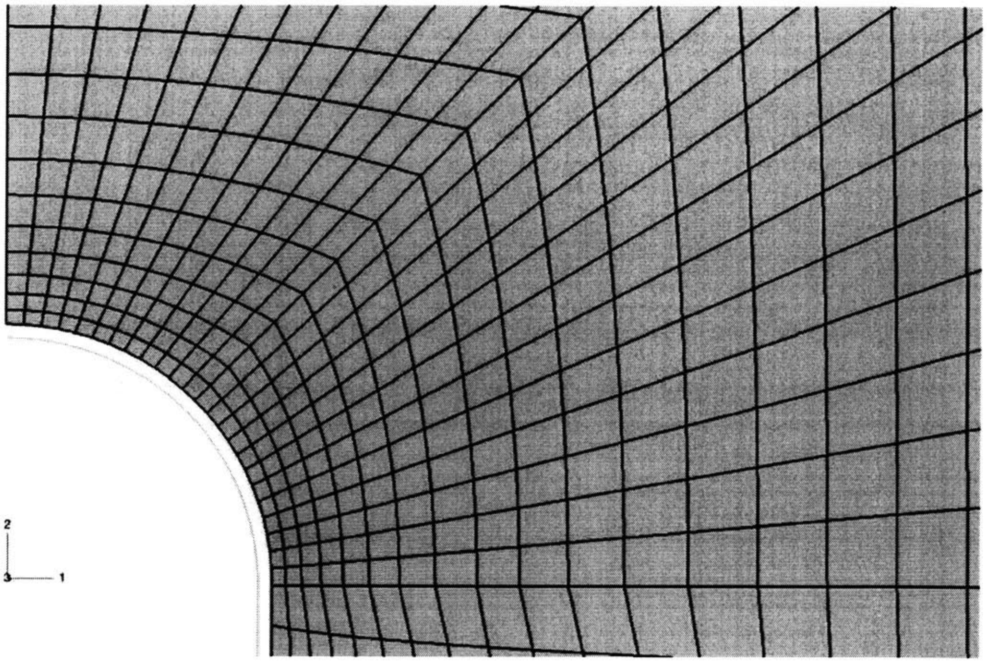

Figure 3-12: End cap area of a single nanotube, stacked RVE

3.3 Results and discussion

3.3.1 Modelling of a single wall nanotube, perfectly bonded to the matrix

Among the first and simplest models that were created was a single wall nanotube RVE with stacked periodic boundary conditions and perfect bonding between the nanotube and the matrix. Figure 3-12 shows a close-up of the end cap area. The nanotube is represented by a line and the matrix by the solid part. The apparent gap between the nanotube and the matrix is equivalent to half the effective thickness of the wall, $t_{wall} = 0.075nm$. The aspect ratios of the nanotube and RVE were ~ 440 and ~ 100 accordingly and the filler volume fraction was $\sim 5\%$.

Effect of periodic boundary conditions

Due to the high aspect ratio of the RVE, it is not practical to display it in its entirety in figures. For this reason, only the regions of interest such as the end cap area that

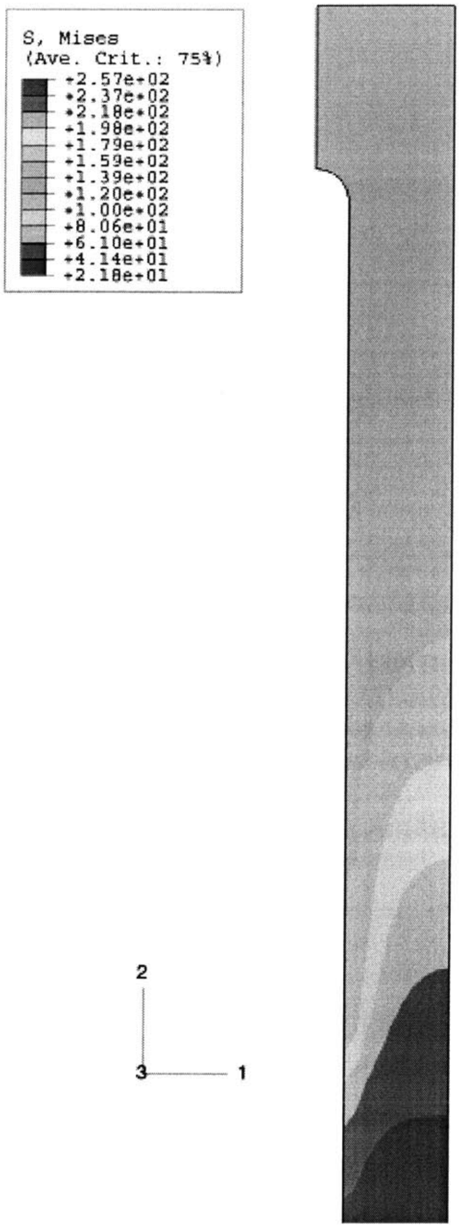

Figure 3-13: Contour plot of Mises equivalent stress at the end cap area of a single wall nanotube stacked RVE

are relevant to the discussion will be displayed in each figure. Figure 3-13 shows a contour plot of the Mises stress in the end cap region of the model. The grey areas indicate regions in which the Mises stress, $\bar{\sigma}$, is less than the yield stress, σ_y. Therefore, it can be concluded that significant yielding occurs around the end cap and along the interface close to the end cap even at low macroscopic axial strain, which in this case was 0.1%.

A number of factors contribute to this behavior. First, the nanotube is perfectly bonded to the matrix, which prevents any slippage at the interface and in addition, there is a significant difference in stiffness between the two, with the nanotube wall being approximately three orders of magnitude stiffer than the matrix. The coupling of these two factors leads to significant deformation in the matrix along the interface and severe stress and strain gradients radially from the interface to the right edge of the RVE. The principal logarithmic strain in the matrix around the end cap exceeds 6, as opposed to under 10^{-3} for the nanotube and under 10^{-1} for the matrix away from the interface.

Another major contributing factor to the pronounced yielding of the matrix is the boundary condition. As it was briefly discussed previously, the stacked assumption results in a highly non-uniform nanotube dispersion, with compliant layers of pure matrix alternating in the axial direction with stiff layers with high filler concentration. This non-uniformity results in concentrated matrix deformation occurring in a localized manner in the pure matrix layer of the RVE, thus producing yielding of the matrix in these regions, with the rest of the matrix experiencing little or no plasticity, as evidenced by Figure 3-13.

An identical model was created to study the behavior of the RVE under staggered periodic boundary conditions. Figure 3-14 shows a contour plot of the Mises stress in the matrix around the nanotube end cap. Both contours in Figures 3-13 and 3-14 have the same minimum and maximum limits in the plotted variable and as a result, have identical legends and color scales. Compared with the stacked model, the staggered model undergoes considerably less yielding, despite the fact that the macroscopic strain is the same (1%). Evidently, since all other model parameters are the same with

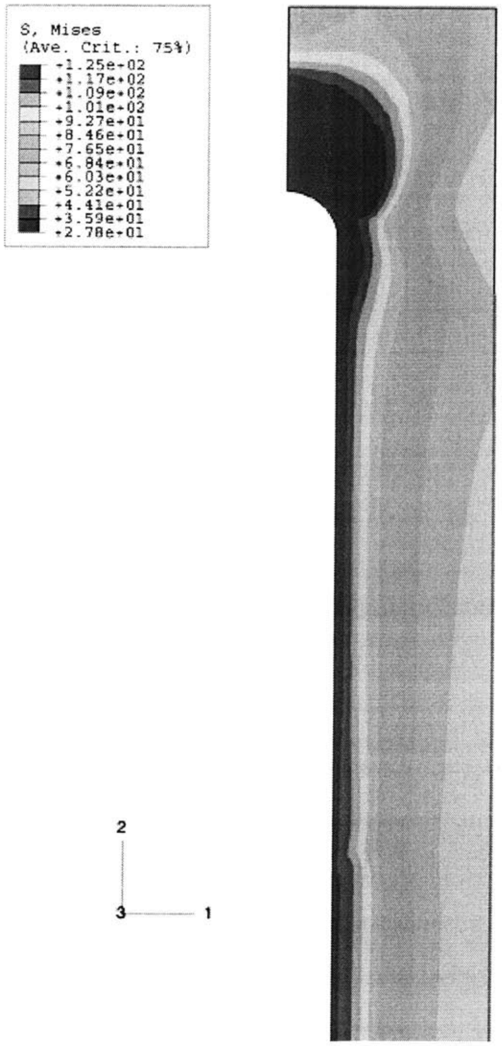

Figure 3-14: Contour plot of Mises equivalent stress at the end cap area of a single wall nanotube staggered RVE

the stacked model, the difference in responses has to be attributed to the boundary conditions. Indeed, the staggered array assumption is a better approximation to a random array, which has a constant particle distribution over large volumes of the composite. As opposed to the stacked array, in which weak layers of pure matrix are alternating with stiff layers with high particle concentration, the staggered array maintains a significantly smaller range of variation in nanotube concentration with axial position. As a result, the staggered RVE is subject to limited yielding as the matrix is shielded from straining by the stiffening effect of the nanotubes. Some plastic deformation does occur at the interface due to the perfect bonding of the stiff nanotube to the matrix. Nevertheless, the principal logarithmic strain around the end cap does not exceed 2.5, as opposed to 6 for the stacked model. Overall, the assumption of a staggered array results in a stiffer mechanical behavior of the RVE.

Predicted composite stiffness

The above findings regarding the differences in mechanical response between the stacked and the staggered model are also verified by the macroscopic stress-strain curves obtained for each model. In the stacked case, yielding is so widespread and severe that it affects the macroscopic response of the composite. On the other hand, matrix flow in the staggered case is more localized and the macroscopic response does not deviate from the elastic regime.

The applied periodic boundary conditions also affect the predicted stiffness of the composite. The staggered arrangement of nanotubes prevents or delays plastic collapse and consequently, staggered RVEs are stiffer than similar stacked RVEs. The predicted elastic moduli are $E_{stacked} = 47GPa$ and $E_{staggered} = 53GPa$ for the stacked and staggered models accordingly. Given that the matrix modulus is $E_{matrix} = 3.1GPa$ and the nanotube load factor is only 5% by volume, both predicted values are relatively high, compared with the most pronounced stiffening effects observed experimentally, which do not exceed a $\sim 90\%$ increase in elastic modulus over pure PMMA (Du et al., 2003). However, the predicted stiffness values should always be evaluated with consideration to the underlying model assumptions. In this case,

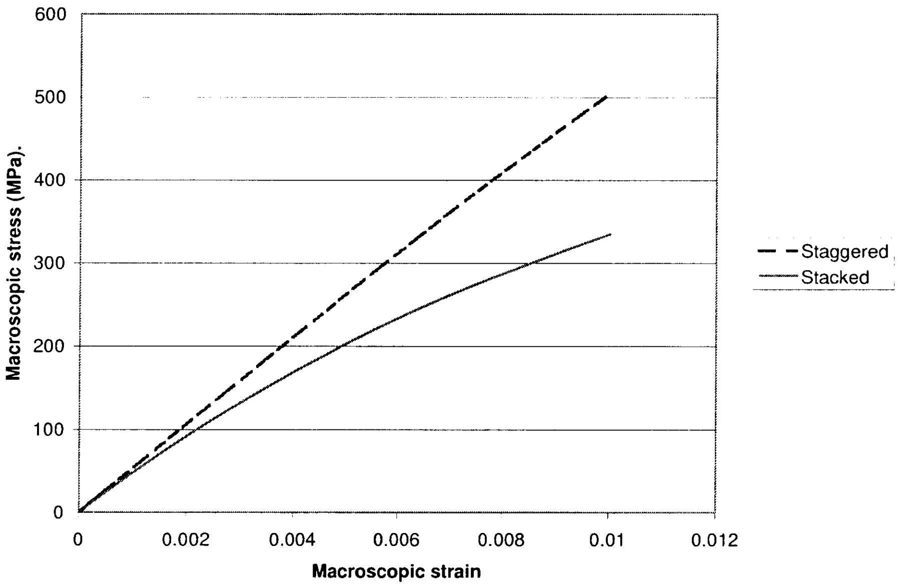

Figure 3-15: Macroscopic mechanical response of a stacked and a staggered RVE with a perfectly bonded single wall nanotube

Chirality	10,10	10,10	10,10
NT length (nm)	601.3751	601.3751	601.3751
NT diameter (nm)	1.3751	1.3751	1.3751
NT l/d	437	437	437
# of walls	1	1	1
RVE length (nm)	303	348	403
RVE radius (nm)	3	2.8	2.6
RVE l/d	101	124	155
Volume fraction	5.2%	5.2%	5.2%
Weight fraction	4.6%	4.6%	4.6%

Table 3.2: Geometric data for the models used in the RVE aspect ratio study

the perfect bond between the nanotube and the matrix is an idealization that drives the stiffness values high, resulting in a predicted upper limit rather than a realistic value for the modulus.

Effect of RVE aspect ratio

Another modelling assumption that affects the behavior of the RVE is its aspect ratio, l_{RVE}/d_{RVE} (Figure 3-2). The RVE aspect ratio determines the spatial distribution of matrix material around the nanotube. A high aspect ratio indicates a large spacing between nanotubes in the axial direction and a small spacing in the radial direction. The reverse is true for low aspect ratios.

Three models with different RVE aspect ratios were created in order to investigate the effects on mechanical behavior. All of the assumptions and model details that were discussed earlier are also applicable to these three models except for the RVE aspect ratios, which were 101, 124 and 155 for the low-, medium- and high-ratio RVEs accordingly. The RVEs were loaded in uniaxial tension and each model was tested both with stacked and staggered periodic boundary conditions

Figure 3-16 plots the macroscopic stress-strain response of all three models, under both stacked and staggered array assumptions, as well as the response of pure PMMA. Table 3.2 summarizes the geometric properties of each model. A number of conclusions can be extracted from the graph. First, compared to a stacked array of

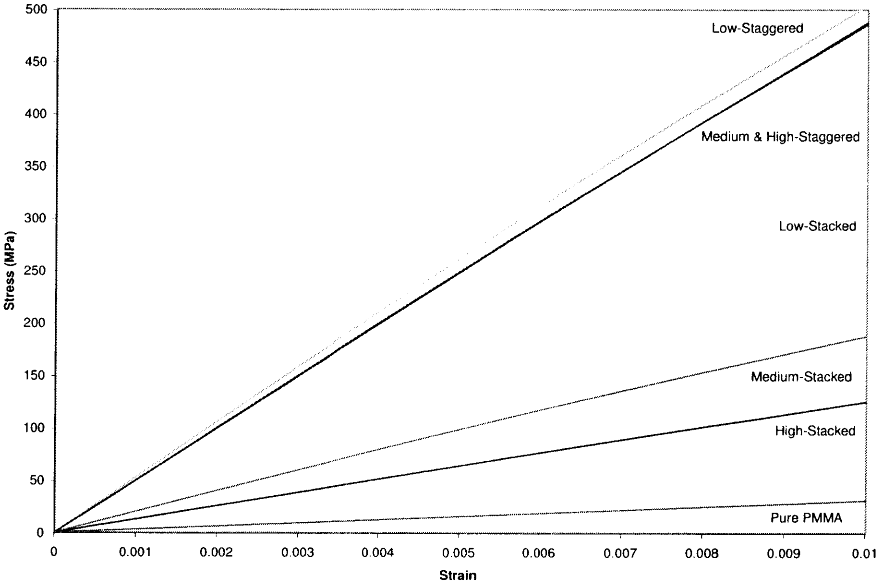

Figure 3-16: Macroscopic mechanical response of three RVEs with different aspect ratios, tested both with stacked and staggered periodic boundary conditions

NT length (nm)	400
NT diameter (nm)	2.06
NT l/d	194
RVE length	409
RVE width	9
RVE l/w	45
Volume fraction	5%

Table 3.3: Geometric data for the two-wall nanotube model

nanotubes, a staggered array of the same nanotubes in the same matrix has a greater stiffening effect, which is in agreement with the earlier results and discussion. Second, the stacked model is quite sensitive to modelling parameters, such as the RVE aspect ratio. Despite its limited magnitude, the variation in the RVE aspect ratio has a significant effect on the behavior of the stacked models. The stiffness of the RVE decreases as the aspect ratio increases, and ranges from $47GPa$ to $20GPa$ and $13GPa$ for the low-, medium- and high-aspect ratio RVEs respectively. As the aspect ratio increases, the weak layer of pure matrix material also increases in thickness, occupying a greater portion of the total RVE length and reducing the overall stiffness. Under different loading conditions, the effects on stiffness might have been different.

In contrast, the staggered model proved to be relatively immune to changes in the RVE aspect ratio. The behavior of the medium- and high-aspect ratio models was virtually identical, with stiffness around $50GPa$ whereas the low-aspect ratio model was somewhat stiffer than the rest at $53GPa$. Consequently, the robustness of staggered models with respect to model parameter variations makes them more suitable for studying the effects of physical and geometrical parameters on the composite as opposed to stacked models.

3.3.2 Modelling of a two-wall nanotube, perfectly bonded to the matrix

An internal wall was added to a single wall RVE to model a two-wall nanotube composite. The external wall was perfectly bonded to the matrix and the internal wall interacted with the external wall through the van der Waals interaction elements. All nanotubes were assumed to be of the armchair type and their diameters were consistently calculated from their assumed chirality, which naturally resulted in the appropriate wall-to-wall distance of $0.34nm$. In this model, the external nanotube was a (15,15) with a diameter of $2.06nm$ while the internal nanotube was a (10,10) with a diameter of $1.38nm$, a difference of $0.68nm$, or twice the interlayer distance. The geometric properties of the model are listed in Table 3.3.

The discussion of the results from the single wall nanotube models, such as the effects of periodic boundary conditions, pertains to multi-walls models as well and therefore, will not be repeated. The primary goals of this model were to investigate the occurrence of wall debonding within a multi-wall nanotube and evaluate the load that is transferred internally across the wall-to-wall interface.

Figure 3-17 shows snapshots of the end cap area of a two-wall nanotube taken at three instants of the simulation. The first image was taken at time, $t = 0$, at the equilibrium position when the interlayer pressure, $p = 0$ and the interlayer distance, $\delta = 0.34nm$ (Figure 3-18). As the RVE is loaded in tension, δ increases slowly while p increases rapidly to its peak absolute value at a macroscopic strain of $\sim 0.3\%$. Immediately after that point, the internal nanotube debonds from the external nanotube and snaps back. The pressure drops from its peak absolute value but remains non-zero due to diminishing weak interactions with the external wall. Similarly, debonding also manifests itself through a drop in the macroscopic stress-strain response of the RVE, shown in Figure 3-19. Note that beyond that point, the stress-strain curve is that of a single wall nanotube RVE.

The interlayer distance increases at the same rate as the displacement of the external wall, since the internal nanotube is virtually rigid. After the snap back, which occurs at very low strains, the nanotube behaves effectively as a single wall nanotube, since there is no load transferred internally. Obviously, this result relies heavily on the assumption that the external wall is perfectly bonded to the matrix. If that was not the case, then nanotube-matrix debonding could possibly occur before layer debonding, depending on the strength of each interface. Nevertheless, these

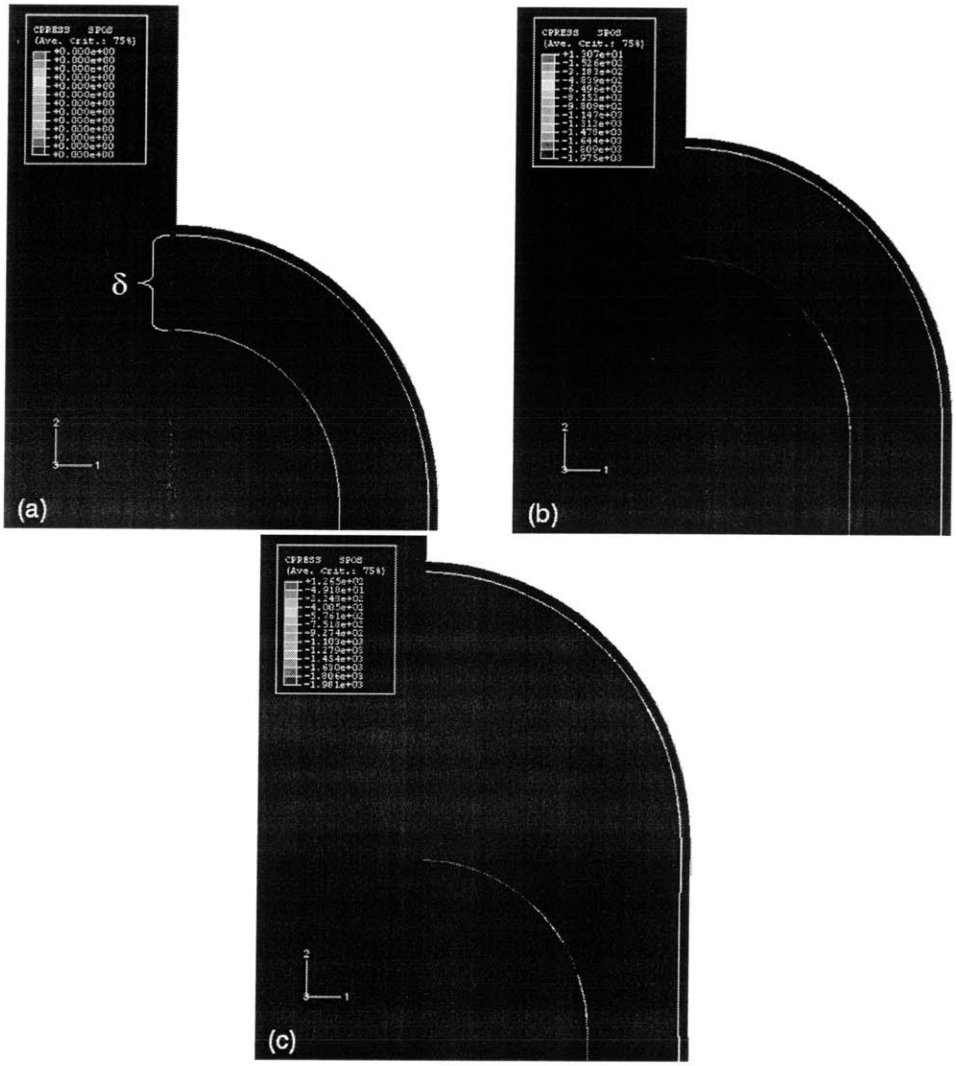

Figure 3-17: Consecutive snapshots of the end cap area of a two-wall nanotube during simulation of a composite RVE subjected to uniaxial tension

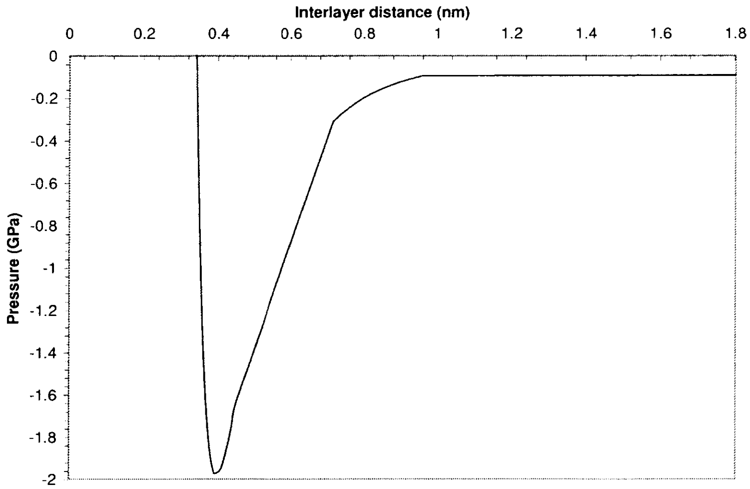

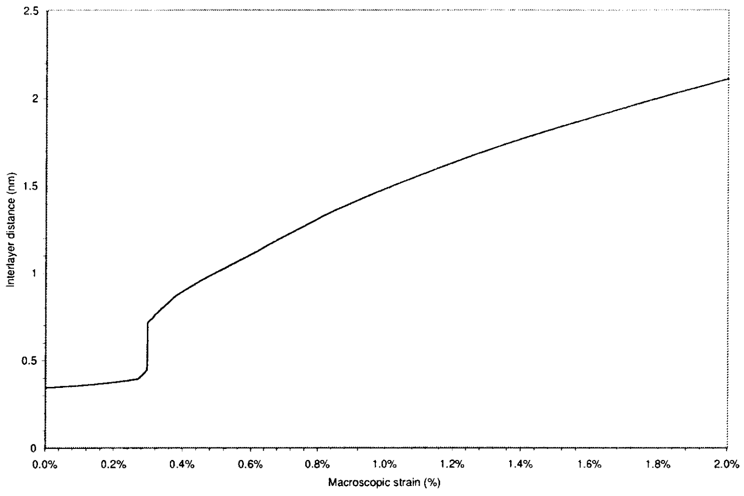

Figure 3-18: Interlayer pressure due to van der Waals forces as a function of distance and interlayer distance as a function of the macroscopic strain of the RVE

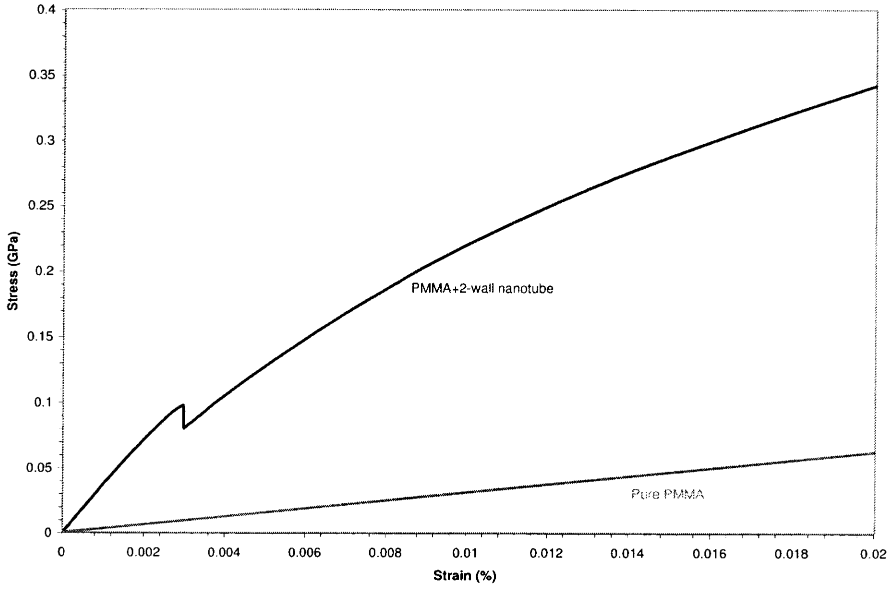

Figure 3-19: Stress strain response of the two-wall nanotube RVE

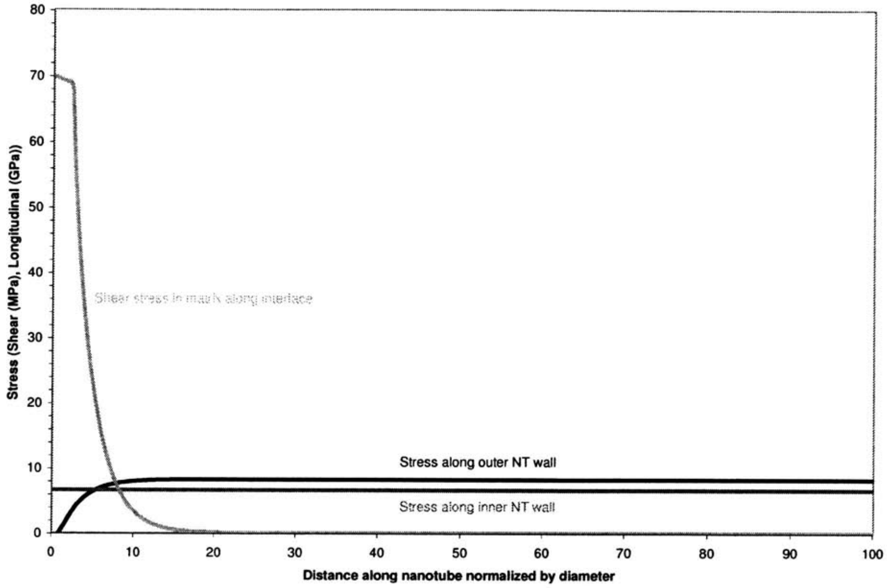

Figure 3-20: Stress distribution along the matrix-nanotube and nanotube-nanotube interfaces: shear stress distribution in the matrix and longitudinal stress distribution in the nanotubes. The x-axis corresponds to the distance along the interface from the point where the nanotube endcap connects to the nanotube wall

results provide insight into the functionality of the internal layers of a multi-wall nanotube.

Further proof of the limited load-carrying capacity of the internal nanotube under the current set of assumptions can be obtained by observing the stress distributions along the interfaces, plotted in Figure 3-20. All stresses refer to the stress values at the interfacial nodes along the walls of the nanotubes, ignoring any effects at the end caps, and were captured right before debonding occurred. Note that due to the symmetry of the nanotube, only half of the length is modelled and therefore, the maximum length value on the x-axis of the graph corresponds to the nanotube midpoint. The shear stress in the matrix and the longitudinal stress in the external nanotube follow a profile which is in agreement to the interfacial stress distributions predicted by the shear lag model (Figure 1-9). The matrix shear stress is maximum at the end cap and decays rapidly away from it, becoming effectively zero at the midpoint. Almost the exact reverse is true for the external nanotube. The anomaly in this case is that the longitudinal stress in the external nanotube is negative close to the end cap, due to the bending of the end cap, which results in compressive stresses in the transition area between the end cap and the wall. Beyond that point, it increases up to its peak value which maintains up to the midpoint. The internal nanotube, which is loaded in tension only through the end cap, has a constant longitudinal stress throughout its length which is $\sim$ 20% lower than the peak stress in the external wall. Furthermore, if more nanotubes were added internally, they would carry even lower loads. Therefore, due to the weak van der Waals interactions between the walls, the load carried internally decays rapidly, leaving the external wall to provide most of the stiffening effect in the composite.

Chapter 4

Sensitivity analysis of the predicted elastic modulus

In Chapter 3, the discussion focused on the assumptions associated with the single-particle model and their effect on the macroscopic mechanical behavior of the composite. Instead of modelling a composite with multiple nanotubes, a unit cell was defined that contained a single nanotube and that, through periodic boundary conditions, served as a representative volume element of a composite. Two types of periodic boundary conditions were investigated that represented two different approaches to simulating random nanotube distribution: stacked and staggered arrays. It was shown that stacked arrays are highly sensitive to the parameters of the model, such as the RVE aspect ratio, which have no physical significance in actual composites. On the other hand, staggered arrays proved to be relatively robust in that respect.

In order to evaluate and study the effects of physical and geometric parameters on the stiffness of the composite, external influences, such as the effects of modelling assumptions, had to be eliminated. For this reason, all sensitivity analyses are conducted using staggered periodic boundary conditions. Three factors are investigated, namely the nanotube aspect ratio, the volume/weight fraction and the number of walls. In each study, only one parameter varied while the rest remained constant. In all cases, the nanotube was perfectly aligned to the loading axis and the outermost wall was perfectly bonded to the matrix, which had the same properties as before.

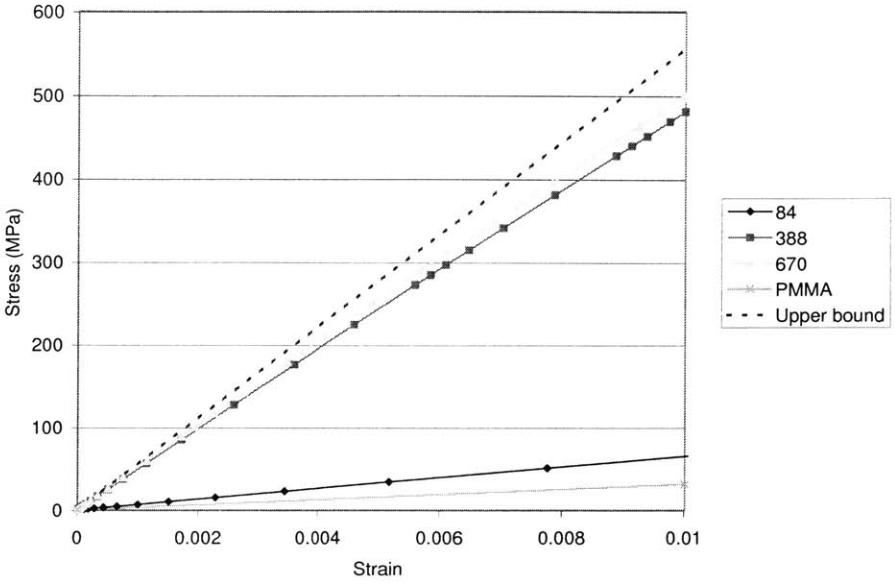

Figure 4-1: Macroscopic stress-strain response of three models with different nanotube aspect ratios and comparison with pure matrix material (PMMA) and the upper-bound solution

4.1 Effect of nanotube aspect ratio

Three different aspect ratios (84, 388 and 670) were observed for their effect on the stiffness of the composite. These values were selected since they were compatible with the particular meshing techniques that were used and facilitated the constraint that all other modelling parameters remain unchanged. The RVE aspect ratio and nanotube volume fraction, as well as the number of walls were held constant.

Figure 4-1 shows plots of the macroscopic responses for the three nanotube aspect ratios and Figure 4-2 shows the predicted stiffness as a function of the aspect ratio, normalized by the matrix elastic modulus. As the nanotube aspect ratio increases, so does the predicted stiffness, although the relationship is highly non-linear. The rate of increase is relatively high from the first ($l/d = 84$) to the second point while it drops

Chirality	10,10	10,10	10,10
NT length (nm)	115.38	533.38	921.38
NT diameter (nm)	1.3751	1.3751	1.3751
NT l/d	84	388	670
# of walls	1	1	1
NT density (g/cm^3)	2.15	2.15	2.15
NT wall stiffness (GPa)	4840	4840	4840
RVE length	240	400	480
RVE radius	1.5	2.5	3
RVE l/r	160	160	160
Matrix density (g/cm^3)	1.17	1.17	1.17
Matrix stiffness (GPa)	3.1	3.1	3.1
Volume fraction	5.03%	5.04%	5.04%
Weight fraction	4.44%	4.45%	4.45%

Table 4.1: Model data for nanotube aspect ratio analysis

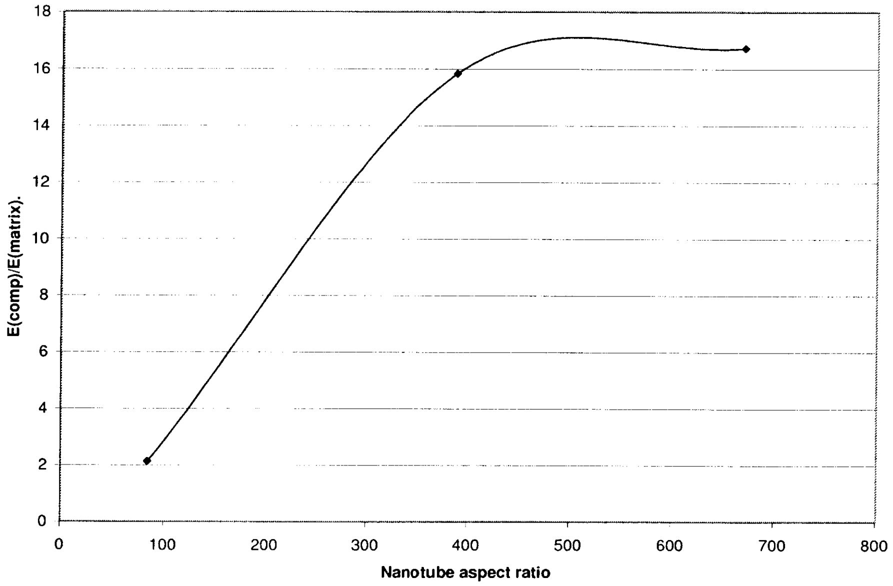

Figure 4-2: Normalized composite stiffness as a function of nanotube aspect ratio

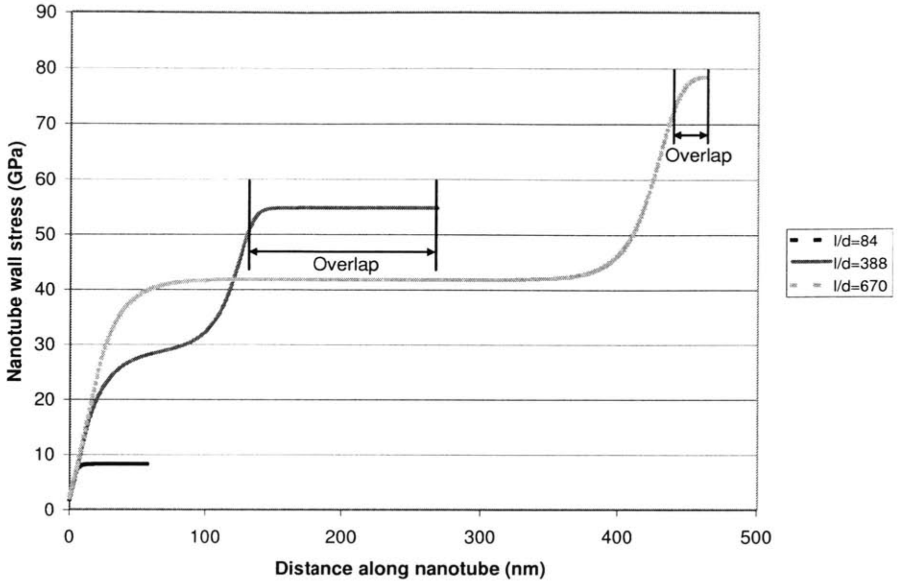

Figure 4-3: Tensile stress distribution along the length of the nanotube wall

significantly between the second and third points ($l/d = 388$ and 670 respectively).

There are two parameters that affect the results of this analysis and contribute to the variation in the predicted composite stiffness and the non-linear nature of this variation: the length of the nanotube and the length of the lateral neighboring nanotube overlap.

Load transfer in discontinuous-fiber composites loaded in uniaxial tension occurs primarily through shear load transfer from the matrix to the fiber, assuming the fiber is perfectly bonded to the matrix. Matrix shear is maximum at the nanotube ends and rapidly decreases away from them along the interface, while longitudinal stress in the nanotube wall increases and attains its peak value where matrix shear vanishes. Figure 4-3 shows the tensile stress distribution for the three models with different nanotube aspect ratios. In all three cases, tensile stress has non-zero values at the

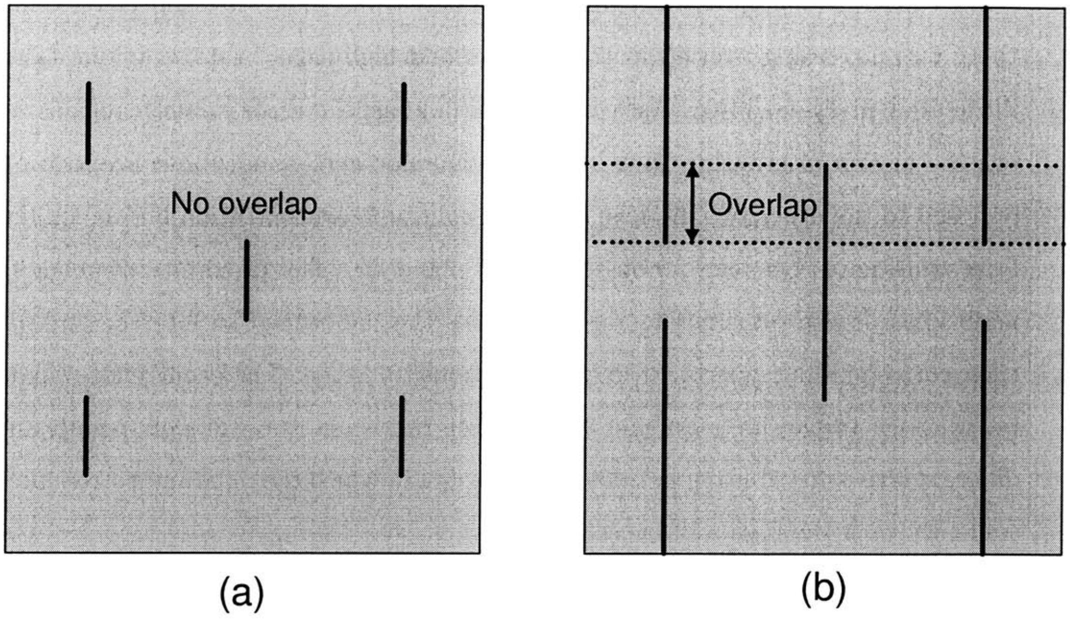

Figure 4-4: Two examples of staggered arrays: (a) Non-overlapping, low aspect ratio and (b) Overlapping, high aspect ratio nanotubes

nanotube end due to some limited load transfer through the end caps. As the length of the nanotube increases, so does the portion of the nanotube that caries the maximum stress/strain. As a result, the reinforcing effect of the nanotube on the uniaxially-loaded composite increases with increasing nanotube aspect ratio, approaching that of a continuous fiber in the limiting case. The change in composite stiffness is therefore attributed to the increased load-carrying nanotube length.

Figure 4-3 however highlights yet another difference among the three models. In the low aspect ratio model, the tensile stress in the walls increases away from the end caps and maintains its maximum value throughout the midpoint area. However, both of the other two models, immediately after the initial increase display an intermediate constant stress plateau before reaching the maximum value. As it was described earlier, the only geometric parameter that varied among the three models was the nanotube aspect ratio. The volume fraction as well as the RVE aspect ratio were held constant. In order to accommodate these constraints, the RVE increased in size both axially and laterally as the nanotube length increased. Consequently, while there was no overlap among laterally neighboring nanotubes in the low aspect ratio model, there was increasing overlap in the medium and high aspect ratio configurations, as illustrated in Figure 4-4. As a result, the low aspect ratio model contains layers of pure matrix alternating with layers of some non-zero nanotube concentration, as opposed to the other two models, in which nanotube concentration between adjacent layers alternates between a non-zero value x and $2x$. The proximity of neighboring nanotubes at the overlapping region enables the nanotubes to interact and allows their corresponding matrix strain perturbations to merge. The occurrence of particle interactions in the medium and high aspect ratio nanotube models results in the different stress distribution profiles in Figure 4-3, in which the maximum stress portion coincides with the region of overlap.

4.2 Effect of nanotube volume/weight fraction

Another parameter that was investigated is the nanotube volume/weight fraction and its effect on the behavior of the composite. Following the methods employed in the other sensitivity analyses, the nanotube and RVE aspect ratios were held constant as the nanotube volume fraction varied. This was achieved by maintaining constant dimensions for the nanotube throughout the study while the length and diameter of the RVE changed in proportion according to a fixed aspect ratio ($l_{RVE}/d_{RVE} = 50$).

4.2.1 Correspondence between nanotube volume and weight fraction

The overwhelming majority of experimental results on composite properties are reported with respect to the weight rather than the volume fraction of the nanotubes in the matrix. Therefore, it became necessary, for the purpose of consistency, to be able to convert from volume fraction, which was used to measure filler concentration in the models, to weight fraction, which is used in actuality. Due to the variation in the structure of nanotubes (variable number of walls, chirality, etc.), no widely-used

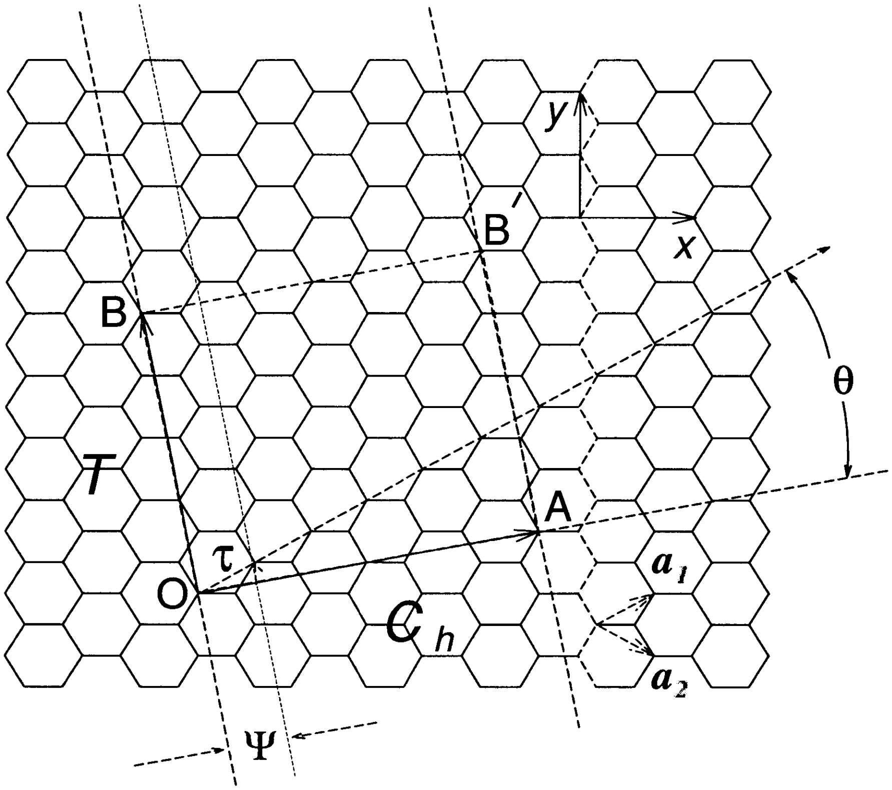

Figure 4-5: Schematic showing how a graphene layer is rolled into a nanotube (Dresselhaus et al., 2001b)

density values have been established in literature. For this reason, a MATLAB-based code was developed to estimate nanotube density, given the chirality of the external nanotube and the number of walls.

Nanotube chirality

Nanotubes can be perceived as single graphene layers, seamlessly rolled into concentric cylinders. In this case, their structure can be described conveniently in terms of 1-D unit cell, extending axially and defined by the vector $\overrightarrow{C_h}$ and $\overrightarrow{T}$ shown in Figure 4-5. The chiral vector, $\overrightarrow{C_h} = n\overrightarrow{a_1} + m\overrightarrow{a_2}$ connects two crystallographically equivalent sites on a graphene sheet and defines the circumference of the nanotube. In the (n, m) notation, when either n or m are 0, the chiral vector denotes a zigzag nanotube. When $n = m$, it denotes an armchair nanotube. The chiral angle θ is the angle between the zigzag direction ($\theta = 0$) and the chiral vector. When $\theta = 0^o$ and 30^o, the nanotube is *achiral* and the angles correspond to a zigzag and an armchair nanotube respectively; if $0^o < \theta < 30^o$, the nanotube is *chiral.* The intersection of the normal vector to $\overrightarrow{C_h}$, $\overrightarrow{OB}$ with the first lattice point determines the translation vector $\overrightarrow{T}$ which, together with the chiral vector, define the rectangular unit cell of the 1-D lattice illustrated in Figure 4-5.

The nanotube is formed by rolling the unit cell to superimpose the two ends of the vector $\overrightarrow{C_h}$ and forming a joint along the lines $\overrightarrow{OB}$ and $\overrightarrow{AB'}$, both of which are perpendicular to the chiral vector (Dresselhaus et al., 2001b). The nanotube diameter d_t is given by

$$d_t = \sqrt{3}a_{C-C}(m^2 + mn + n^2)^{1/2}/\pi = C_h/\pi \tag{4.1}$$

where C_h is the length of $\overrightarrow{C_h}$ and a_{C-C} is the C–C bond length ($1.42\mathring{A}$).The number of hexagons, N, per unit cell of an armchair nanotube is

$$N = 2(m^2 + n^2 + nm)/3n \tag{4.2}$$

Each hexagon in the lattice contains two carbon atoms. Finally, the length of the translational vector, $\overrightarrow{T}$ is $T = a$, where $a = 2.49\mathring{A}$ is the length of the unit vector (Dresselhaus et al., 2001b). Therefore, both the volume of the nanotube and the number of carbon atoms contained in it can be calculated from its chirality.

Calculation of density as a function of chirality and number of walls

For the purpose of calculating the mass per unit cell, the mass of a ^{12}C atom was assumed to be $1.993 \times 10^{-23} g$. Figure 4-6 shows a plot of the density of a nanotube as a function of the number of walls, with an external wall of chirality $(220, 220)$, corresponding to a diameter of $30.3nm$. Not all data points in the figure represent realistic nanotubes. Single wall nanotubes for example usually do no exceed a few nanometers in diameter and multi-wall nanotubes are filled with layers almost to the core. Thus, density values of actual nanotubes of that chirality are located on the right side of the chart, which represents a relatively large number of walls. In Figure 4-

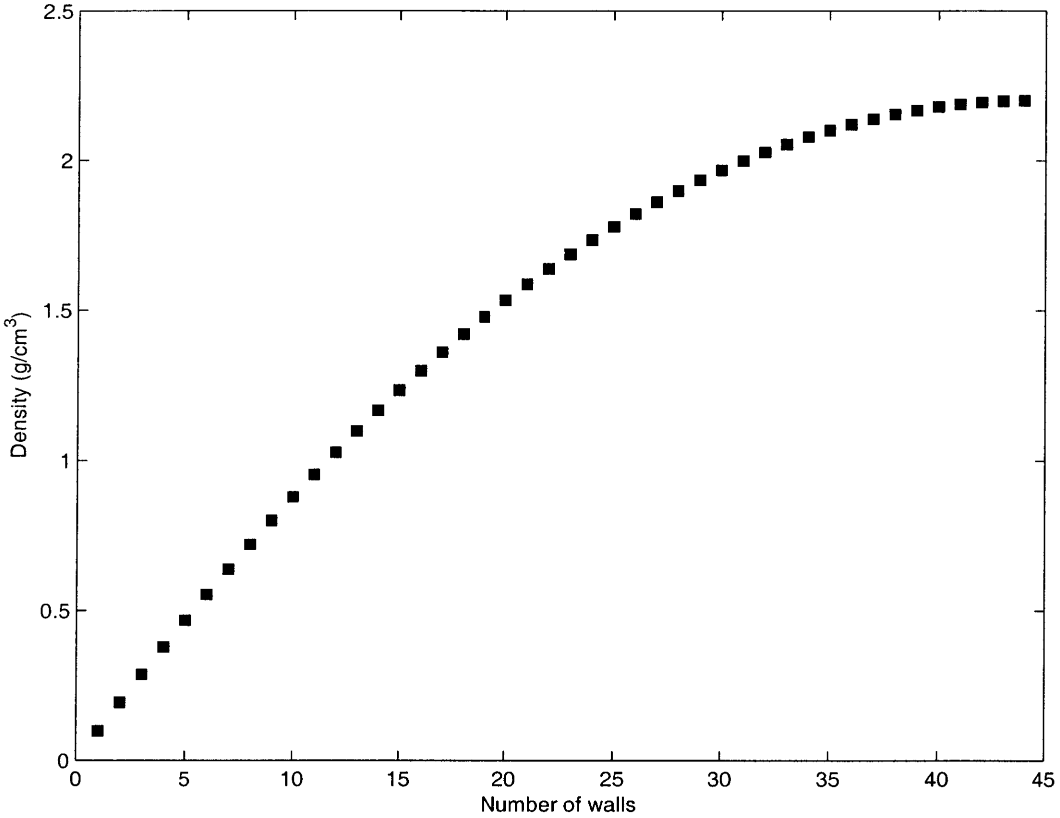

Figure 4-6: Density of a (220, 220) nanotube as a function of the number of walls

Chirality	10,10	10,10	10,10
NT length (nm)	141.38	141.38	141.38
NT diameter (nm)	1.3751	1.3751	1.3751
NT l/d	103	103	103
# of walls	1	1	1
NT density (g/cm^3)	2.15	2.15	2.15
NT wall stiffness (GPa)	4840	4840	4840
RVE length	100	90	75
RVE radius	2	1.8	1.5
RVE l/r	50	50	50
Matrix density (g/cm^3)	1.17	1.17	1.17
Matrix stiffness (GPa)	3.1	3.1	3.1
Volume fraction	8.33%	11.42%	19.74%
Weight fraction	7.16%	9.59%	15.57%

Table 4.2: Model data for nanotube volume fraction analysis

6, the external wall is held constant as walls are added internally. Consequently, the volume is fixed while nanotube walls with decreasing diameter and mass are added, resulting in the nonlinear relationship in the graph. Qian et al. (2000) use a density value of $2.16 g/cm^3$ for multi-wall nanotube with diameters around $30 nm$. Given that multi-wall nanotubes are filled almost all the way to the core, the density extracted from Figure 4-6 for $\sim$ 40 walls is in excellent agreement with the literature. The estimated density of a $(10, 10)$, single wall nanotube, such as the one used in the models, is $2.15 g/cm^3$.

4.2.2 Composite stiffness predictions

Three models were created with nanotube concentrations of 8.3%, 11.4% and 19.7% by volume, corresponding to 7.2%, 9.6% and 15.6% by weight. The nanotube diameter and aspect ratio were $1.38 nm$ and $\sim$ 100 respectively and the RVE aspect ratio was 50. In addition, periodic boundary conditions consistent with a staggered array were applied. Figure 4-7 shows a graph of the predicted axial stiffness values for the composite as a function of the nanotube weight fraction and compares it to the upper-bound solution. The results presented in Figure 4-7 suggest a strong, linear correlation between the nanotube concentration and the axial stiffness of the

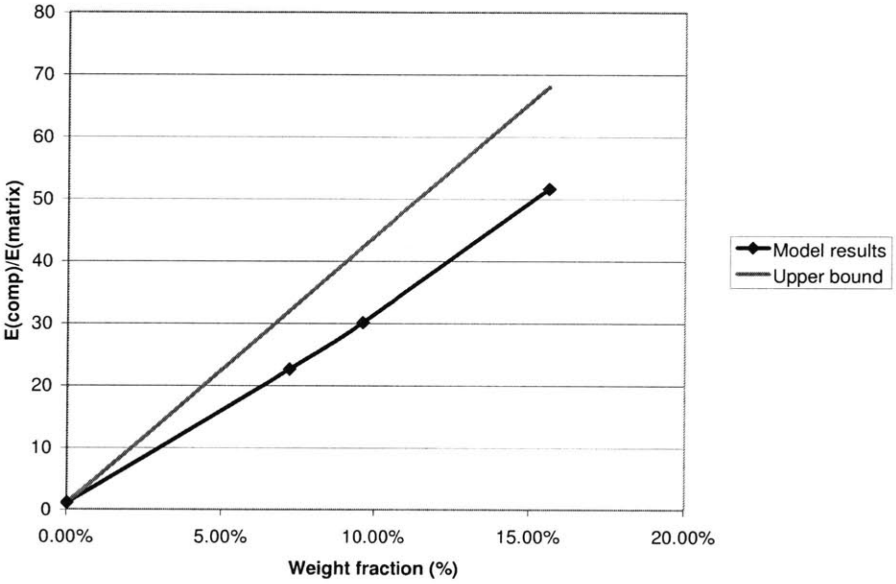

Figure 4-7: Predicted composite stiffness as a function of the nanotube weight fraction

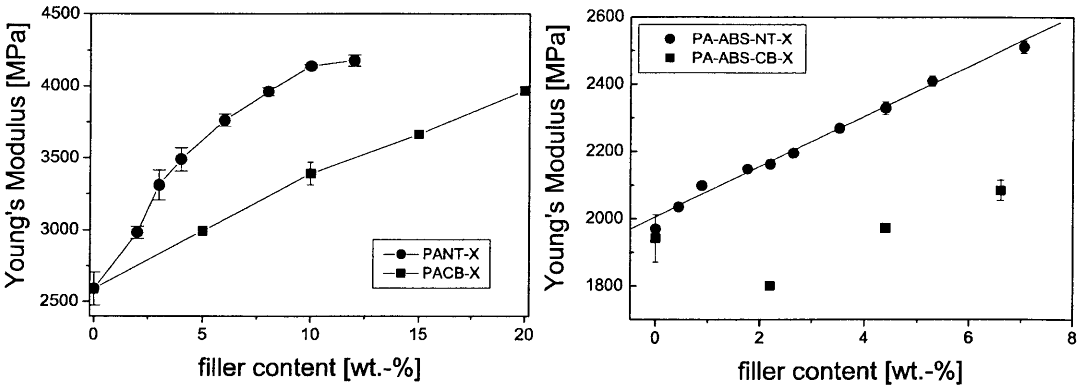

Figure 4-8: Young's modulus as a function of filler weight fraction for (a) multi-wall nanotube-filled polyamide-6 and carbon black-filled polyamide-6 composites and (b) multi-wall nanotube-filled polyamide-6/ABS blend and carbon black-filled polyamide-6/ABS blend composites (Meincke et al., 2004)

composite. Even at low weight fractions (~ 8%), the axial elastic modulus of the RVE is more than 20 times larger than the modulus of pure matrix material.

On the other hand, no firm conclusions can be drawn from experimental results available in related literature. Reports range from observations of an evident increase in elastic modulus, in some cases occurring linearly with respect to weight fraction, to deterioration of the stiffness even at low nanotube concentrations. Meincke et al. (2004) examined the mechanical properties of multi-wall nanotube-polyamide-6 and -polyamide-6/ABS-blend composites and compared them with the properties of similar carbon black-filled composites, as shown in Figure 4-8. In both composites, the stiffness increases with weight fraction, linearly in the case of the PA-6-ABS blend composite. The nanotubes had no preferred orientation in either system and they were well dispersed in the PA-6-based composite but clustered in the PA-6/ABS.

Kumar et al. (2002) also reported an increase in composite stiffness and other mechanical properties with weight fraction, when single wall nanotubes are added to PBO to form composite fibers, as shown in Table 4.3. According to the authors, nanotubes were highly aligned and well dispersed at both weight fractions.

Further evidence of stiffness improvements in nanotube-enabled polymer composites is provided by Andrews et al. (2002), who studied the macroscopic mechanical

sample	fiber diameter (μm)	tensile modulus (GPa)	strain to failure (%)	tensile strength (GPa)	compressive strength (GPa)
PBO	22 ± 2	138 ± 20	2.0 ± 0.2	2.6 ± 0.3	0.35 ± 0.6
PBO/SWNT (95/5)	25 ± 2	156 ± 20	2.3 ± 0.3	3.2 ± 0.3	0.40 ± 0.6
PBO/SWNT (90/10)	25 ± 2	167 ±15	2.8 ± 0.3	4.2 ± 0.5	0.50 ± 0.6

Table 4.3: Mechanical properties of PBO and SWCNT/PBO composite fibers (0%, 5% and 10% by weight) (Kumar et al., 2002)

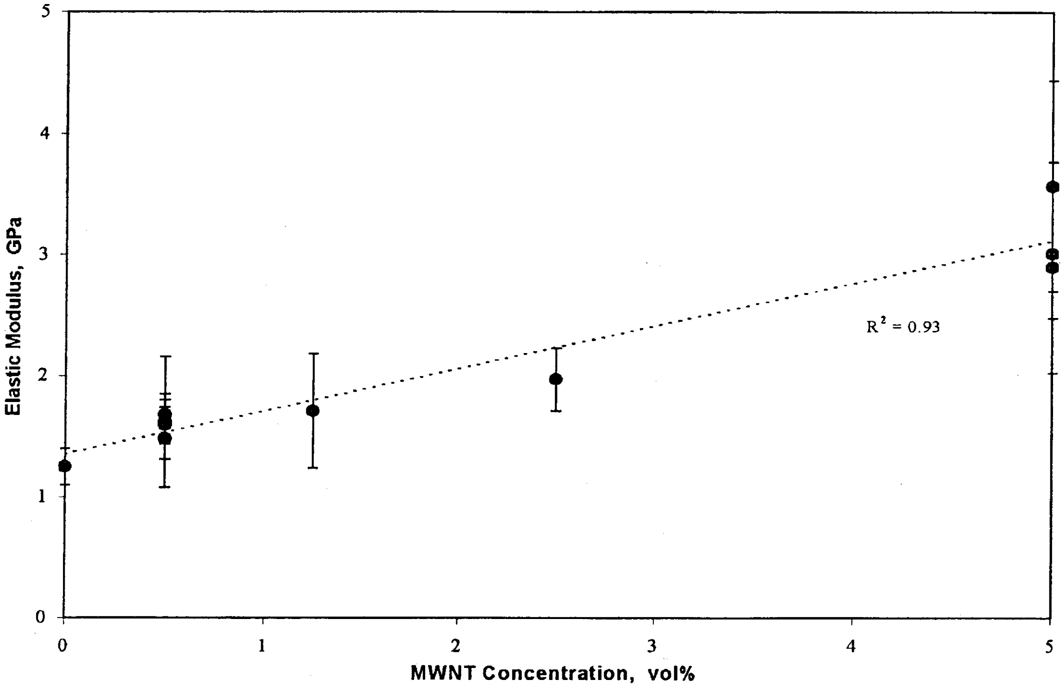

Figure 4-9: Young's modulus as a function of filler weight fraction for multi-wall nanotube-filled polypropylene composite fibers (Andrews et al. 2002)

behavior of multi-wall nanotube-enabled composite films and fibers using various polymers as matrices. The elastic modulus of the polypropylene-based composite film increased monotonically with nanotube concentration from $1.0GPa$ for the neat polymer to $2.4GPa$ for the 12.5% by volume composite. The stiffening effect was more evident in the corresponding composite fibers, as shown in Figure 4-9. The stiffness advantage of the fibers compared to same-system thin films stems from the improved axial alignment of nanotubes in fibers, induced by the large shear fields applied during extrusion. Andrews et al. also tested multi-wall nanotube-polystyrene composite films, with similar results as before, as shown in Figure 4-10. The graph indicates

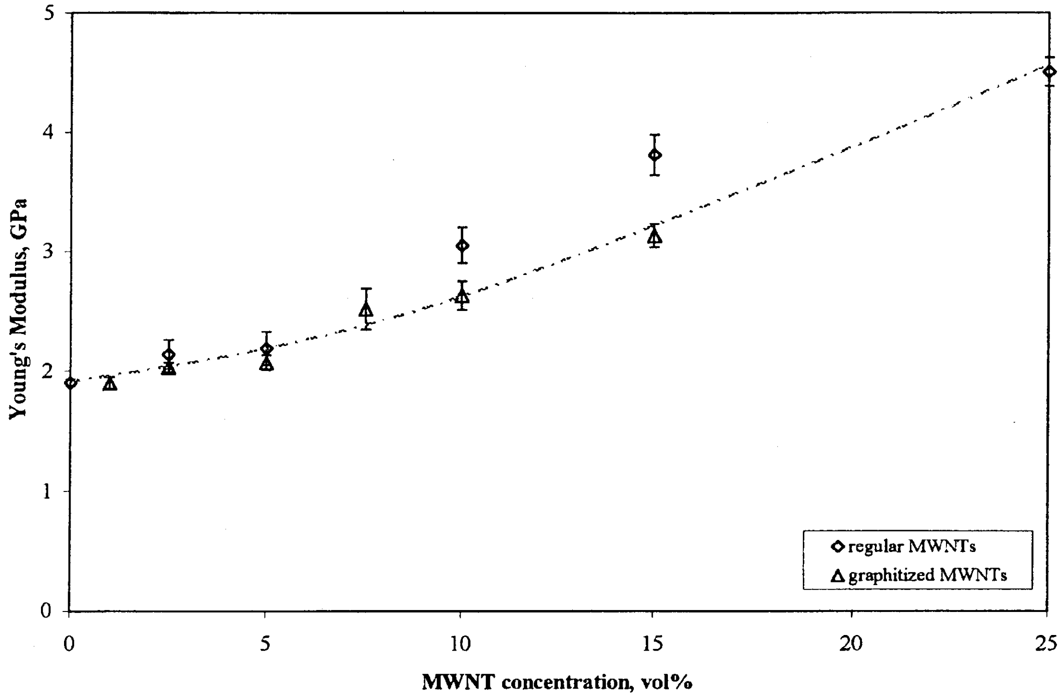

Figure 4-10: Young's modulus as a function of filler weight fraction for multi-wall nanotube-filled polystyrene composite films (Andrews et al., 2002)

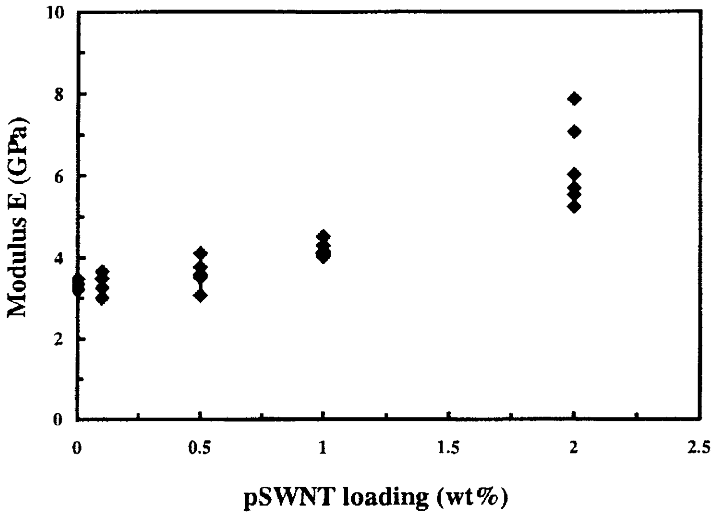

Figure 4-11: Young's modulus as a function of filler weight fraction for single wall nanotube-filled polymethylmethacrylate composite fibers (Du et al., 2003)

that the major increases in composite Young's modulus in this case are realized at concentrations above 10% by volume, resulting in an almost convex curve, contrary to the results in Figure 4-8 which suggest that the elastic modulus reaches a plateau.

Finally, Du et al. (2003) produced composite fibers using a coagulation method to mix purified single wall nanotubes with PMMA and measured the effects on the elastic tensile modulus of the fiber. A measurable increase in stiffness with increasing filler loading was observed in this composite system as well, as shown in Figure 4-11. The nanotubes were well-dispersed and well-aligned, as evidenced by micrographs and small-angle X-ray scattering accordingly.

So far, the trends that have been described are in agreement with the mechanical behavior predicted by the model. The experimental stiffness values are significantly lower than the values extracted from the model, which can be attributed to the underlying assumptions of the model. The perfect matrix-nanotube bonds, the staggered array and the perfect nanotube alignment are simplifications that do not reflect observations of realistic nanotube-enabled composites. In actuality, nanotubes are only weakly bonded to the matrix, they are randomly arranged and they are wavy, with only vaguely defined preferred orientations at best.

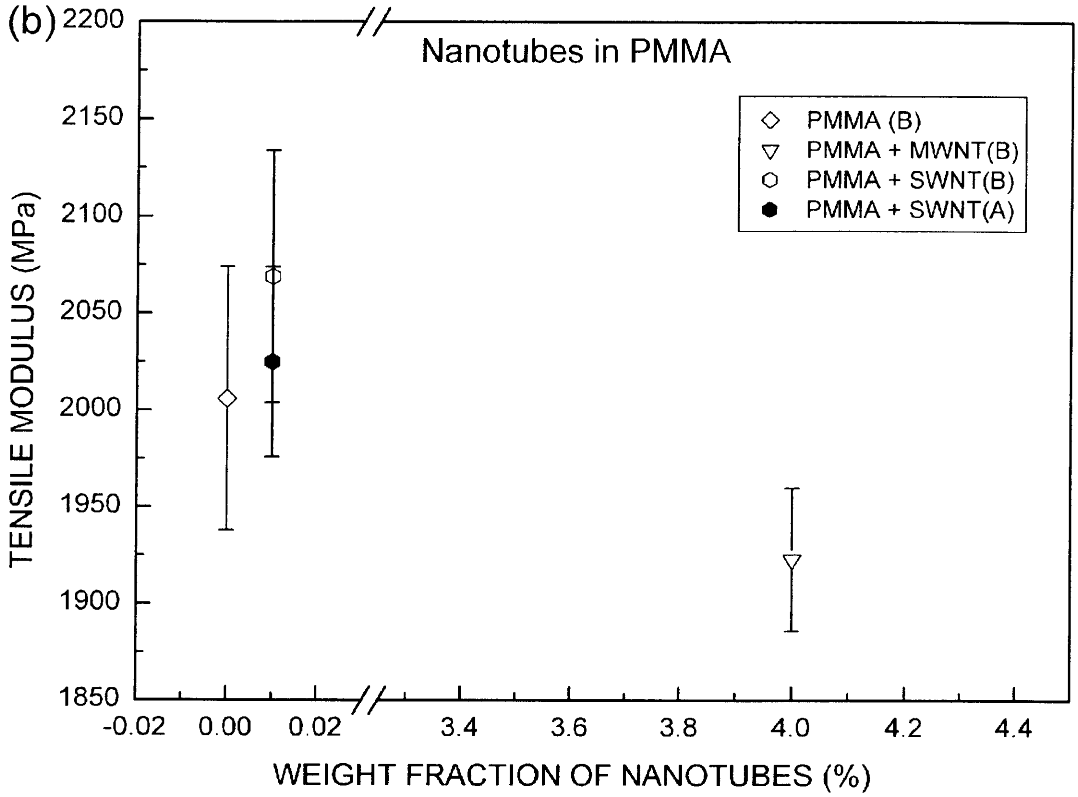

Figure 4-12: Young's modulus as a function of filler weight fraction for single and multi-wall nanotube-filled polymethylmethacrylate composite fibers (Cooper et al., 2002)

However, there have also been reports of either no effects or detrimental effects of the nanotube concentration on composite stiffness. In a study of single wall and multi-wall nanotube-enabled PMMA composite fibers, Cooper et al. (2002) reported very limited increase in tensile modulus at ultra-low weight fractions and larger decreases at higher loadings (Figure 4-12). The indexes (A) and (B) refer to composites prepared with PMMA particles larger and smaller than $200\mu m$. The nanotubes were well-dispersed and well-aligned as they were in the composites discussed by Winey.

Singh et al. (2003) reported similar findings for composite films made with entangled single wall nanotubes and polycarbonate. Values for the Young's modulus of the film were obtained from TMA tests, performed at two different cycling frequencies. Figure 4-13 summarizes the results. Considerable stiffness increases occur at very

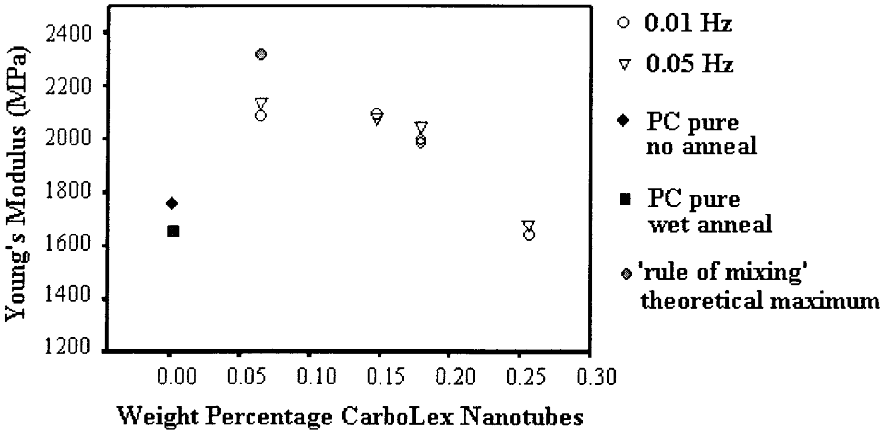

Figure 4-13: Young's modulus as a function of filler weight fraction for single wall nanotube-filled polycarbonate composite films (Sundararajan et al. 2003)

low nanotube concentrations, but the effect rapidly diminishes with increasing weight fraction.

The variety of the above results and the apparent contradictions among some of them highlight the complex nature of the reinforcing effects of carbon nanotubes when used as fillers in a polymer matrix. A number of parameters interact and determine the resulting macroscopic mechanical behavior of a nanotube-enabled composite. The strength of the bonds along the nanotube-matrix interface is of utmost importance, as it determines the amount of load transferred to the nanotubes. Internal load transfer in multi-wall nanotubes as well as load transfer among single wall nanotubes forming a rope also affect the stiffness of the composite. Furthermore, as it was illustrated earlier, the use of nanotubes in composite fibers has a more pronounced effect with respect to the stiffness than their use in thin films. Filler orientation and dispersion are also essential parameters for the composite elastic modulus. Finally, the processing methods and matrix material affect all the aforementioned parameters and, as a result, play a major role in determining how efficient the nanotubes as stiffeners.

Chapter 5

Finite element modelling of the mechanical behavior of a multi-nanotube volume element

As demonstrated in the previous two chapters, the single-nanotube RVE can provide useful insight into the parameters that affect the macroscopic mechanical behavior of a nanotube-enabled composite. Both geometric and load-transfer-related characteristics and their relative impact on the properties of the composite can be evaluated. Furthermore, thanks to a series of simplifying assumptions, the models of unit-cell RVEs are computationally very efficient, requiring limited processing power and facilitating the study of multiple model configurations in relatively short periods of time. These assumptions include the stacked and staggered periodic boundary conditions applied on the RVE, the perfect alignment of the nanotube to the loading axis and, in some cases, the perfect bonding between the nanotube and the matrix along their interface. While these simplifications reduce the computational requirements of the model, they limit its ability to examine the effects of dispersion, alignment and all related parameters. Although the staggered periodic boundary conditions simulate more realistically the nanotube dispersion in actual composites than the stacked boundary conditions do and render the model virtually immune to artifacts from variations in the RVE aspect ratio, they cannot capture the randomness of nanotube

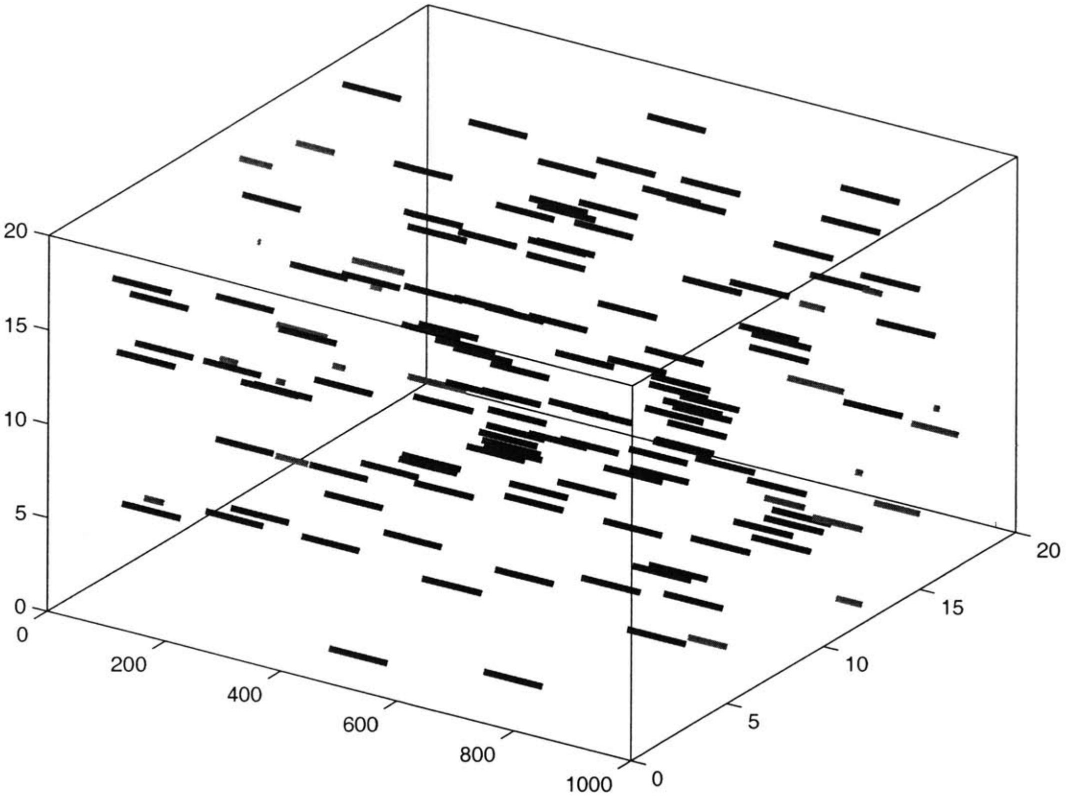

Figure 5-1: Three-dimensional volume element with randomly dispersed nanotubes

dispersion and all the phenomena associated with it, such as filler clustering, etc.. For this reason, volume elements with randomly dispersed nanotubes were created and modelled using finite element techniques.

5.1 Modelling details

The finite element models that were created for this study were based on the three-dimensional volume elements with randomly dispersed nanotubes that were discussed in Chapter 2, shown in Figure 5-1. More specifically, the MATLAB module that created those volume elements was coupled with an input file generator that encoded all the necessary information into a format suitable for ABAQUS to process. Most parameters are given as inputs to the code. These include the matrix and nanotube mechanical properties, the RVE dimensions, the nanotube length and volume fraction

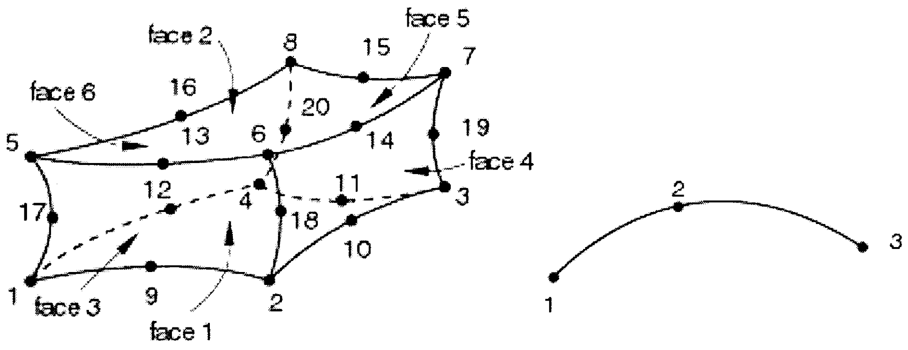

20 - node element

3 - node element

Figure 5-2: Types of elements used to mesh the matrix and the nanotube

as well as the macroscopically applied strain on the RVE.

5.1.1 Material and geometric properties

For all the studies that will be discussed in this chapter, the elastic modulus of the matrix was $3.1GPa$ and the Poisson's ratio was 0.3 for the matrix and 0.19 for the nanotube. For the nanotube aspect ratio and volume fraction studies the elastic modulus of the nanotube was assumed to be $1TPa$ while it varied as specified later in the other studies. Both the matrix and the filler were assumed to behave elastically throughout the simulation. The nanotubes had a fixed diameter of $1nm$ but their length and thus, their aspect ratio, could vary. They were randomly dispersed inside the matrix and perfectly aligned to the axis of loading. Furthermore, they were assumed to be perfectly bonded to the matrix.

5.1.2 Modelling parameters

Meshing

20-node, hexahedral (brick) continuum elements were used to mesh the matrix while 3-node, quadratic beam elements were used for the nanotubes, as shown in Figure 5-2. Beam elements have both displacement and rotational degrees of freedom as opposed to continuum elements, for which only the displacement degrees of freedom are active.

This apparent mismatch allows the nanotubes to rotate rigidly around their axis, since that degree of freedom is free. This issue was resolved by fully constraining the rotational degree of freedom of all nanotubes about their axis.

Boundary conditions

A RVE is a sample volume of a whole entity and is large enough to account for all characteristics in the large-scale sample and yet small enough to be computationally efficient. Conceptually, the RVE is surrounded by identical volume elements, arranged periodically in a three-dimensional, stacked array. As a result, any one point on the surface of the RVE also belongs to one or more neighboring RVEs. This periodicity is implemented by a set of boundary conditions, applied on all surface nodes.

The implementation of the periodic boundary conditions requires the creation of two auxiliary, *fictitious* nodes at arbitrary points in space outside the RVE, whose displacements, u_i, by definition, correspond to the individual components of the macroscopic displacement gradient, $H_{ij} = \frac{\partial u_i}{\partial x_j}$, of the RVE (Danielsson et al., 2002). Due to the symmetry of the tensor, only six individual components need to be determined, corresponding to two auxiliary nodes in three-dimensional space. For the purpose of applying these boundary conditions, the surface nodes can be divided into corner nodes, edge nodes and surface nodes, each type requiring different boundary conditions, since they are shared by a different number of neighboring RVEs.

Corner nodes are shared by 8 neighboring RVEs. Corner node O in Figure 5-3 is fully constrained, i.e. $u_i = 0$, $i = 1, 2, 3$. The constraint equations for node A are given by

$$u_i = L_1 H_{i1} \tag{5.1}$$

and for node D they are given by $u_i = L_1 H_{i1} + L_3 H_{i3}$. The boundary conditions for the remaining corner nodes are formulated in a similar manner.

Edge nodes, which include all nodes along an edge except the two corresponding corner nodes, are shared by 4 neighboring RVEs. As a result, a generic point Φ on edge OA for example, with coordinates $(\Phi, 0, 0)$, has three constrained image points,

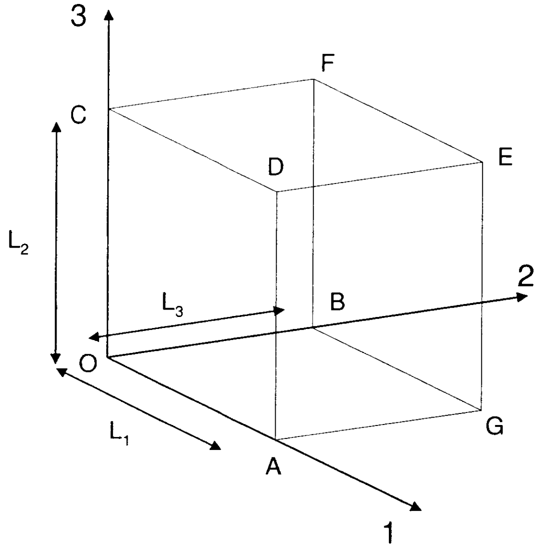

Figure 5-3: Schematic of three-dimensional volume element

Φ_2, Φ_3 and Φ_{23}, with coordinates $(\Phi, L_2, 0)$, $(\Phi, 0, L_3)$ and (Φ, L_2, L_3) accordingly. The constraint equations for the three constrained image nodes are then given by

$$\Phi_2 \rightarrow u_i = u_i^{\Phi} + L_2 H_{i2} \tag{5.2}$$

$$\Phi_3 \rightarrow u_i = u_i^{\Phi} + L_3 H_{i3} \tag{5.3}$$

$$\Phi_{23} \rightarrow u_i = u_i^{\Phi} + L_2 H_{i2} + L_3 H_{i3} \tag{5.4}$$

where u_i^{Φ} are the displacements of the control node Φ. Similar equations can be developed for nodes on edges *OB* and *OC*.

Finally, face nodes, which include all nodes on a surface except the corner and edge nodes, are shared by 2 neighboring RVEs and each of these nodes has one constrained image node. A point P for example, located on face *OADC*, with coordinates $(P_1, 0, P_3)$, has an image point P' with coordinates (P_1, L_2, P_3). The constraint equations are given by

$$u_i^{P'} = u_i^{P} + L_2 H_{i2} \tag{5.5}$$

where u_i^P are the displacements of the control node P. The constraint equations for the two other free faces, *OAGB* and *OBFC* are formulated accordingly.

NT length (nm)	15	30	50	80
NT diameter (nm)	1	1	1	1
NT l/d	15	30	50	80
NT stiffness (GPa)	1000	1000	1000	1000
RVE length (nm)	120	120	120	120
RVE width (nm)	7	7	7	7
RVE l/w	17	17	17	17
Matrix stiffness (GPa)	3.1	3.1	3.1	3.1
Volume fraction	5%	5%	5%	5%

Table 5.1: Model data for nanotube aspect ratio analysis

5.2 Effect of nanotube aspect ratio

A similar analysis to that performed for the single nanotube RVE was conducted to study the effect of the nanotube aspect ratio on the macroscopic axial stiffness of the composite. All parameters except the nanotube length were held constant, as suggested by Table 5.1. Furthermore, for each geometry, multiple realizations of the same model were created in order to study the variation in macroscopic properties due to variations in nanotube dispersion, generated by the randomization code. Figure 5-4 displays representative RVEs for each of the four configurations that were considered.

All models were loaded to 4% strain. Figure 5-5 summarizes the results for each model as well as the averages and standard deviation within each aspect ratio case. The variation in the predicted stiffness of models with identical geometric specifications is due to the randomness of the nanotube dispersion. This variation captures the effect of parameters such as the degree of filler clustering on the macroscopic mechanical behavior of the composite.

The stiffness prediction results are consistent with the findings from the single nanotube RVE, which suggested a significant increase in stiffness with increasing nanotube aspect ratio. As the nanotube length increases, the maximum longitudinal strain in the nanotube as well as the length over which it is sustained increase, thus improving the nanotube's capacity to carry load. In the limiting case of a continuous

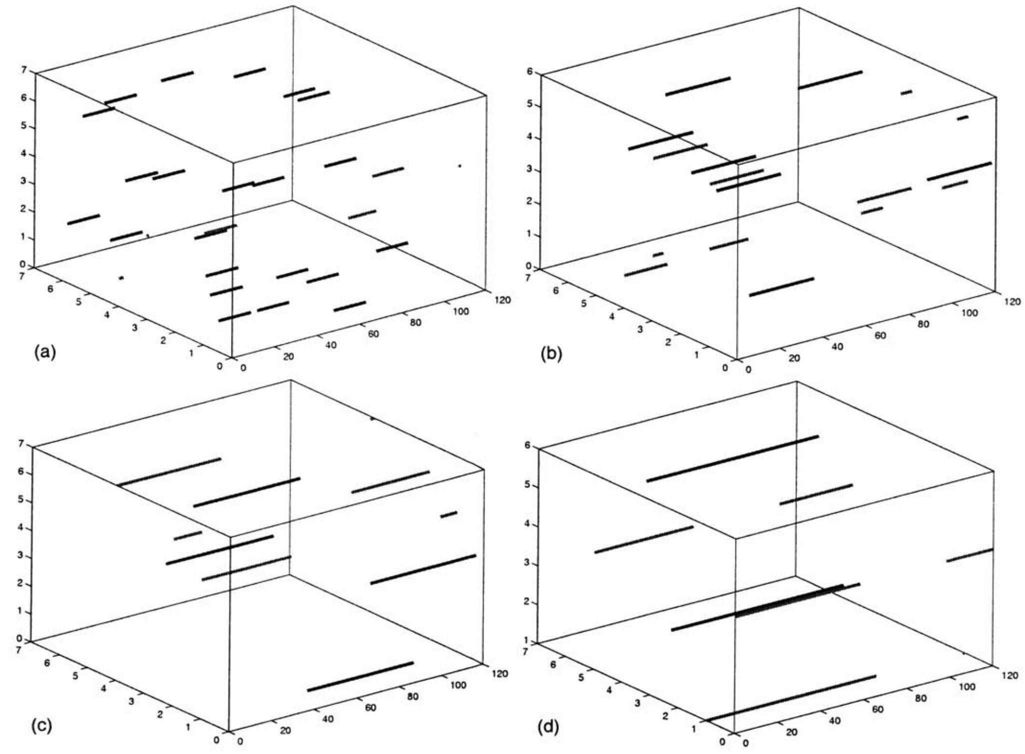

Figure 5-4: RVEs with nanotube aspect ratios of (a) 15, (b) 30, (c) 50 and (d) 80

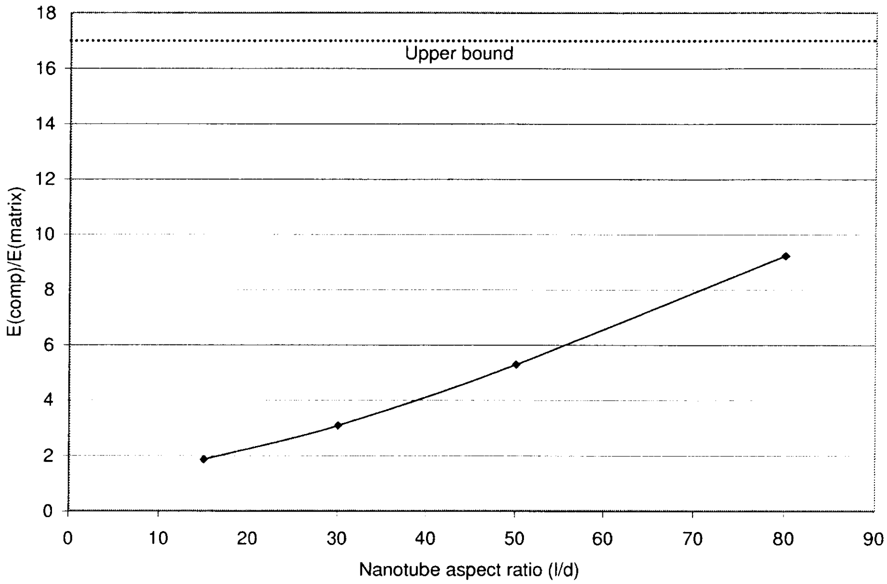

NT l/d	15	30	50	80
Composite stiffness (GPa)	5.81	8.66	19.64	25.89
	5.66	9.11	15.00	27.83
	5.54	10.69	14.26	31.81
Average	5.67	9.49	16.30	28.51
St Dev	0.14	1.07	2.92	3.02

Figure 5-5: Stiffness results for nanotube aspect ratio analysis

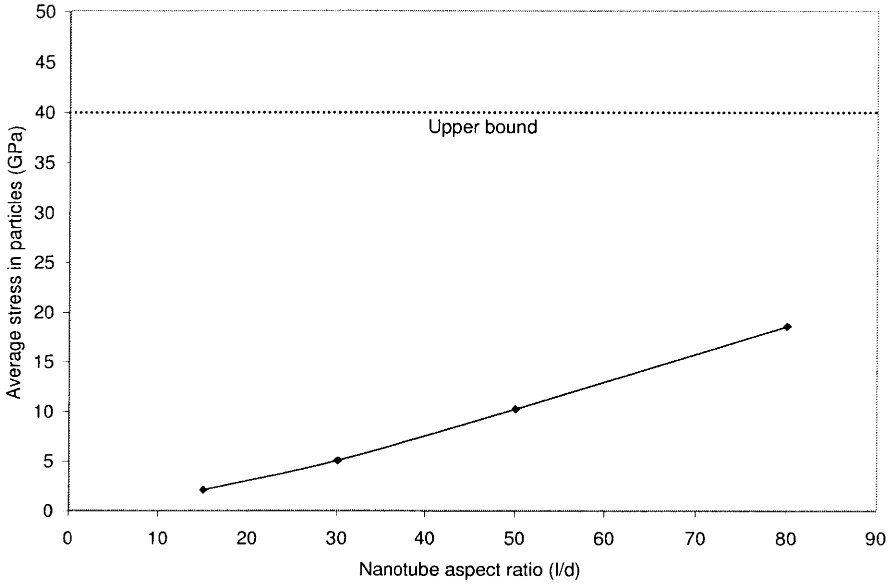

Figure 5-6: Average particle stress for nanotube aspect ratio analysis

fiber, the particle's longitudinal strain equals the macroscopic strain in the composite. Thus, longer nanotubes carry larger loads and have a more pronounced stiffening effect on the composite. The results from the simulation are consistent with this observation. Figure 5-6 illustrates the variation of the average longitudinal stress over all particle elements as the nanotube aspect ratio increases. Figures 5-7 to 5-10 highlight the differences in the longitudinal stress of particles with different aspect ratios. The maximum longitudinal stress in these cases increases monotonically with increasing particle aspect ratio and ranges from $4.3GPa$ for $l/d = 15$ to $43.5GPa$ for $l/d = 80$. Contrary to the findings from the single nanotube RVE analysis, strain shielding did not affect the predicted macroscopic response of the multi-nanotube RVE as the longitudinal stiffness increased steadily with nanotube aspect ratio, at least within the aspect ratio range that was investigated.

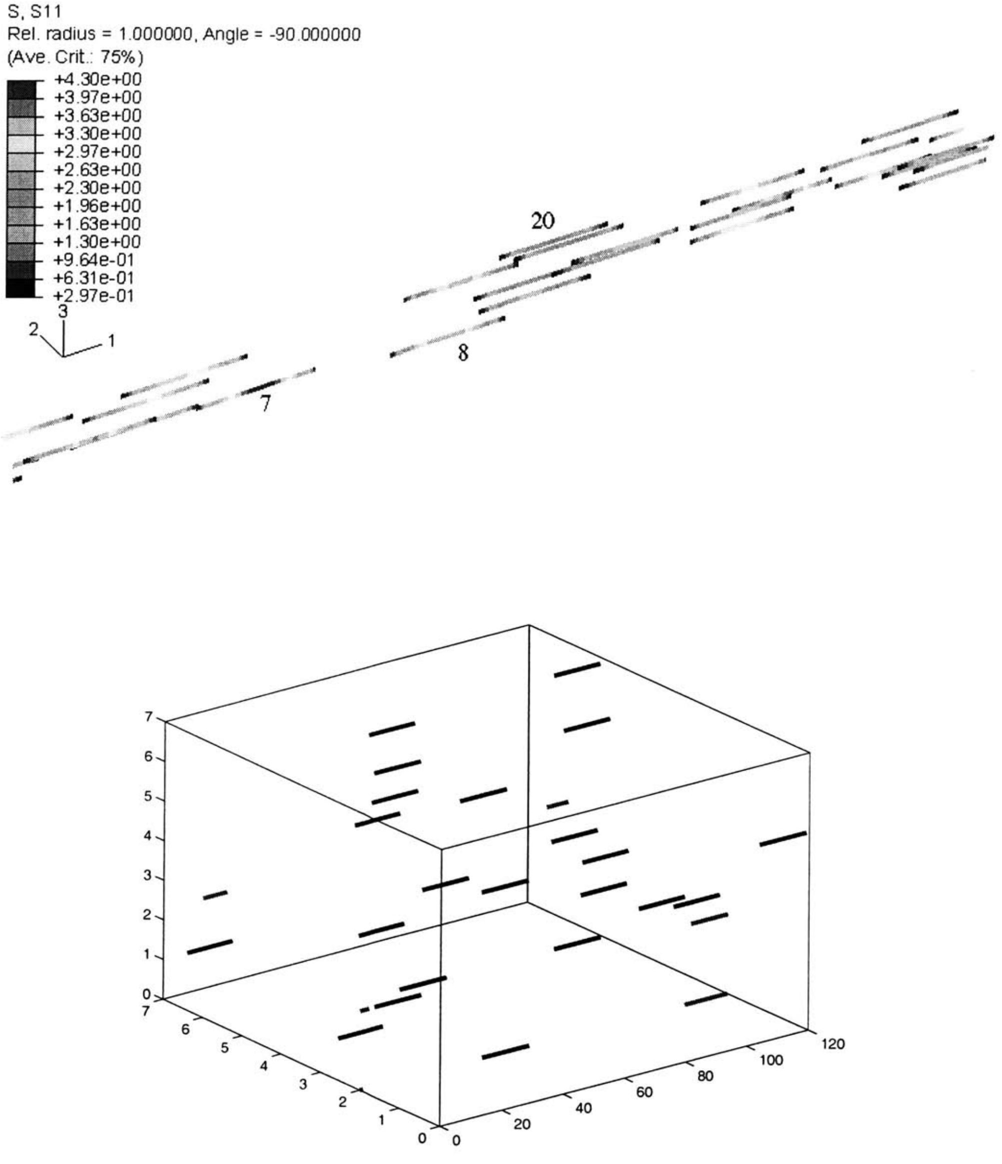

Figure 5-7: Longitudinal stress contours for particles with $l/d = 15$ and the corresponding RVE

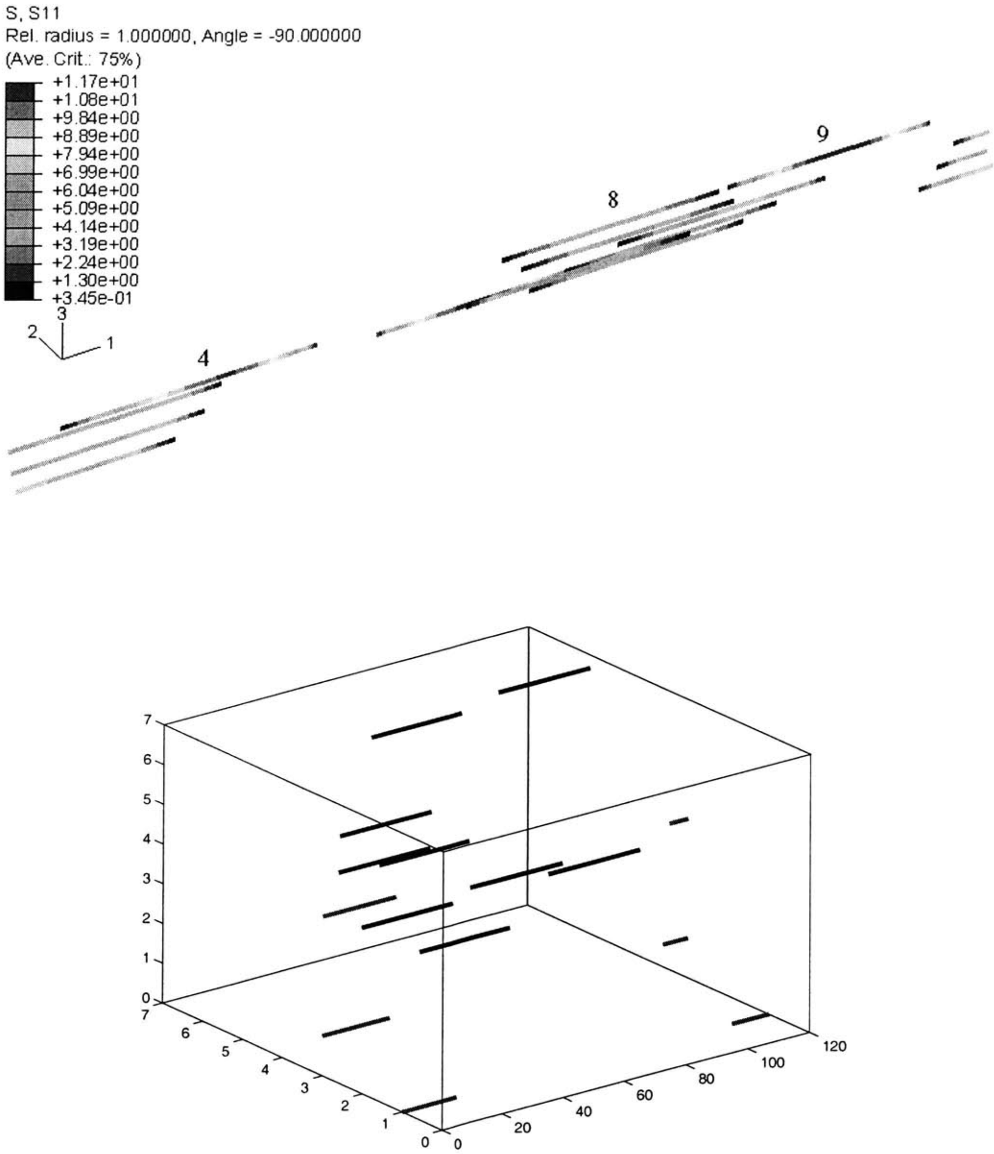

Figure 5-8: Longitudinal stress contours for particles with $l/d = 30$ and the corresponding RVE

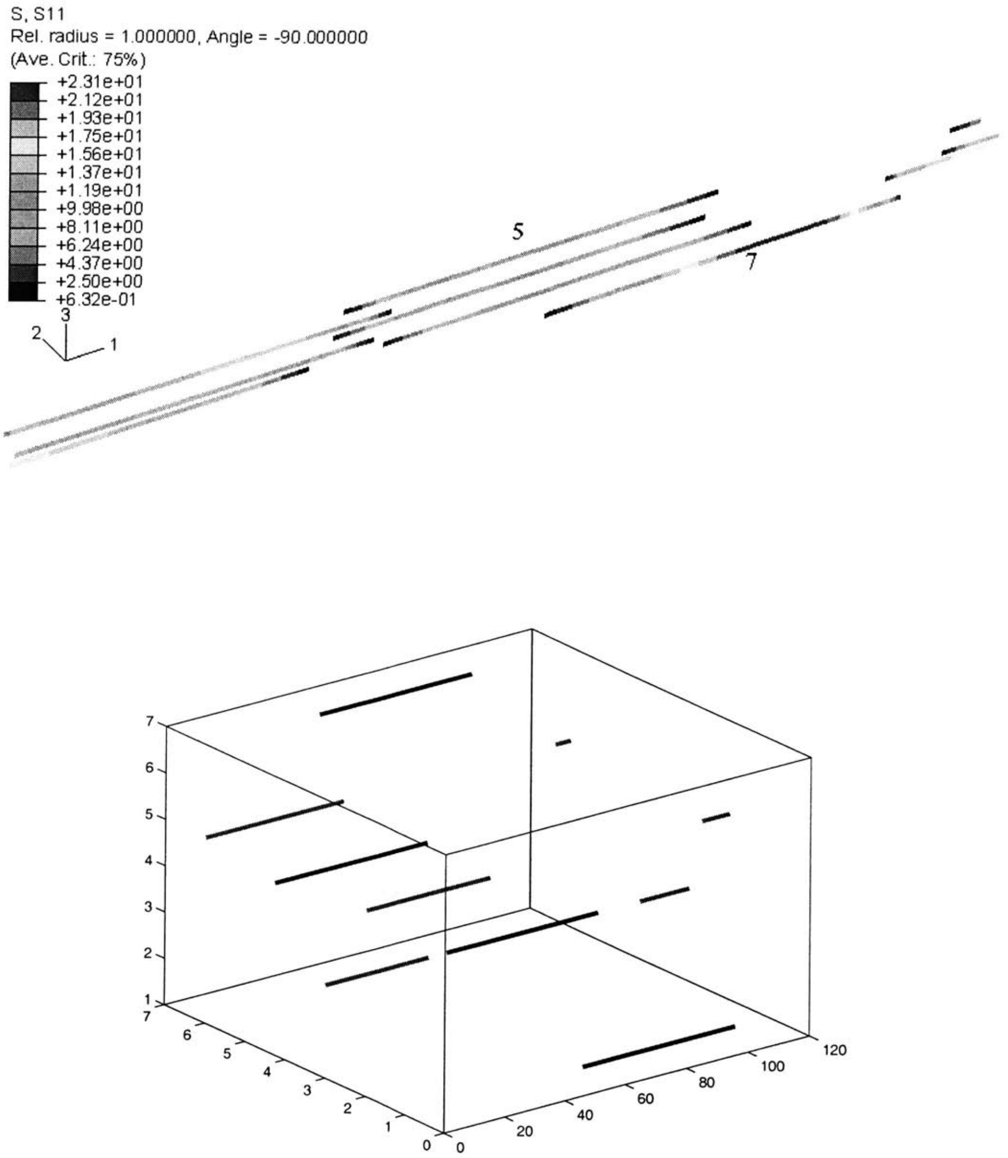

Figure 5-9: Longitudinal stress contours for particles with $l/d = 50$ and the corresponding RVE

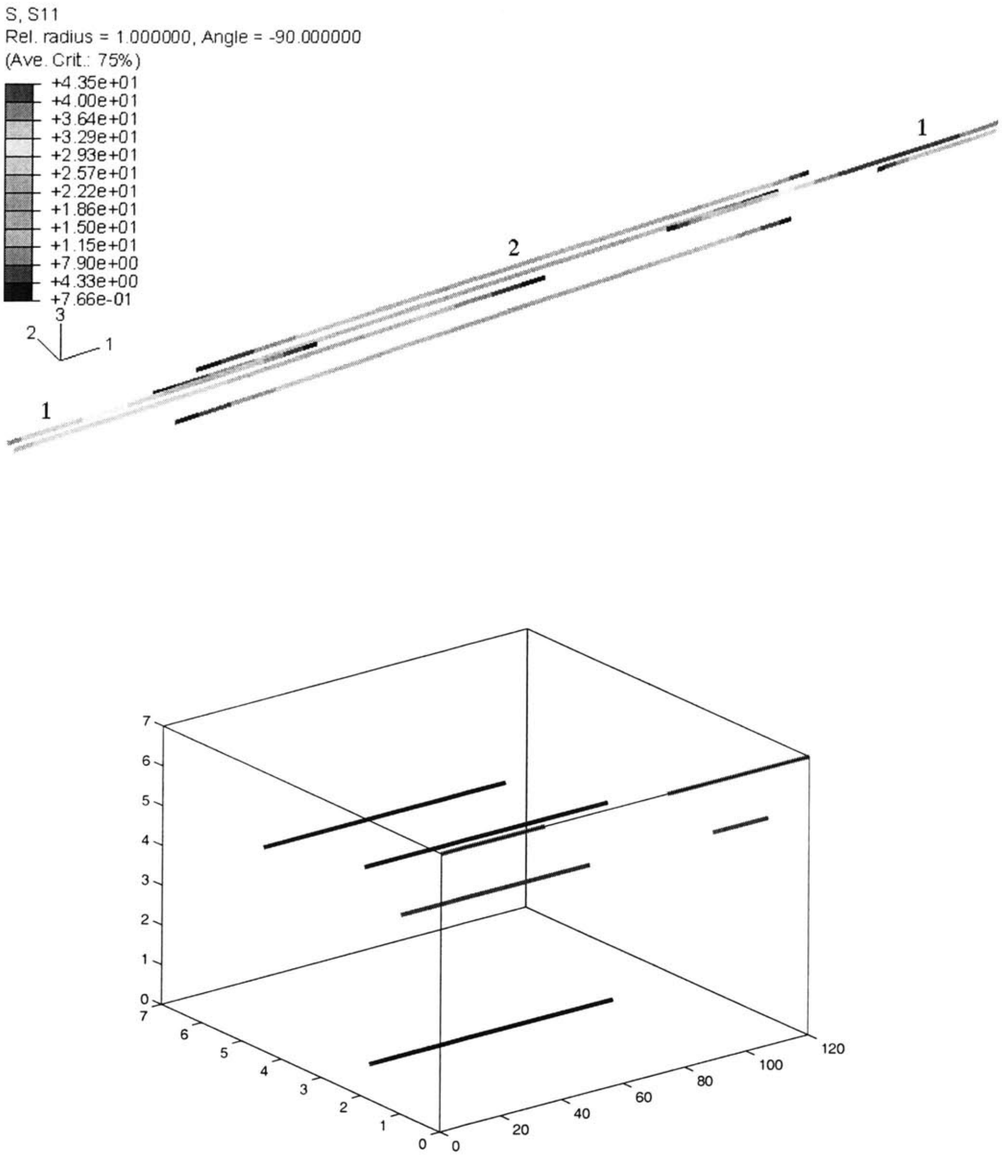

Figure 5-10: Longitudinal stress contours for particles with $l/d = 80$ and the corresponding RVE

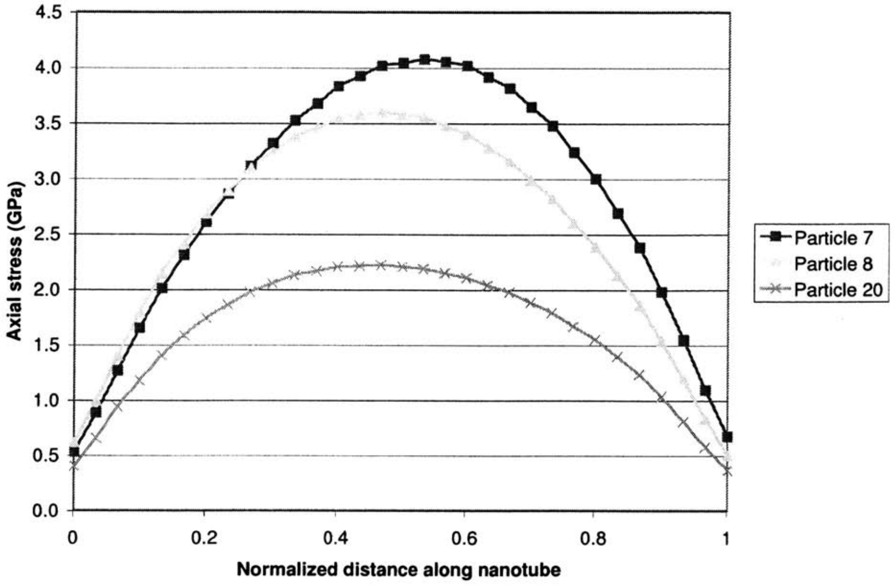

Figure 5-11: Axial stress distribution along selected labelled particles from Figure 5-7

Figures 5-11 to 5-12 illustrate the axial stress distribution along selected labelled particles from Figures 5-7 to 5-10. Particle interactions between laterally adjacent nanotubes essentially shield the matrix in the region from straining with adverse consequences for the composite stiffness. Since load transfer to the nanotube occurs both through the end caps (normal load) as well as through shear at the walls, the reduction in matrix strain results in a reduction in load transfer to the nanotube, as further attested by the plotted stress distributions, thus impairing the stiffening effect on the composite.

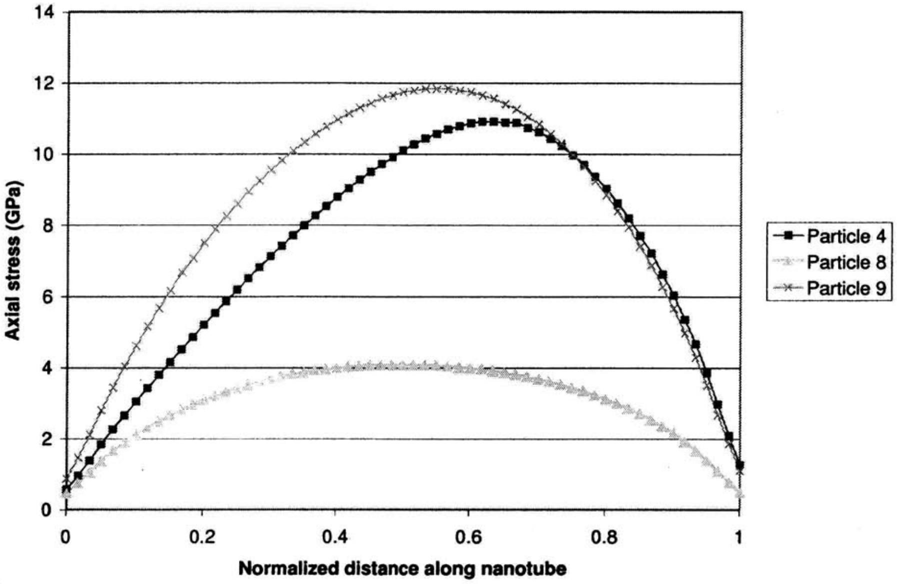

Figure 5-12: Axial stress distribution along selected labelled particles from Figure 5-8

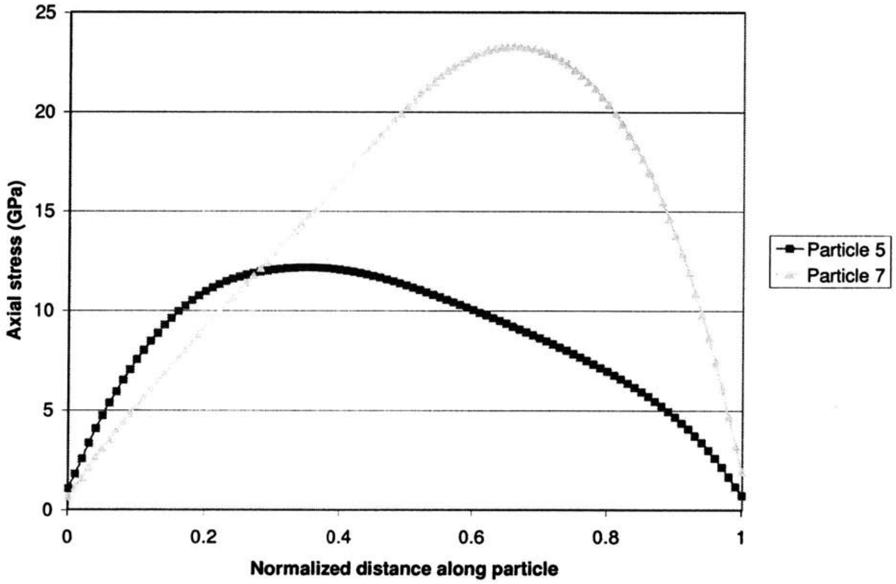

Figure 5-13: Axial stress distribution along selected labelled particles from Figure 5-9

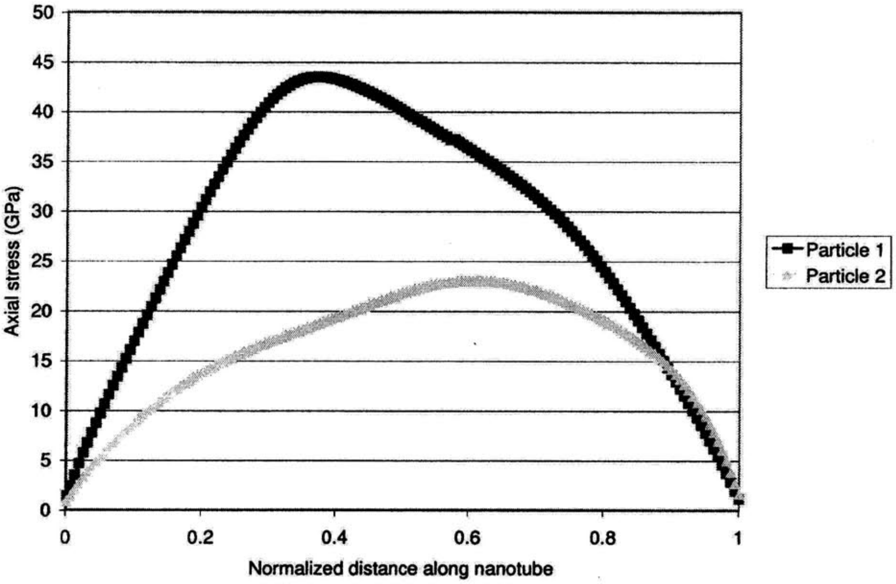

Figure 5-14: Axial stress distribution along selected labelled particles from Figure 5-10

NT length (nm)	80	80	80	80
NT diameter (nm)	1	1	1	1
NT l/d	80	80	80	80
NT stiffness (GPa)	1000	1000	1000	1000
RVE length (nm)	120	120	120	120
RVE width (nm)	7	7	7	7
RVE l/w	17	17	17	17
Matrix stiffness (GPa)	3.1	3.1	3.1	3.1
Volume fraction	5%	15%	30%	50%

Table 5.2: Model data for nanotube volume fraction analysis

5.3 Effect of nanotube volume fraction

The effect of the nanotube load in the matrix, expressed as the volume fraction of the composite, was investigated through a series of models, in which all parameters were held constant except for the volume fraction. Table 5.2 lists the details about the geometry and the material properties for each model. Figure 5-15 shows the four RVEs that were modelled for this analysis. All models were loaded to a maximum uniaxial strain of 4% and their axial stiffness was measured and plotted, as shown in Figure 5-16.

Even at low nanotube concentrations, the increase in the axial composite stiffness is dramatic. It needs to be emphasized though, as it was done for the single nanotube RVE models, that these results should always be evaluated with careful consideration of the relevant underlying assumptions, namely the rigid bond between the nanotube and the matrix, the perfect alignment of the nanotubes and the completely random dispersion. Such idealizations make the overall increase in axial composite stiffness more pronounced and consequently, the predicted values obtained from these models serve as theoretical upper limits to the stiffening effect of nanotubes in a matrix.

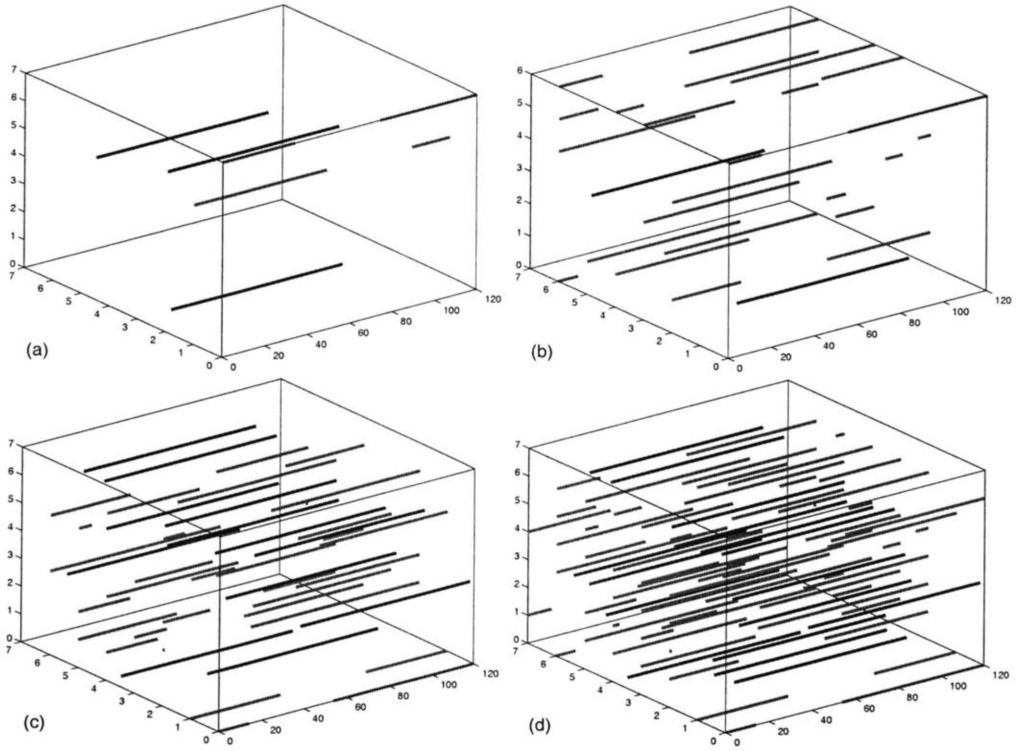

Figure 5-15: RVEs with nanotube volume fraction of (a) 5%, (b) 15%, (c) 30% and (d) 50%

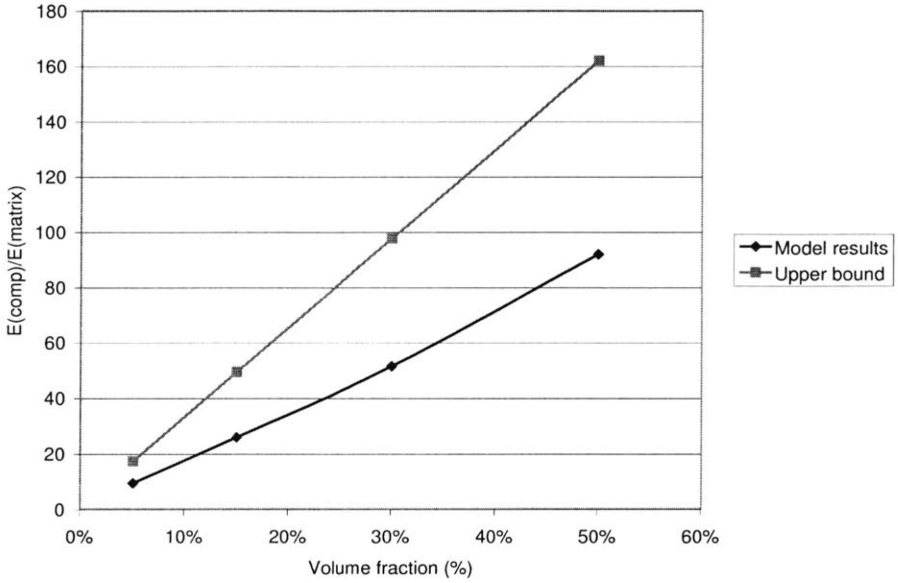

Volume fraction	5%	15%	30%	50%
E (GPa)	28.51	79.86	158.94	284.44

Figure 5-16: Stiffness results for nanotube volume fraction analysis

NT length (μm)	8	8
NT diameter (nm)	50	50
NT l/d	160	160
# of load-carrying walls	1	60
NT stiffness (GPa)	29	1000
RVE length (μm)	12	12
RVE width (μm)	0.7	0.7
RVE l/w	17	17
Matrix stiffness (GPa)	3.1	3.1
Volume fraction	1.3%	1.3%

Table 5.3: Geometric data for the multi-wall nanotube internal load transfer study

5.4 Effect of wall-to-wall load transfer within multi-wall nanotubes

In order to investigate the effect of load transfer within the walls of a multi-wall nanotube, two scenarios were simulated: one in which load was transferred internally, through wall-to-wall van der Waals interactions and another in which no load was transferred from the outer wall, thus behaving as a large-diameter single wall nanotube. Table 5.3 summarizes the geometric properties of both models. A value of $50nm$ for the outer diameter corresponds to an armchair nanotube, with approximate outer-wall chirality (365,365). A 60-wall nanotube with this diameter has a hollow core with diameter $\sim 10nm$.

In order to estimate the effective stiffness of a multi-wall nanotube, capable of transferring load internally, both the walls and the van der Waals interactions were simulated as a set of linear springs, arranged in series and in parallel as shown in Figure 5-17. Load is assumed to be transferred internally in the normal direction and through the end-caps only, as van der Waals interactions cannot accommodate shear load transfer. Figure 5-18 shows a plot of the effective stiffness of a multi-wall nanotube, with a fixed outer diameter of $50nm$, as a function of the number of load-carrying walls. At 60 walls, the effective stiffness of the nanotube is $1TPa$ while, in the limiting case of a single wall with the same diameter, the stiffness drops to $29GPa$, which highlights the magnitude of the effect the internal load transfer mechanisms

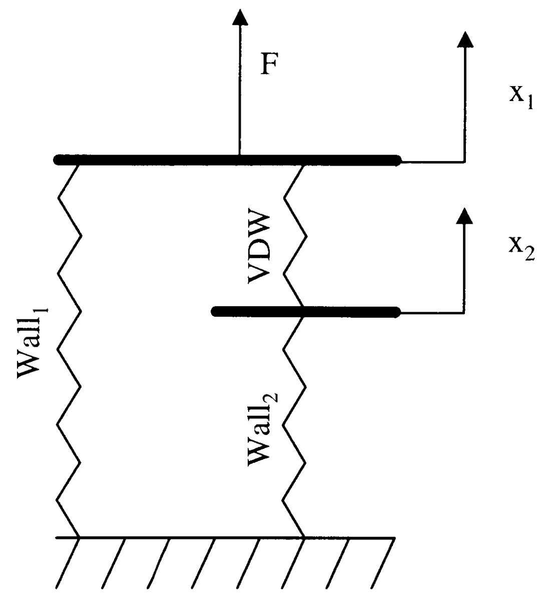

Figure 5-17: Schematic showing the spring model used for the calculation of the effective stiffness of a multi-wall nanotube

can have on the stiffness of the nanotube.

This effect further extends into the macroscopic axial stiffness of the reinforced composite. As Figure 5-19 suggests, if load is transferred internally in a multi-wall nanotube, composite stiffening is significant even at low nanotube concentrations. On the other hand, if no load is carried by the internal walls, most likely due to poor wall-to-wall interaction leading to external wall debonding, only a limited increase in composite stiffness is observed.

5.5 Effect of curvature

The effect of curvature, a common characteristic of nanotubes in an actual matrix, on the macroscopic stiffness was also investigated, using similar 3-D models as previously. Curvature was induced by defining the center node of each nanotube beam element at an off-axis location, forming a parabola with the two edge nodes, as shown in Figure 5-20. The common RVE that was used for all three model is shown in Figure 5-21

Table 5.4 summarizes the data for relevant geometric parameters used in this

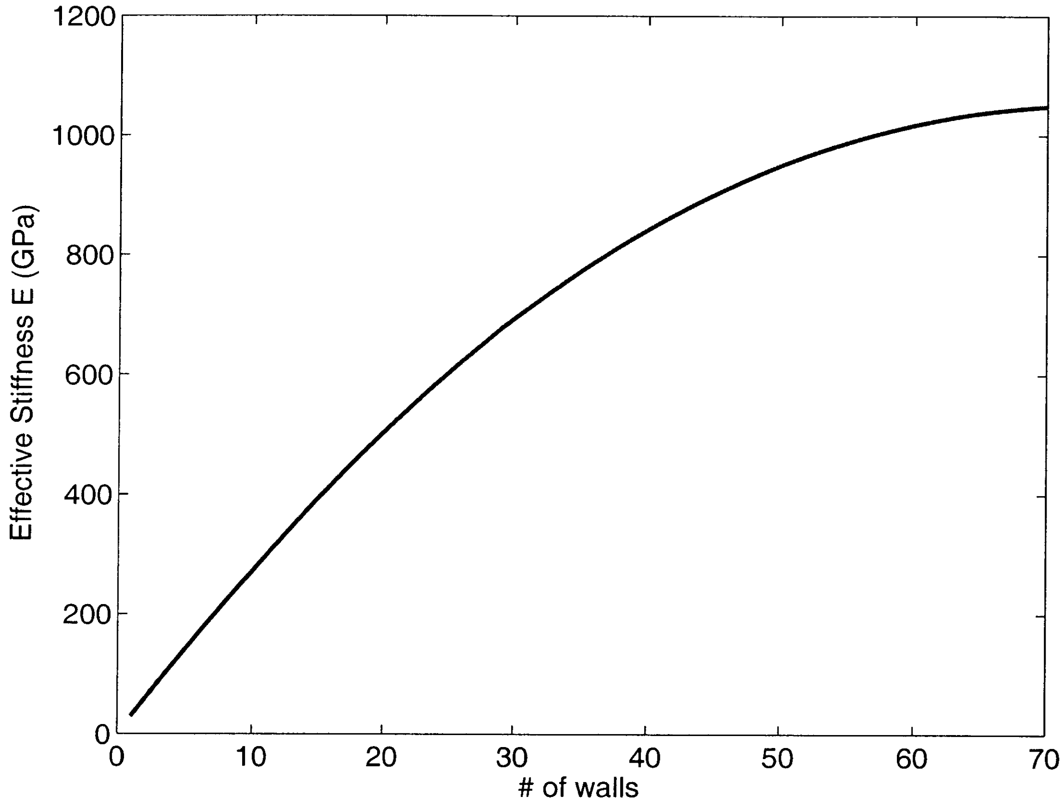

Figure 5-18: Variation of the nanotube effective stiffness with the number of load-carrying walls

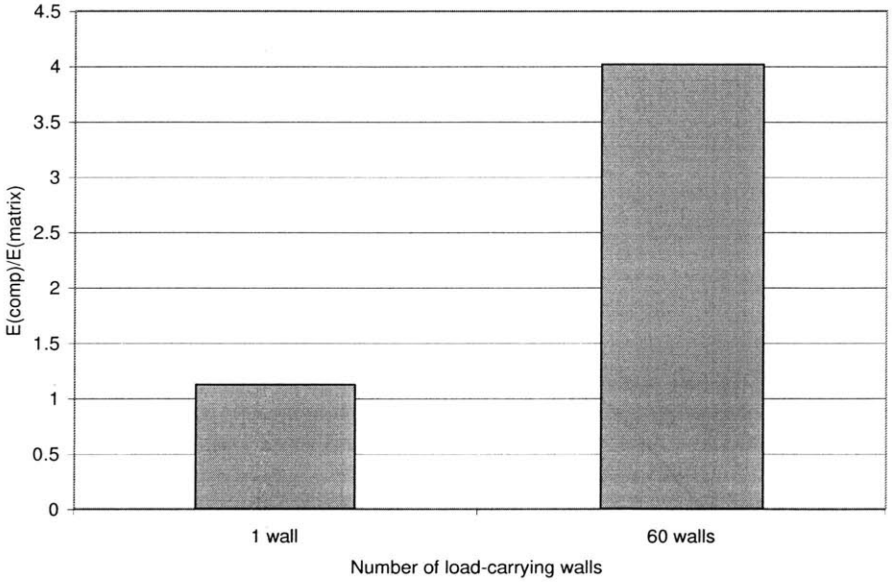

Figure 5-19: Normalized composite stiffness for 1 and 60 load-carrying walls in a multi-wall nanotube

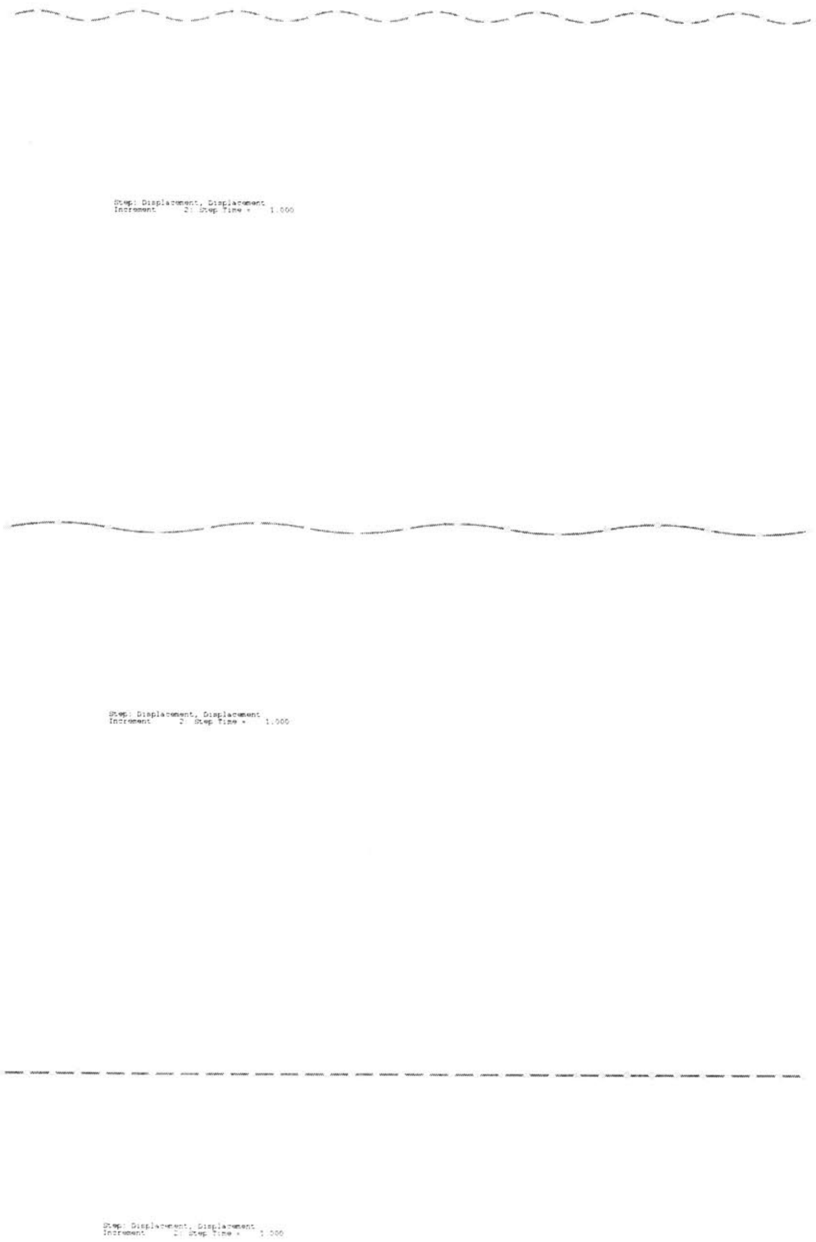

Figure 5-20: Sample nanotubes from each of the three models used for the curvature analysis

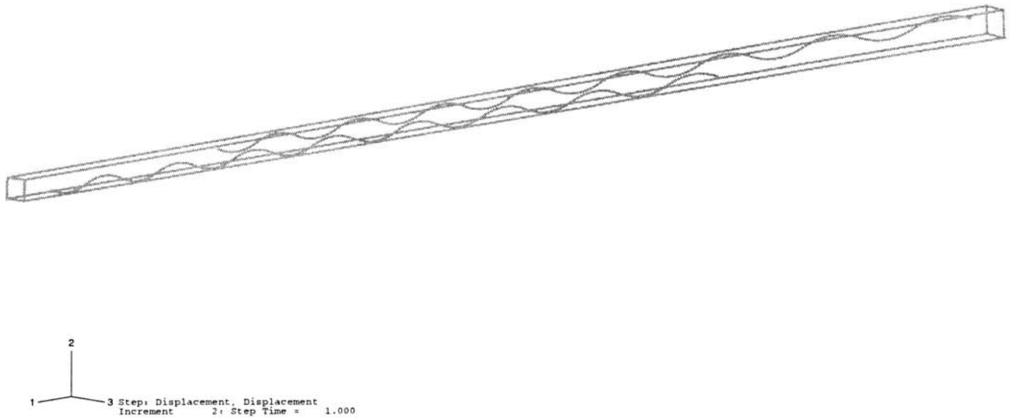

Figure 5-21: RVE used for the curvature analysis

analysis. Two models containing nanotubes with different curvature were created and compared to an identical model with perfectly straight nanotubes. In all cases, the nanotubes were assumed to contain multiple walls. There were two variations of the straight nanotube model, one assuming all walls were carrying load and the other assuming only the outer wall was being loaded. It was not necessary to make that distinction for the case of the curved models since the internal walls do resist bending and provide flexural rigidity, thanks to the van der Waals interactions among them.

NT length (μm)	16	16	16	16
NT diameter (nm)	50	50	50	50
NT l/d	320	320	320	320
NT stiffness (GPa)	1000	1000	1000	29
Curvature (λ/α)	40	20	N/A	N/A
RVE length (nm)	220	220	220	220
RVE width (nm)	4	4	4	4
RVE l/w	55	55	55	55
Matrix stiffness (GPa)	3.1	3.1	3.1	3.1
Volume fraction	1.8%	1.8%	1.8%	1.8%

Table 5.4: Geometric data for the nanotube curvature study

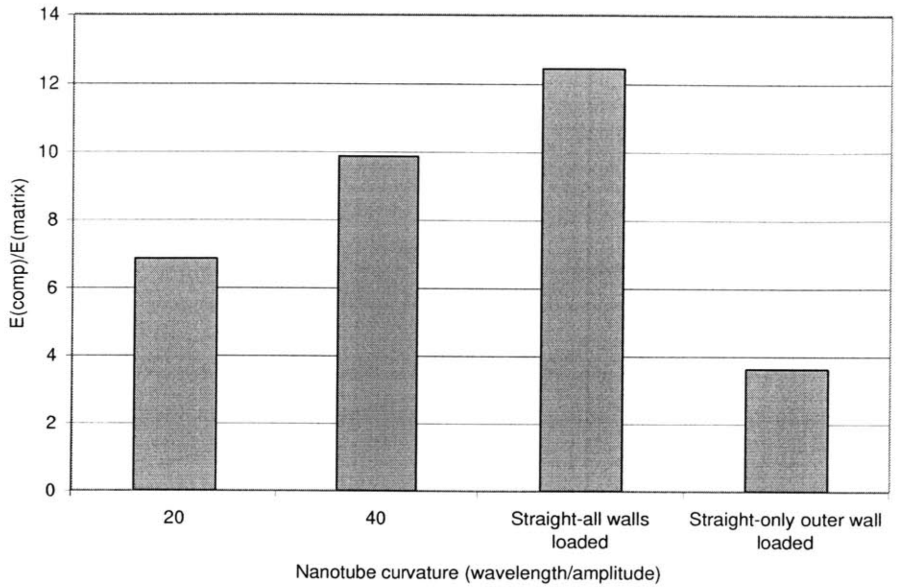

Figure 5-22: Normalized composite stiffness variation with nanotube curvature

Figure 5-22 shows a graph of the normalized composites stiffness as a function of the curvature, measured in terms of the ratio of the wavelength to the amplitude. The graph suggests that the nanotube curvature has an adverse effect on the axial modulus of the composite. This can be attributed to the low bending stiffness of the nanotube, modelled as a beam, compared to its axial stiffness. $k_{bending}/k_{axial} \ll 1$. Nevertheless, the predicted macroscopic stiffness of a composite containing curved multi-wall nanotubes is still larger than that of a composite containing straight multi-wall nanotubes that cannot transfer load internally which is due to the fact that even if the inner walls are not functionalized in a curved nanotube, they still resist bending deformations and thus enhance the bending stiffness of the nanotube and the macroscopic axial stiffness of the composite.

Figures 5-23 and 5-24 show graphs of the axial stress distribution across the nan-

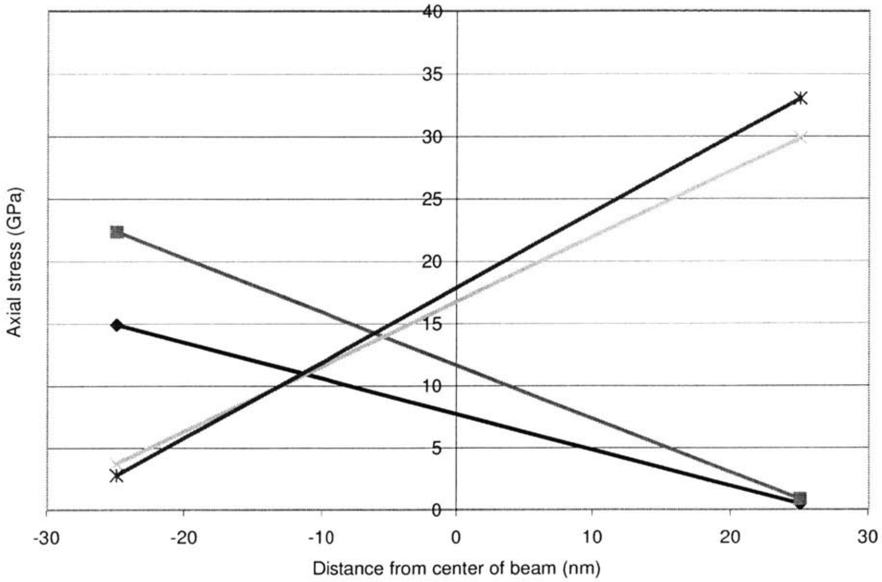

Figure 5-23: Axial stress distribution across nanotube cross section for model with nanotube curvature $\lambda/\alpha = 10$

otube cross-section at 4 distinct points along a nanotube in the highly curved and slightly curved models accordingly. As the curvature decreases, the stress distribution approaches that of a straight nanotube loaded in tension, as suggested by these figures. As a result, in a multi-wall nanotube with limited or no load transfer to its inner walls, some curvature might actually enhance its stiffening effect, as inner walls provide flexural rigidity to the nanotube. The amount of curvature in such a nanotube is thus constrained by the low bending-to-axial stiffness ratio at the upper bound and by the inability of the inner walls to carry axial loads at the lower bound. An optimum curvature would be dependent upon the geometry of the nanotube, number of walls, as well as its effective stiffness.

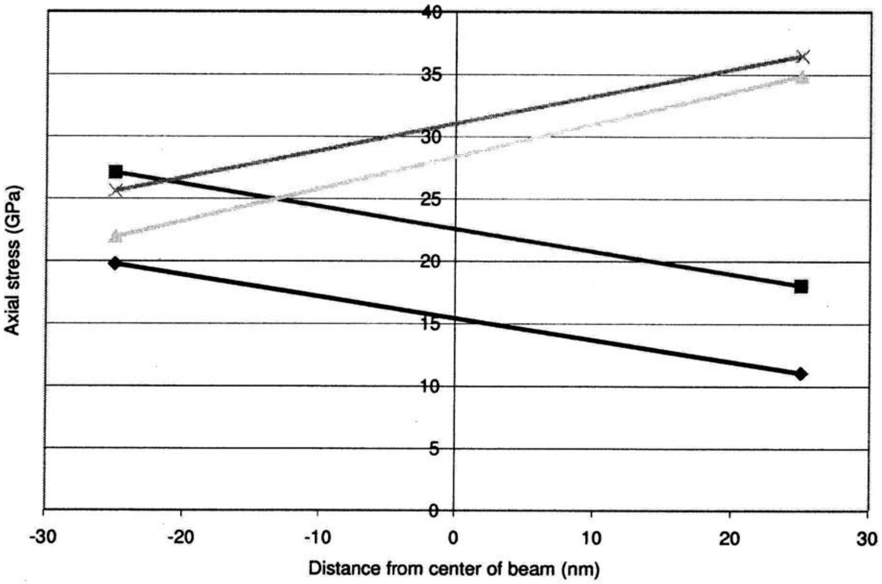

Figure 5-24: Axial stress distribution across nanotube cross section for model with nanotube curvature $\lambda/\alpha = 20$

Chapter 6

Summary, conclusions and future work

In this thesis, various efforts and approaches to modelling the microstructure and mechanical properties of nanotube-enabled composites were presented in detail and the results were discussed and used to shed light on the underlying mechanisms that affect the mechanical behavior of such composites. The goal was to identify and investigate in detail the parameters that dictate the macroscopic properties of the composites and develop modelling techniques that capture effectively and efficiently the relationships between microscopic mechanisms and macroscopic behavior. Key conclusions of this thesis can be classified into two main categories: Those focusing on the modelling issues of carbon nanotube-enabled composites and those dealing with the macroscopic composite properties in relation to microstructural parameters.

6.1 Modelling techniques

6.1.1 Composite modelling

Unit-cell models

Initial modelling efforts focused on unit-cell representative volume elements, containing a single nanotube embedded in a matrix and featuring periodic boundary conditions, that simulated either a stacked or a staggered spacial arrangement of nanotubes. Such boundary conditions introduced the effects of particle interactions, normally encountered in multi-phase systems, without requiring the modelling of multiple particles. In all studies, the focus was on subjecting the RVE in uniaxial tension and extracting the macroscopic stiffness of composites containing perfectly aligned nanotubes. The implementation of these boundary conditions coupled with the multiple symmetries in the geometry allowed for efficient and computationally inexpensive simulations.

The stacked and staggered periodic boundary conditions represent two different approaches to approximating a completely random particle distribution in the matrix. Between the two, the staggered array resembles a random dispersion more closely than the stacked array and, as a result, captures with greater accuracy the behavior of a composite with randomly dispersed particles. In the stacked array, in scanning the modelled composite along the direction of the nanotubes, one encounters layers with high nanotube concentrations alternating with layers of pure matrix. As a result of this layered pattern, stacked models are very sensitive to the aspect ratio of the RVE, which is a parameter associated with the model rather than the actual geometry of a composite. This non-uniformity also leads to highly localized straining of the softer phase, the matrix, and minimal straining of the stiffer phase, the nanotube which, consequently, offers only limited stiffening to the composite. On the other hand, staggered arrays display significantly less variation in space, assuming the nanotube volume fraction and/or aspect ratio are maintained above a minimum value. As a result, they capture the stiffening effects more accurately and are virtually immune to variations in the RVE aspect ratio. For this reason, they constitute a better alternative to modelling unit-cell RVEs and performing single-parameter sensitivity analyses than stacked arrays.

3-D models

Modelling efforts then shifted towards a 3-D model that focused on regions of the composite large enough to include multiple nanotubes, ranging from 4 or 5 to more than 20. Periodic boundary conditions were applied in this model as well, as the model only processes a RVE that, conceptually, repeats itself periodically and extends in all three dimensions. The major advantage of the 3-D model vs. the unit-cell models is the size of its scope, which is able to capture multiple, randomly dispersed particles as opposed to single particles, forced into a patterned array. As a result, it better simulates actual composites in terms of particle dispersion, although it is still an approximation as it is also characterized by periodicity, albeit on a larger volume scale than the unit-cell models. In addition to capturing the randomness of nanotube dispersion, the 3-D model can be used to study the effects of randomness of nanotube alignment and curvature as well as non-uniform distributions (clusters, entangled nanotube, etc.). The tradeoff for the increased capabilities and accuracy of the 3-D model is its increased computational requirement, which limits the size of the RVEs considered.

6.1.2 Particle modelling

The particle itself (the nanotube in this case) also is subject to different modelling techniques. In the unit-cell models, a continuum mechanics approach was used to model each wall of the nanotube as a thin shell with a finite thickness and appropriate mechanical properties. In addition, user-defined elements were used to model the van der Waals interactions among the nanotube walls. Although not as detailed as atomistic simulations, this modelling technique captures with accuracy the behavior of the nanotube as a whole as well as the mechanisms and interactions among its constituent walls. It is particularly useful for studying issues related to the microstructure of the nanotubes, such as the role of the endcaps, the stress transfer along each wall and across walls in the case of multi-wall nanotubes, as well as phenomena such as wall debonding, sword-in-sheath modes of failure, etc.. Another method of modelling the nanotubes was employed for the 3-D models, resulting from a shift of focus from the nanotube microstructure towards dispersion-related issues. In this case, the nanotubes were modelled as slender beams, with an effective cross-sectional area consisted with the area of an actual nanotube. This is a higher-level, 'black-box' approach to nanotube modelling in that it neglects the mechanical response of individual walls and simulates the nanotubes as solid, cylindrical particles, with appropriate effective material properties. As a result, no predictions can be made about internal mechanisms, such as wall debonding; instead, the effect of such occurrences needs to be manually input into the model in order for it to be accounted for.

6.2 Effects of material microstructure on the mechanical properties of the composite

The staggered unit-cell models and the 3-D models were both used to perform sensitivity analyses on various parameters that affect the macroscopic stiffness of the composite. Parameters of interest were the nanotube aspect ratio and volume fraction, the number of walls, as well as nanotube curvature. Two important assumptions were made for the sake of simplicity and efficiency of the model. First, in all cases, the nanotubes were assumed to be perfectly bonded to the matrix. Second, they were assumed to be untangled and perfectly aligned to the loading axis.

Macroscopic stiffness has a positive correlation both with the nanotube aspect ratio and the volume fraction. As the aspect ratio increases, the load-carrying length of the nanotube and the maximum stress increase as well, thus raising the overall stiffening effect. In the limiting case, macroscopic stiffness approaches the upper bound solution for a continuous-fiber-reinforced composite. Furthermore, particle interactions became increasingly important with increasing l/d, as evidenced by the merging of matrix strain perturbations. Particularly in the case of the staggered model, nanotube overlap in the radial direction, which depends on the nanotube aspect ratio, had a significant impact on the axial stress profile along the nanotube. Similar trends were observed with the variation of nanotube volume fraction. Due to the perfect bonding assumption and the large particle-to-matrix stiffness ratio, even small loads of nanotubes in the matrix had a substantial impact on the macroscopic stiffness of the composite. Above a certain nanotube concentration threshold, matrix strain shielding occurs, impeding load transfer from the matrix to the nanotube, which is a function of the matrix shearing. As a result, the reinforcing efficiency of the nanotubes is reduced.

Comparison between the staggered unit-cell model and the 3-D multi-particle model does not yield any definite conclusions as to which produces the highest axial stiffness predictions for the composite. Although the 3-D model results are higher on average, there is significant statistical variation in the 3-D modelling results due to the random nature of the dispersion. Furthermore, the sensitivity of the staggered model to the RVE aspect ratio, albeit weaker than that of the stacked model, can still affect the predicted results. As the RVE aspect ratio decreases, the nanotube takes up a larger portion of the total RVE length and thus, the predicted stiffness increases as the RVE behavior approaches that of a continuous fiber composite. In this limiting case, the unit-cell models should converge with the 3-D models in their predictions of macroscopic stiffness.

Both the unit-cell and the 3-D model yield considerably higher predictions for the axial composite stiffness than experimental measurements reported in literature for similar volume fractions and aspect ratios. A combination of parameters lead to this discrepancy. First, the bonding between the nanotubes and the matrix is generally weak, as evidenced by instances of nanotube pull-out, observed in micrographs of fractured surfaces of composites. There have been numerous efforts to functionalize the external surface of the nanotube by cross-linking the outer wall to the amorphous or crystalline matrix, or by coating the nanotube. Although there may be an increase in the strength of the interfacial bond, it is still far from the perfect bonding assumption that was used in the models. With no slippage occurring along the nanotube-matrix interface, load is transferred more efficiently to the fully functionalized, modelled nanotubes, yielding higher stiffness predictions.

The modelling condition that the nanotubes be perfectly aligned and straight has similar effects on the stiffness values. As suggested by the curvature analysis conducted using the 3-D model, even limited nanotube curvature can result in significant decrease in the macroscopic stiffness of the composite, as the nanotubes are loaded in bending rather than in tension. The ratio $k_{bending}/k_{axial} \ll 1$ justifies the drop in composite stiffness when nanotubes are loaded in bending rather than in tension. This also explains in part the difference between modelling predictions and experimental data. Due to their high aspect ratio, even well-aligned nanotubes are characterized by non-zero curvature when dispersed inside a matrix and thus, they are loaded in bending, at least at relatively small strains. At higher strains, the nanotubes stretch and line up with the loading axis, at which point one might expect an increase in composite stiffness. However, this effect is annulled by phenomena such as nanotube-matrix debonding, wall fracture, etc..

Another parameter that affects the behavior of the composite is the number of walls that are effectively loaded in a multi-wall nanotube-enabled composite. As shown in Chapter 5, the stiffness of the composite depends heavily on how much load is transferred from the outer wall of a nanotube to its inner walls. Given that wall-to-wall interactions occur as weak van der Waals bonds, inner walls carry only small loads and do not contribute to the stiffening of the composite, although they may increase the flexural rigidity of the nanotube. In addition, inner walls tend to debond even at small strains, as evidenced both by the modelling results and the 'sword-in-sheath' nanotube failure mode observed in actual fractured specimens. Low internal load transfer is yet another issue then that leads to discrepancies between the predicted stiffness values and the experimental data.

6.3 Conclusions

It seems therefore that nanotubes have great potential as reinforcing agents in polymer matrices that is nevertheless hindered by a number of currently unresolved issues. The ability to transfer high loads from the matrix to the nanotube is crucial to capitalizing on the extremely high stiffness of nanotubes but has yet to be fully accomplished. Efforts to functionalize the nanotube surface have centered around coatings and cross-links with the matrix. However, sacrificing C-C bonds in the wall to form new bonds with the matrix dramatically compromises the structural integrity of the nanotube and, as a result, its load-carrying capacity. This is particularly important in single wall nanotubes, which only have a single load-carrying wall.

Nanotube dispersion is also a parameter on which research efforts have been focusing. Numerous methods have been employed to reduce or eliminate nanotube clustering, entanglement and misalignment, such as sonication, use of surfactants and coatings, melt spinning, solution-evaporation methods, etc.. Uniform dispersion ensures that each nanotube contributes to the stiffening of the composite by straining and carrying high stresses, assuming adequate load transfer from the matrix to the nanotube. Furthermore, although both the nanotube aspect ratio and volume fraction were shown to have a positive effect on predicted composite stiffness, they tend to impede processing of the composite and to trigger the formation of clusters as they increase, thus having an adverse effect on composite stiffness.

Between single and multi-wall nanotubes, the former possess a slight mechanical advantage over the latter as they have a higher effective elastic modulus due to their significantly smaller cross sectional area. However, they have a strong tendency to entangle and form ropes, without dispersing uniformly in the matrix. This creates yet another hindrance to the reinforcing effect as the single wall nanotubes slide past each other when formed in ropes. Furthermore, due to their low flexural rigidity, they are subject to high curvature and misalignment. On the other hand, although multi-wall nanotubes are less stiff and cannot utilize their inner walls due to their inability to transfer load internally, they are easier to align and process and, currently, they are produced in larger quantities, which also makes them more cost efficient. Global single wall nanotube production capacity is currently running at 9 tons per year with the potential to increase to 20 tons by the year's end, while capacity for multi-wall nanotubes is already 32 tons per year (http://www.nanospace.org/, 2004).

In conclusion, adequate load transfer capability and uniform dispersion are both prerequisites to the design and production of a nanotube-enabled polymer composite that capitalizes on the superb mechanical properties of nanotubes. Complete nanotube functionalization along the matrix-nanotube interface is neither achievable at this point nor desirable and as a result, load transfer from the matrix to the nanotube needs to occur through a combination of partial interfacial bonding and other methods, such as mechanical interlocking among nanotubes, possibly arranged in a non-woven fabric-like pattern. In terms of designing such composites and predicting their macroscopic behavior, the three-dimensional modelling capability that has been developed can be used to accurately simulate these and other conditions and capture their effect, such as nanotube misalignment, clustering and interfacial slipping/debonding.

Appendix A

Effect of nanotube diameter on macroscopic axial stiffness of a random, 3-D RVE

$$E_{CNT} = \frac{A_{wall} E_{wall}}{A_{CNT}} \tag{A.1}$$

where E_{CNT} is the effective nanotube elastic modulus, A_{wall} is the cross-sectional area of the wall, E_{wall} is the elastic modulus of the wall and A_{CNT} is the effective cross sectional area of the nanotube.

NT length (nm)	160	160	160
NT diameter (nm)	0.6875	1.3751	2.0626
NT l/d	23273	11636	7757
NT stiffness (GPa)	2112	1056	704
RVE length (nm)	240	240	240
RVE width (nm)	14	14	14
RVE l/w	17	17	17
Matrix stiffness (GPa)	3.1	3.1	3.1
Volume fraction	5%	5%	5%

Table A.1: Geometric data for the single wall nanotube diameter sensitivity study

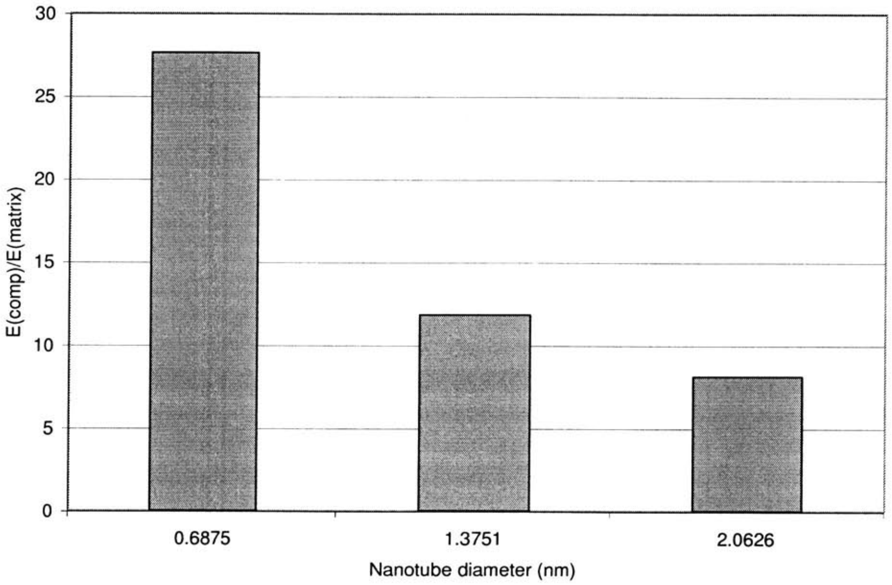

Figure A-1: Normalized composite stiffness for different single wall nanotube diameters

Bibliography

[1] Beaumont, P. W. R. (1989) The failure of fiber composites - An overview. *J. Strain Anal.* **24**(4), 189-205.

[2] Edison, T. A. (1892) US Patent 470,925 (issued March 15, 1892).

[3] Edwards, K. L. (1998) An overview of the technology of fibre-reinforced plastics for design purposes. *Mater. Des.* **19**(1-2), 1-10.

[4] Saito, R., Dresselhaus, G. and Dresselhaus, M. S. (1998). *Physical properties of carbon nanotubes.* Imperial College Press.

[5] Jones, R. M. (1999). *Mechanics of composite materials.* 2nd ed., Taylor & Francis, Inc.

[6] Courtney, T. H. (1990). *Mechanical behavior of materials.* McGraw-Hill, Inc.

[7] Dresselhaus, M. S. and Endo, M. (2001a) Relation of carbon nanotubes to other carbon materials. *Topics Appl. Phys.* Eds. Dresselhaus, M. S., Dresselhaus, G. and Avouris, Ph., **80**, 11-28.

[8] Kroto, H. W., Heath, J. R., O'Brien, S. C., Curl, R. F. and Smalley, R. E. (1985) C-60 - Bucminsterfullerene. *Nature* **318**(6042), 162-163.

[9] *http://www.chem.sunysb.edu/msl/* (2004).

[10] Iijima, S. (1991) Helical microtubules of graphitic carbon. *Nature* **354**(6348), 56-58.

[11] Walsh, P. J. (2001) Carbon fibers. *ASM Handbook* **21**, 35-40.

[12] Dresselhaus, M. S., Dresselhaus, G., Sugihara, K., Spain, I. L. and Goldberg, H. A. (1988). *Graphite fibers and filaments.* Springer-Verlag.

[13] Jacobsen, R. L., Tritt, T. M., Guth, J. R., Ehrlich, A. C. and Gillespie, D. J. (1995) Mechanical properties of vapor-grown carbon fiber. *Carbon.* **33**(9), 1217-1221.

[14] Ting, J. and Lake, M. L. (1994) Vapor-grown carbon-fiber reinforced carbon composites. *Carbon.* **33**(5), 663-667.

[15] Schaffer, J. P., Saxena, A., Antolovich, S. D., Sanders, T. H. and Warner, S. B. (1995). *The science and design of engineering materials.* Irwin.

[16] Tucker, C. M. and Liang, E. (1999) Stiffness predictions for unidirectional short-fiber composites: Review and evaluation. *Compos. Sci. Technol.* **59**(5), 655-671.

[17] Cox, H. L. (1952) The elasticity and strength of paper and other fibrous materials. *Brit. J. Appl. Phys.* **3**(72), 72-79.

[18] Eshelby, J. D. (1957) The determination of the elastic field of an ellipsoidal inclusion and related problems. *Proc. Roy. Soc. A* **241**, 376-396.

[19] Hill, R. (1963) Elastic properties of reinforced solids: Some theoretical principles. *J. Mech. Phys. Solids* **11**, 357-372.

[20] Xia, Z., Curtin, W. A. and Okabe, T. (2002b) Green's function vs. shear-lag models of damage and failure in fiber composites. *Compos. Sci. Technol.* **62**, 1279-1288.

[21] Beyerlein, I. J. and Phoenix, S. L. (1996) Comparison of shear-lag theory and continuum fracture mechanics for modeling fiber and matrix stresses in an elastic cracked composite lamina. *Int. J. Solids Structures.* **33**(18), 2543-2574.

[22] Xia, Z., Curtin, W. A. and Okabe, T. (2002a) Shear-lag vs. finite element models for stress transfer in fiber-reinforced composites. *Compos. Sci. Technol.* **62**, 1141-1149.

[23] Steif, P. S. and Hoysan, S. F. (1987) An energy method for calculating the stiffness of aligned short-fiber composites. *Mech. Mater.* **6**, 197-210.

[24] Mori, T. and Tanaka, K. (1973) Average stress in matrix and average elastic energy of materials with misfitting inclusions. *Acta Metallurgica.* **21**, 571-574.

[25] Thostenson, E. T., Ren, Z. and Chou, T. (2001) Advances in the science and technology of carbon nanotubes and their composites: a review. *Compos. Sci. Technol.* **61**, 1899-1912.

[26] Louie, S. G. (2001) Electronic properties, junctions and defects of carbon nanotubes. *Topics Appl. Phys.* Eds. Dresselhaus, M. S., Dresselhaus, G. and Avouris, Ph., **80**, 113-145.

[27] Ajayan, P. M. and Ebbesen, T. W. (1997) Nanometre-size tubes of carbon. *Rep. Prof. Phys.* **60**, 1025-1062.

[28] Dresselhaus, M. S. and Avouris, P. (2001b) Introduction to carbon materials research. *Topics Appl. Phys.* Eds. Dresselhaus, M. S., Dresselhaus, G. and Avouris, Ph., **80**, 1-9.

[29] Baughman, R. H., Zakhidov, A. A. and de Heer, W. A. (2002) Carbon nanotubes - The route towards applications. *Science* **297**, 787-792.

[30] Yakobson, B. I. and Avouris, P. (2001) Mechanical properties of carbon nanotubes. *Topics Appl. Phys.* Eds. Dresselhaus, M. S., Dresselhaus, G. and Avouris, Ph., **80**, 287-327.

[31] Treacy, M. M. J., Ebbesen, T. W. and Gibson, J. M. (1996) Exceptionally high Young's modulus observed for individual carbon nanotubes. *Nature* **281**(6584), 678-680.

[32] Krishnan, A., Dujardin, E., Ebbesen, T. W., Yianilos, P. N. and Treacy, M. M. J. (1998) Young's modulus of single-walled nanotubes. *Phys. Rev. B.* **58**(20), 14013-14019.

[33] Wong, E. W., Sheehan, P. E. and Lieber, C. M. (1997) Nanobeam mechanics: Elasticity, strength and toughness of nanorods and nanotubes. *Science* **277**, 1971-1975.

[34] Salvetat, J., Briggs, G. A. D., Bonard, J., Bacsa, R. R., Kulik, A. J., Stockli, T., Burnham, N. A. and Forro, L. (1999) Elastic and shear moduli of single-walled carbon nanotube ropes. *Phys. Rev. Lett.* **82**(5), 944-947.

[35] Yu, M., Lourie, O., Dyer, M. J., Moloni, K., Kelly, T. F. and Ruoff, R. S. (2000a) Strength and breaking mechanism of multiwalled carbon nanotubes under tensile load. *Science* **287**, 637-640.

[36] Yu, M., Files, B. S., Arepalli, S. and Ruoff R. S. (2000b) Tensile loading of ropes of single wall carbon nanotubes and their mechanical properties. *Phys. Rev. Lett.* **84**(24), 5552-5555.

[37] Qi, H. J., Teo, K. B. K., Lau, K. K. S., Boyce, M. C., Milne, W. I., Robertson, J. and Gleason, K. K. (2003) Determination of mechanical properties of carbon nanotubes and vertically aligned carbon nanotube forests using nanoindentation. *J. Mech. Phys. Solids.* **51**(11-12), 2213-2237.

[38] Pantano, A., Parks, D. M. and Boyce, M. C. (2004) Mechanics of deformation of single- and multi-wall carbon nanotubes. *J. Mech. Phys. Solids.* **52**(4), 789-821.

[39] Chopra, N. G., Benedict, L. X., Crespi, V. H., Cohen, M. L., Louie, S. G. and Zettl, A. (1995) Fully collapsed carbon nanotubes. *Nature* **377**(6545), 135-138.

[40] Poncharal, P., Wang, Z. L., Ugarte, D. and de Heer, W. A. (1999) Electrostatic deflection and electromechanical resonances of carbon nanotubes. *Science* **283**(5407), 1513-1516.

[41] Hernandez E., Goze, C., Bernier, P. and Rubio, A. (1998) Elastic properties of C and BxCyNz composite nanotubes. *Phys. Rev. Lett.* **80**(20), 4502-4505.

[42] Cadek, M., Coleman, J. N., Ryan, K. P., Nicolosi, V., Bister, G., Fonseca, A., Nagy, J. B., Szostak, K., Beguin, F. and Blau, W. J. (2004) Reinforcement of polymers with carbon nanotubes: The role of nanotube surface area. *Nano Lett.* **4**(2), 353-356.

[43] Gorga, R. E. and Cohen, R. E. (2004) Toughness enhancements in poly(methyl methacrylate) by addition of oriented multiwall carbon nanotubes. *J. Polym. Sci. Pol. Phys.* **42**.

[44] Wagner, H. D., Lourie, O., Feldman, Y. and Tenne, R. (1998) Stress-induced fragmentation of multiwall carbon nanotubes in a polymer matrix. *Appl. Phys. Lett.* **72**(2), 188-190.

[45] Ajayan, P. M., Schadler, L. S., Giannaris, C. and Rubio, A. (2000) Single-walled carbon nanotube-polymer composites: Strength and weakness. *Adv. Mater.* **12**(10), 750-753.

[46] Schadler, L. S., Giannaris, S. C. and Ajayan, P. M. (1998) Load transfer in carbon nanotube epoxy composites. *Appl. Phys. Lett.* **73**(26), 3842-3844.

[47] Qian, D., Dickey, E. C., Andrews, R. and Rantell, T. (2000) Load transfer and deformation mechanisms in carbon nanotube-polystyrene composites. *Appl. Phys. Lett.* **76**(20), 2868-2870.

[48] Kumar, S., Dang, T. D., Arnold, F. E., Bhattacharyya, A. R., Min, B. G., Zhang, X., Vaia, R. A., Park, C., Adams, W. W., Hauge, R. H., Smalley, R. E., Ramesh, S. and Willis, P. A. (2002) Synthesis, structure and properties of PBO/SWNT composites. *Macromolecules* **35**(24), 9039-9043.

[49] Du, F., Fischer, J. E. and Winey, K. I. (2003) Coagulation method for preparing single-walled carbon nanotube/poly(methyl methacrylate) composites and their

modulus, electrical conductivity, and thermal stability. *J. Polym. Sci. Pol. Phys.* **41**(24), 3333-3338.

[50] Haggenmueller, R., Gommans, H. H., Rinzler, A. G., Fischer, J. E. and Winey, K. I. (2000) Aligned single-wall carbon nanotubes in composites by melt processing methods. *Chem. Phys. Lett.* **330**(3-4), 219-225.

[51] Schueler, R., Petermann, J., Schulte, K. and Wentzel, H. P. (1997) Agglomeration and electrical percolation behavior of carbon black dispersed in epoxy resin. *J. Appl. Polym. Sci.* **63**(13), 1741-1746.

[52] Sandler, J. K. W., Kirk, J. E., Kinloch, I. A., Shaffer, M. S. P. and Windle, A. H. (2003) Ultra-low electrical percolation threshold in carbon-nanotube-epoxy composites. *Polymer* **44**(19), 5893-5899.

[53] Socrate, S. and Boyce, M. C. (2000) Micromechanics of toughened polycarbonate. *J. Mech. Phys. Solids* **48**(2), 233-273.

[54] Odegard, G. M., Harik, V. M., Wise, K. E. and Gates, T. S. (2001) Constitutive modeling of nanotube-reinforced polymer composite systems. *http://citeseer.ist.psu.edu/odegard01constitutive.html*

[55] Zhao, Y. X. and Spain, I. L. (1989) X-ray-diffraction data for graphite to 20 GPa. *Phys. Rev. B.* **40**(2), 993-997.

[56] Meincke, O., Kaempfer, D., Weickmann, H., Friedrich, C., Vathauer, M. and Warth, H. (2004) Mechanical properties and electrical conductivity of carbon-nanotube filled polyamide-6 and its blends with acrylonitrile/butadiene/styrene. *Polymer* **45**(3), 739-748.

[57] Andrews, R., Jacques, D., Minot, M. and Rantell, T. (2002) Fabrication of carbon multiwall nanotube/polymer composites by shear mixing. *Macromol. Mater. Eng.* **287**(6), 395-403.

[58] Cooper, C. A., Ravich, D., Lips, D., Mayer, J. and Wagner, H. D. (2002) Distribution and alignment of carbon nanotubes and nanofibrils in a polymer matrix. *Compos. Sci. Technol.* **62**(7-8), 1105-1112.

[59] Singh, S., Pei, Y., Miller, R. and Sundararajan, P. R. (2003) Long-range, entangled carbon nanotube networks in polycarbonate. *Adv. Funct. Mater.* **13**(11), 868-872.

[60] Danielsson, M., Parks, D. M. and Boyce, M. C. (2002) Three-dimensional micromechanical modeling of voided polymeric materials. *J. Mech. Phys. Solids* **50**, 351-379.

[61] *http://www.nanospace.org* (2004).